Università Cattolica Del Sacro Cuore

University of Notre Dame

Istituto Italiano di Tecnologia

XXXIII Ciclo di Dottorato - International PhD in Science

ADVANCED NANOCOMPOSITES FOR PHOTOCATYLITIC DEGRADATION OF ORGANIC POLLUTANTS IN WATER

A Dissertation

for the Degree of

Doctor of Philosophy

By

Federica Costantino

Supervisors

Dott.ssa Despina Fragouli

Prof. Luca Gavioli

Prof. Prashant V. Kamat

Academic year 2021-2022

Acknowledgments

Four years of doctoral study at Istituto Italiano di Tecnologia (IIT), University of Notre Dame and Università Cattolica del Sacro Cuore has been a rewarding experience both in my personal and professional life. I would like to acknowledge several people who have supported and helped me throughout this journey.

First and foremost, I would like to thank my supervisors Dr. Despina Fragouli, Prof. Prashant V. Kamat, and Prof. Luca Gavioli for their guidance and motivation during these years.
I would like to thank all my mates from Smart Materials Lab and Kamat's group, it was a pleasure to work and meet all of you guys.

I would love to thank my Dad and Mum: Michele and Elisabetta, my siblings: Lorenzo and Roberta, for their loving care and their unconditional support wherever I went, and the motivation that they give to me every day. I feel your love every single moment even miles away from home, despite the distance I have always felt close to you.
I would like to thank Riccardo for his love, understanding, and encouragement that give to me every day in my scientific career and life; he is always there where I need his support and love.
My greatest gratitude goes to the friends that I met during this PhD adventure in IIT and outside the lab: Ana, Giulia M, Giulia S, Maria Elena, Margherita, Valentina, Maria Laura, Despoina, Giorgia, Gabriele, Edoardo, Fabrizio, Marco, Marta, Martina, Dagmara, Giacomo, Stefano T., Francesco. We spent an unforgettable time together and I am sure we will keep in touch, meet again and create new amazing memories around Italy and over the country.

A special thank goes to Federica (Feef), you are one of the best girl that I ever met; we spent a lot of time together: making new recipes, talking about phycology, watching amazing TV series, kayaking in the sea and hiking around Genoa and in Sicily as well. We supported each other both in our personal and academic life.

I sincerely thank all of the friends that I met during my time in the US: Chiara, Enrico, and Irina. A special thank goes to Maria Sole, we shared many adventures during our travel, dinner, and breaks around Notre Dame Lake, I am lucky to meet you and find a new friend.

Thank to my friends in Partinico: Silvia, Federica, Serena, Pietro, Noemi, Luca, Totò, Maria Lorena, Federico, Monica, Valentina, Peppe, Roberta and Daniela. It is always lovely to come back home, get updated about each other's lives, share chats, time and dinner.

This dissertation is dedicated to all of you, thank you.

The future belongs to

those who believe in

the beauty of their

dreams

Contents

ADVANCED NANOCOMPOSITES FOR PHOTOCATaLYTiC DEGRADATION OF ORGANIC POLLUTANTS IN WATER 7

ABSTRACT.....7

CHAPTER 1: GENERAL INTRODUCTION 11
1.1 Water Scarcity and Water Pollution.....11
1.2 Sources of Organic Pollutants in water 13
1.2.1 Organic Dyes 14
1.2.2 Pesticides.....16
1.3 Common Wastewater Treatment Processes.....18
1.4 Photocatalysis.....21
1.4.1 Heterogeneous Photocatalysis.....21
1.5 Nanotechnology.....25
1.6 Doping of Semiconductors 30
1.7 Polymer Nanocomposites, an alternative approach for water treatment process.....32
1.7.1 Polymers matrix with metal oxide NPs for photocatalysis.....36
1.8 Research Aim and Scope.....38
1.9 References.....41

CHAPTER 2: CELLULOSE ACETATE TIN DIOXIDE FIBROUS MEMBRANE FOR THE PHOTOCATALYTIC DEGRADATION OF ORGANIC DYES 49
2.1 Introduction.....50
2.2 Materials and Methods.....51
2.2.1 Chemicals.....51
2.2.2 Fibers Preparation.....51
2.3 Photodegradation experiment.....52
2.3.1 Analysis of photodegraded products.....54
2.4 Results and Discussion.....55
2.4.1 Morphological Characterization of the CA/SnO_2.....55
2.5 Photocatalytic degradation of MO and MB 62
2.6 Liquid Chromatography analysis after photodegradation.....69
2.7 Conclusions.....71
2.8 References.....73

CHAPTER 3: DIRECT FORMATION OF CERIA/PLATINUM NANOSTRUCTURES ON POLYMERIC MATS FOR DEGRADATION OF METHYLENE BLUE DRIVEN BY VISIBLE IRRADIATION.....76

3.1 Introduction.....77
3.2 Materials and Method.....78
3.2.1 Chemicals.....78
3.2.2 Fiber preparation.....78
3.3 Photocatalytic tests.....80
3.4 Reactive Oxygen Species Identification.....81
3.5 Results and Discussion.....83
3.5.1 Morphological Characterization of the mats.....83
3.6 Photocatalytic degradation performance under visible light irradiation.99
3.7 Reactive oxygen species (ROS) identification.....104
3.8 Conclusions.....107
3.9 References.....109

CHAPTER 4: TRACKING THE ELECTRON FLOW IN THE PHOTOCATALYTIC ACTIVITY OF BIPOLAR Pd/CdS MEMBRANE.....112

ABSTRACT.....112
4.1 Introduction.....113
4.2 Materials and Method.....114
4.2.1 Chemicals.....114
4.3 Fabrication of BPM-CdS.....115
4.3.1 Fabrication of BPM-CdS/Pd.....116
4.4 Photocatalytic Experiments using BPM-CdS/Pd.....117
4.4.1 Reduction of Methyl Viologen.....118
4.4.2 Oxidation of 4-Nitro Phenol.....118
4.4.3 Simultaneous Oxidation and reduction of 4-Chlorophenol and 4-Nitrophenol.....119
4.5 Results and Discussion.....119
4.5.1 Morphological characterization of BPM-CdS/Pd.....119
4.6 Photocatalytic reduction of Methyl Viologen to optimize the Pd concentration.....125
4.7 Photodegradation of Nitro-phenolic compounds.....130
4.7.1 Simultaneously photodegradation of chloro-phenol and nitro-phenol compounds.....132
4.8 Conclusion.....136

CHAPTER 5: CONCLUSIONs AND FUTURE WORK.....141

Appendix A: INSTRUMENT DETAILS.....144

Appendix B: CALCULATION AND APPROXIMATION.....147

Appendix C: EXPERIMENTAL SUPPORT.....149

ADVANCED NANOCOMPOSITES FOR PHOTOCATALYTIC DEGRADATION OF ORGANIC POLLUTANTS IN WATER

ABSTRACT

Water plays a vital role in sustain life on earth. However, the quality of the water resources is seriously affected by the pollution caused by industrial, municipal and agricultural activities. To remediate the toxic organic and inorganic contaminants in water, several physical, chemical and biological water treatment methods are employed. However, current water treatment technologies present limited performance, materials of high cost, and need highly energy consuming infrastructure. In this scenario, the utilization of advanced materials and innovative methods could be helpful for reducing the cost and enhancing the performance of the wastewater treatment. One of most promising method is the Advanced Oxidation Processes (AOPs). The AOPs use semiconductor materials that are activated by the UV or Visible light irradiation that are able to mineralize organic water pollutants. Currently, commercial available photocatalysts are mostly used in slurry or powder form, but this requires post-treatment processes in order to avoid secondary pollution, causing the increase of the overall treatment cost. To face up such limitation and to resolve problems related to the post-treatment process, the immobilization of the photocatalysts on solid compact matrices is a feasible solution. In particular, the use of polymeric matrices as host solid materials may result in a final system that combines the

photocatalytic properties of the semiconductor component with the mechanical properties, usability and cost effectiveness of the polymers.

In this study are developed polymeric nanocomposites for their utilization in AOPs. The study is focused on the (i) investigation of the chemical and physical characteristics of the prepared samples and (ii) evaluation of their photocatalytic performance on the degradation of organic pollutants in water.

This study was possible thanks to the collaboration of the Smart Materials group of Istituto Italiano di Tecnologia (IIT) in Genova, the research group of Interdisciplinary Laboratory for Advanced Materials Physics (I-Lamp) at Università Cattolica del Sacro Cuore (UCSC) in Brescia and the Radiation Laboratory of the University of Notre Dame (ND, Indiana, USA).

The promising results are summarized and illustrated in this thesis, which has been structured in five chapters:

The Chapter 1 is dedicated to the water pollutants, starting from the causes and reaching to the remediation processes. In this chapter, the description of the Advanced Oxidative Processes (AOPs) and their utilization as an innovative solution for water decontamination are presented. Specifically, are discussed the characteristic of this process and the different types of semiconductors which are used in this process concluding on the utilization of polymeric nanocomposites in the wastewater treatment through AOPs.

Chapter 2 presents the development of a porous nanocomposite mat composed of cellulose acetate (CA) and tin dioxide (SnO_2) for the photocatalytic degradation of organic pollutants. The nanocomposite is prepared by the combination of the electrospinning technique and the *in-Situ* thermal activation of tin precursor directly in the fibrous mats. The final nanocomposites are used for the photocatalytic degradation of an anionic dye

(Methylene Blue (MB)) and a cationic one (Methyl Orange (MO)) in water under UV irradiation. The mats are able to photodegrade both types of dyes with an efficiency of more than 90%. After the photodegradation process the by-products are studied with the Liquid Chromatography-Mass Spectrometry (LC-MS) which indicates the de-methylation of the organic structure for both dyes and a hydroxylation process in the MO azo-dye as the main degradation roots.

The characteristic and photocatalytic activity of the CA polymer fibers combined with cerium nanoparticles (CeNPs) and platinum (Pt) nanostructures (CA/CeNPs/Pt) are discussed in the Chapter 3. The mats are prepared by the combination of the supersonic beam deposition (SCBD) of Pt nanoclusters directly on the surface of electrospun CA fibrous mats, which are pre-loaded with a cerium salt precursor and transformed into CeNPs directly in the solid mats by a simple thermal treatment. The photocatalytic performance of the final composites is evaluated by the degradation of the MB under visible light irradiation, and is proved that the mats reach a degradation efficiency of 70%. As demonstrated the presence of Pt nanoclusters enhances the photocatalytic activity of the nanocomposites, while the detection of the reactive oxygen species in solution showed that holes and •OH radicals are the main species involved in the photodegradation process.

In the Chapter 4 a novel system composed by a Bipolar Membrane (BMP) and the combination of cadmium sulfide (CdS) and palladium (Pd) nanostructures are used for the degradation of phenolic compounds in water. The combination of CdS and Pd in the different sides of the membrane improved the photocatalytic activity of the system, that resulted from the simultaneous oxidation of 4-chlorophenol and the reduction of 4-

nitrophenol under visible light irradiation. The choice of these compounds allows to obtain a mechanistic insight into the sequential electron transfer between segregated phases embedded in the membrane.

The Chapter 5 summarizes the results obtained throughout this study and outlines possible future developments and related applications.

CHAPTER 1: GENERAL INTRODUCTION

1.1 Water Scarcity and Water Pollution

Water is essential for all forms of life on Earth. All human beings need to consume 3-4 liters of fresh water daily to sustain life and almost 100 liters per person per day for human related activities (domestic, municipal and agricultural use).[1,2] However, over of 97% of water is seawater, unsuitable for drinking and for most of agricultural porpoises. From the rest available resources, 2% of the earth's water is stored in as a fresh water in glaciers, ice caps and snowy mountains. That leaves 1% of the earth's water available to humans daily water supply needs. Most of this remaining quantity is stored in the soil (aquifers) or bedrock fractures beneath the ground (ground water) or in lakes, rivers, and streams on the earth's surface (surface water).[3]

Fresh water is used for a variety of purposes. In particular, agricultural uses represent the largest consumer of fresh water, about 42%. Approximately 39% of fresh water is used for the production of electricity; 11% is used in urban and rural homes, offices, and hotels; and the remaining 8% is used in manufacturing and mining activities.[3,4] In this context, the capacity of a continuously growing population to safeguard suitable access to adequate quantities of water is already at risk and the situation will become worse in the next few decades.

Clean water scarcity is the main issue in today's world of 7.7 billion people. Fresh water demand is expected to continuously increase, as the world population will growth about 22-34% by 2050.[5] This strain will be aggravated by unequal population growth in different

regions of the world, first in Africa or in Asia where scarcity of fresh water is even now a major issue. In fact, many countries are already experiencing water scarcity, with the estimation that the global population who lives in potential water-scarce area, to increase from 27% (in 2010s) to 58% by 2050.[5,6]

While water demand is increasing, the water availability is shrinking due to the scarcity of resources and the water pollution, which is correlated with the population density and the economic growth. At present, in the developing countries the 90% of sewage is directly discharged in the environment untreated, and the 12% of the world's population drinks water from unimproved and unsafe sources.[5] Despite the improvement in living standards related to a rapid urbanization, which plays a significant role in human civilization, the industrial and intense agricultural activities have introduced large quantities of chemicals in the environment causing potential harm in the entire ecosystem. The list of contaminants, that can be found in water will increase dramatically over the years and includes dyes, pesticides, surfactants, chloro-organics compounds, personal care products, detergents, fragrances, flame retardant, industrial chemicals and cleaning agents.[7]

In the face of ever-growing demand, wastewater is gaining momentum as a reliable alternative source of water, shifting the paradigm of wastewater management from "treatment and disposal" to "reuse, recycle and resource recovery". In this sense, wastewater is no longer seen as a problem in need of a solution, rather it is part of the solution to challenges that societies are facing today. For that reason, the scientific community puts a lot of effort to figure out new solutions and procedures to reduce the presence of pollutants in water. These water remediation methods are summarized in three

main categories: (1) physical processes, such as filtration, sedimentation, distillation and adsorption; (2) biological processes where are used living systems (i.e. bacteria, algae, plants) for the decomposition of the pollutants; (3) chemical processes, such as flocculation, chlorination and the recently developed advanced oxidative processes (AOPs).[8–12] In order to reach the goals of water quality improvement and water resources protection, individuals and organizations responsible for various aspects of wastewater management need to comply and act in the collective interest. An effective plan is required to guarantee the availability of clean and affordable water. For this reason, one of the goals reported in the Agenda 2030 of United Nations is focused on the definition of actions to ensure availability and sustainable management of water and sanitation for all (Goal 6). All the States by 2030 have to improve the quality of water by reducing pollution, eliminated dumping and minimizing release of hazardous chemicals and materials, halving the proportion of untreated wastewater and substantially increase recycling and safe reuse.

1.2 Sources of Organic Pollutants in water

There are various types of organic pollutants in water (organic, inorganic, pathogenic and radioactive pollutants). Due to their huge variety, organic pollutants are the main contributors to the environmental pollution. In general, they are found in various wastewater sources, such as: domestic, industrial and agricultural sectors, and their composition depends on the wastewater type, ranging from pharmaceutical and personal care products to persistent organic pollutants (insecticide, pesticide, oil, fertilizers, pharmaceutical compounds and personal care products).[1,13]

The domestic wastewater is water that derives from daily human activities and the wastewater quantities depend on the water consumption rate per population density. The constituents of the domestic wastewater are soaps, cleaning detergents, dental care products, hair colorants and others personal care products (which include: sodium, phosphorous and nitrogen based chemicals).[14] Another important source of organic pollutants is the industrial wastewater. Industrial activities cause the release a huge amounts of chemicals into the rivers, lakes and coastal areas. There are many types of organic pollutants in the industrial wastewater produced from textile, pharmaceutical, oil refining, pesticide, cosmetic to food industries.[15]

The agricultural sector is also identified as one of the most important sources for organic pollutants in wastewater that can affect the environment. These pollutants are related to the by-products of anthropogenic activities in the agricultural area such as fertilizers, animal manure and agrichemicals. The organic pollutants produced from agricultural activities can be found in the surface water and the ground water.[16,17]

Considering the several types of organic pollutants and focusing on the aims of this dissertation will be discuss in the next paragraph the organic dyes and pesticides.

1.2.1 Organic Dyes

A dye is a colored substance that chemically bonds to the substrate where it is applied.[18] All industries (starting from textile to food-packaging industries) use dyes for the production of desired color product. Dyes can be classified in natural and synthetic. The first ones are derived directly from roots, berries, leaves, wood and lichens while the second

ones are made from petrochemicals and earth minerals via chemical reactions. Synthetic dyes are more popular because of their lasting color pay-off and wide range of colors. Natural dyes do not compromise the environment and can be self-degraded; while the synthetic dyes when released into the environment are a source of pollution.[19,20]

Dyes possess color because they:

- absorb light in the visible spectrum (400-700 nm)
- have at least one chromophore group
- have a conjugated system with alternate single and double bonds
- exhibit resonance of electrons

Considering that, the dyes are used by several industries for the production of the final products, they can be found in wastewater and finally in the water systems, and even if in low quantities, they affect their quality and compromise their utilization for human purpose. In fact, most of the synthetic dyes have a complex molecular structure (see Figure 1 where some common synthetic dyes are presented); they are extremely toxic with a low degradation rate in the environment.[18] Moreover, some organic dyes are bonded with heavy metals (Zn, Pb, Cu, Cd, Co), amines, and aromatic compounds. Indeed, organic dyes are not only harmful to aquatic life but also mutagenic to humans, even at a low concentration of 1 ppm.[1,21] The health problems related to organic dyes are skin irritation, sore eyes, carcinogenicity and dysfunction of the brain level and reproductive system, and mutagenicity.[1,13]

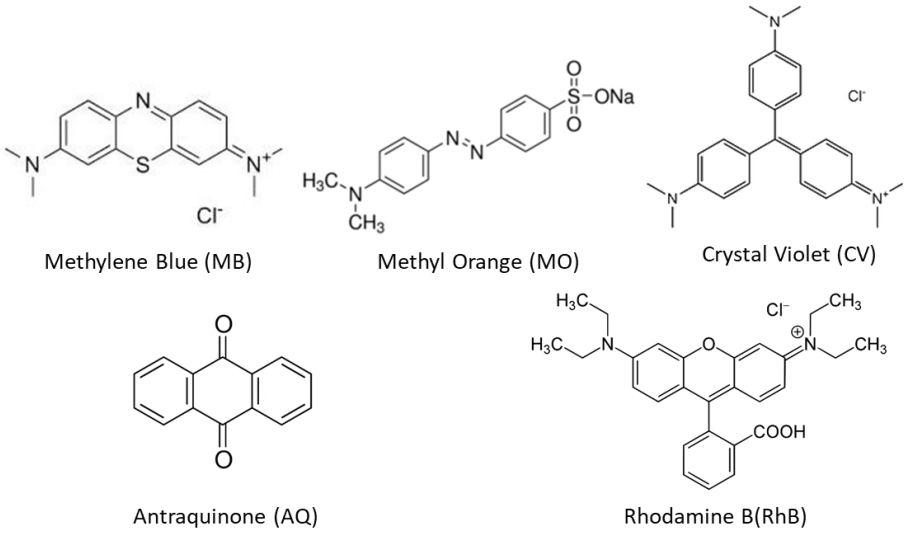

Figure 1. Common dyes found in wastewater.

The removal of these dyes from water is a challenging issue due to their high solubility and high persistence in the environment. For this reason, many efforts have been made to develop new technologies for the removal of the dyes from water through photocatalytic degradation, adsorption, and electro-oxidation and reverse osmosis processes.[18,22] The photocatalytic process is one of most promising solutions because it is non-toxic, not expensive and does not affect human life.

1.2.2 Pesticides

Pesticides are substances that kill or otherwise control the growth an unwanted organism.[23] All chemical pesticides share the common property of blocking a vital metabolic process in the organism, they present long half-lives and are persistent in the environment.[21,23]

The high resistance property under biological degradation is the main reason of the bio-accumulation of the pesticides into animal bodies through the food chain. They are

classified into different categories on the basis of their origin and the type of pest they target.[24] Chemical pesticides such as insecticides, herbicides and fungicides are commonly used in agricultural fields. However, the excessive use of these agrochemicals have adverse effects on environment such as reduced population of insect pollinators, threat to endangered species and habitat of birds. Upon consumption, chemical pesticides also cause various health problems such as skin, eye and nervous system related problems and cancer upon prolonged exposure.[25,26] These contaminants are widely present in air, water, soil and migratory species, which move across the international region. The most common category of pesticides is the organochlorine based pesticides such as dichloro-diphenyl-trichloro ethane (DDT), or chlorinated biphenyls (PCBs), mainly used in agriculture or derive from industrial by-products (Figure 1.1).[1,27]

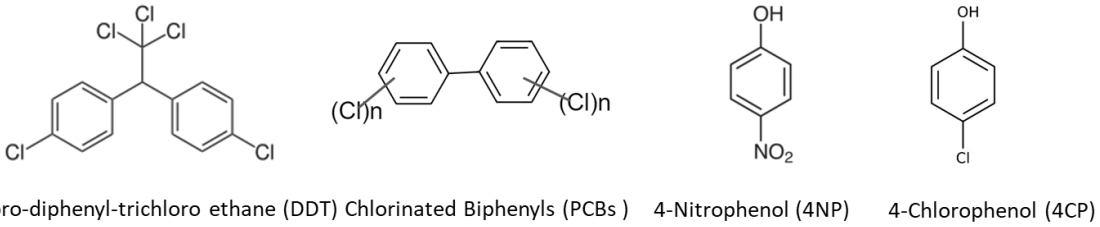

Dichloro-diphenyl-trichloro ethane (DDT) Chlorinated Biphenyls (PCBs) 4-Nitrophenol (4NP) 4-Chlorophenol (4CP)

Figure 1.1. Principal class of pesticides found in wastewater.

Various remediation techniques have been developed so far in order to remove pesticides from water based on surface adsorption, membrane filtration and biological degradation.[28] However, slow response, low specificity and sensitivity are some of the drawbacks of such techniques. In the last years, nanotechnology has emerged as a powerful tool for the sensing and remediation of pesticides. Different types of nanoparticles, viz. metal nanoparticles, bimetallic nanoparticles and metal oxide nanoparticles; nanotubes

such as carbon nanotubes and halloysite nanotubes have been used for the detection, degradation and removal of pesticides using different types of method starting from the adsorption to the photodegradation process.[21,29]

1.3 Common Wastewater Treatment Processes

Wastewater must be treated in order to be disposed in the ambient without causing harm to the environment and to the human health. As reported in the Figure 1.2, there are several methods used at the different stages of the wastewater treatment process. These can be classified as physical methods, such as membrane-filtration processes (nano-filtration, reverse osmosis, electrodialysis) and sorption techniques; chemical methods, such as coagulation, flocculation, conventional oxidation methods (with ozone), irradiation or electrochemical techniques, and biological methods such as aerobic and anaerobic microbial degradation and use of pure enzymes.[30,31]

In general, the decontamination process starts with physical and mechanical pre-treatment of the wastewater, to eliminate debris, followed by the primary treatment, which involves the partial elimination of solid and organic matter by physical and chemical methods, such as precipitation and coagulation (as reported in the Figure 1.2).

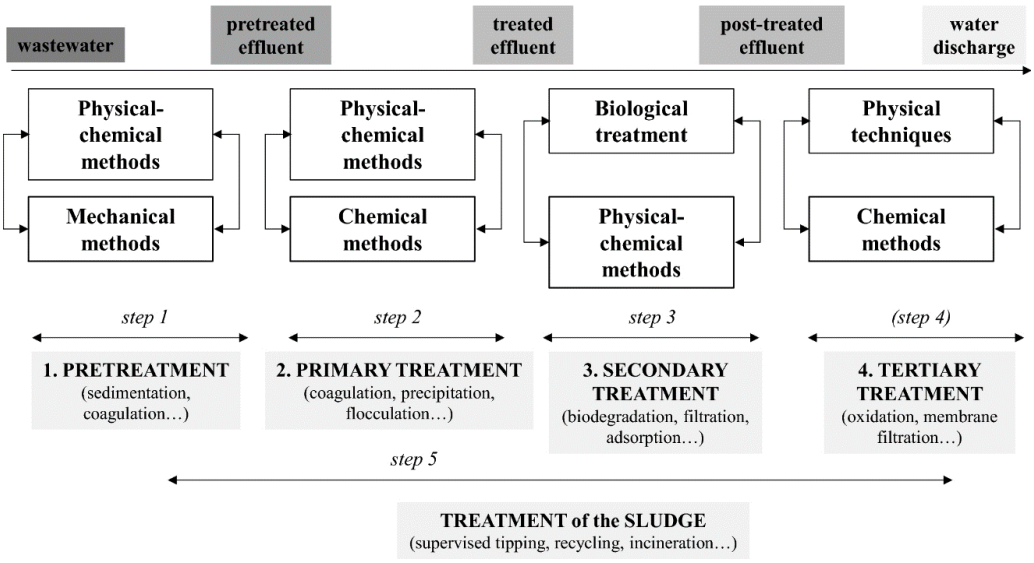

Figure 1.2. Main processes for the decontamination of industrial wastewaters.[30]

Then the treated effluent is subjected to the secondary treatment, where the dissolved and suspended solid matter is removed by chemical and biological treatment. In this step, the biodegradable organic matter is removed by aerobic biological treatment, which includes the use of micro-organisms or activated sludge.[8,29] The effluent is subjected to a tertiary treatment before being discharged in the environment. Tertiary treatment involves physical and chemical techniques to improve the quality of the water. The dissolved solids, organic compounds and heavy metals are removed with advanced wastewater treatments, such as oxidation processes, which involve the use of membrane or adsorbents.[11,32,33] However, common wastewater treatments at this stage are ineffective to remove several chemical compounds because the conventional wastewater treatments are aimed to treat specific effluents and they are not able to remove emerging pollutants.[12,34,35] For these reasons the optimization of existing processes and their combination with new treatment techniques in the tertiary treatment could be a good solution to improve the quality of water after the

overall process. In particular, as can be seen from the Figure 1.2 the stage (3) and (4) of the waste water treatment are the core of the whole procedure and various methods, based on different technologies, are used during these phases for the decontamination of wastewater.

A promising and environmental friendly technique based on AOPs can be used for the treatment of contaminated and industrial wastewater. Glaze et al. in 1987 were the first to define the AOPs methods and then utilize them in the wastewater treatment field.[36] Subsequently, several research studies on the wastewater treatment using AOPs were presented, indication that such methods are very promising for the wastewater treatment.

AOPs are based on the *in-situ* generation of highly reactive species ($OH^{\bullet}$, $O_2^{\bullet -}$) which are able to mineralize organic contaminants into relatively harmless compounds (CO_2, H_2O). AOPs include chemical oxidation (O_2, Fenton reagents), photochemical oxidation (UV/O_3, UV/H_2O_2) and heterogeneous photocatalysis (UV-Vis/NPs).[11,37] Among those, heterogeneous photocatalysis is an attractive method, because of the possibility of generating powerful reactive radicals under irradiation without the need of additional chemicals. The mild operation conditions of temperature and pressure and the use of inexpensive reagents, of free light-source and stable catalysts are particularly attractive for applications in the wastewater treatment processes. AOPs have many advantages, such as:

- Contaminants are directly destroyed in water, rather than simply coagulated or filtrated from the water, thus the secondary pollution can be avoided.

- No harmful compounds are generated after the process, just CO_2 and H_2O or small inorganic ions.

- The AOPs are suitable for the degradation of a wide range of contaminants including some inorganics and pathogens.

1.4 Photocatalysis

Photocatalysis is a process, during which, a chemical reaction is accelerated in the presence of a catalyst upon light exposure.[1,38] The photocatalyst participates in the chemical reaction without being consumed. Depended on the physical state of the reactants and catalyst, the photocatalytic process can be of two types: homogenous or heterogeneous.[1]

Homogenous photocatalysis is the process where the photocatalyst is in the same phase (gas, solid, liquid) with the reactant. The process is activated upon exposure to light, with the photocatalyst promoted to an excited state forming strong reductant and oxidant species by the presence of other agents. Even though homogenous photocatalysis has a high oxidation capability, it is not popular in photocatalytic applications. This is because it is difficult to separate the photocatalysts from the solution, the photocatalysts have a low possibility to be reused, and the purification of the reactants involved during the process is necessary after the process.[39]

Considering the aim of this dissertation the heterogeneous photocatalysis will be discussed in detail in the next paragraph.

1.4.1 Heterogeneous Photocatalysis

Heterogeneous photocatalysis is a process, which includes different types of reactions, such as oxidation, dehydrogenation, hydrogen transfer and gaseous pollutants removal.[33,40,41] In the heterogeneous photocatalysis, the catalyst is in a different phase

with respect to the reactants, in general in suspended form or in a immobilized state.[40] Based on their band-gap energy, materials are classified in three categories (see Figure 1.3). Specifically in crystalline solids composed of *N* atoms the decreased interatomic spacing results in the coupling between adjacent atoms with discrete electronic energy levels and in the overlapping of their atomic wave functions, and consequently in the formation of continuous energy bands of discrete but closely spaced energy levels. The external energy level completely filled with electrons is called valence band (VB), while the upper vacant level is called conduction band (CB). The forbidden gap between VB and CB is called band-gap energy (Eg).[42,43] The properties of a solid depend on the energy bands position and with the distribution of electrons in each band.[43,44] Considering this a crystalline material can be classified as insulator, semiconductor or conductor.[41,42]

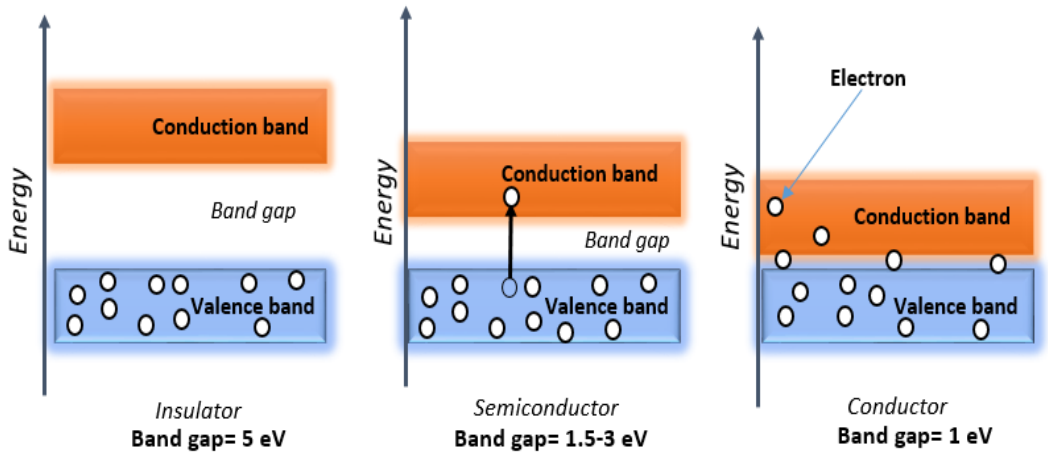

Figure 1.3. Three basic categories of materials based on band gap energy. An insulator has a large band gap so electrons cannot jump from the valance band (VB) to the conduction band (CB). In the semiconductor materials, the band gap is narrower so the electron can lift in the conduction band. In a metal or a conductor, there is no band gap, so the electrons can easily jump from each bands.

Normally, the heterogeneous photocalyst are semiconductor materials, typical metal oxides (MO_x) such as oxide of titanium, zinc, tin, tungsten and vanadium, as shown in the Table 1.1 where are presented the typical photocatalysts with their band gap energies.

Table1.1 Common photocatalysts for photocatalytic processes

Photocatalyst	**Band-gap (eV)**	**Spectral region**
ZnO	3.30	UV
TiO_2	3.24	UV
SnO_2	3.60	UV
CeO_2	3.10	UV
CdS	2.40	UV and Visible

During the photocatalytic degradation process, the photocatalyst is activated through a light source, and a series of chemical reactions occur on its surface, where the reactants are

adsorbed, such as oxygen reduction and oxidation of organic compounds. The photocatalytic process can be dived in five independent steps (Figure 1.4):

1. Mass transfer of reactants from the bulk phase to the catalytic surface.
2. Adsorption of reactants
3. Photocatalytic process:
    a. Light adsorbed by the catalyst
    b. Formation of electron/hole pairs
    c. Migration of free charges, which induce the reactions.
4. Product desorption.
5. Mass transfer of the products from the interfacial region to the bulk.

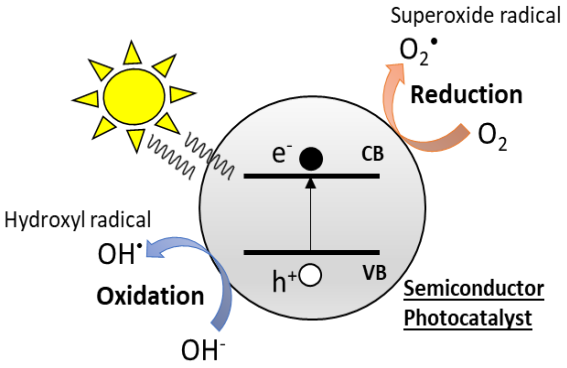

Figure 1.4. Diagram of heterogeneous photocatalytic steps. The photocatalysts can absorb protons to generate electrons and holes. In the oxidation site, the reaction between the positive charged holes and water generate hydroxyl radicals (•OH). In the reduction site the dissolved oxygen molecules can generate the short-lived super oxide anion radicals ($\bullet O_2^-$). These radicals are the crucial species for the degradation process.

A crucial aspect is the activation of the semiconductor materials by adsorption of a photon with energy greater or equal to the band gap energy ($h\nu > E_g$).[45] This will lead to a separation of electrons (e^-) and holes (h^+) by the promotion of e^- from the VB to the CB (eq. 1.1). The e-/h^+ pairs formed participate in several oxidation and reaction processes at the catalyst

surface with the adsorbed organic species (R) (eq. 1.2-1.5), in order to promote their decomposition.[45]

$$MO_x + hv \rightarrow MO_x (e^- + h^+) \quad (1.1)$$

$$e^- + O_2 \rightarrow O_2^{\bullet -} \quad (1.2)$$

$$h^+ + OH^- \rightarrow OH^{\bullet} \quad (1.3)$$

$$R\text{-}H + OH^{\bullet} \rightarrow R^{\bullet} + H_2O \quad (1.4)$$

$$R + h^+ \rightarrow R^{+\bullet} + \text{intermediate/final products} \quad (1.5)$$

The formation of $O_2^{\bullet -}$ leads the formation of hydroperoxyl radicals ($HOO^{\bullet}$) and hydroxyl peroxide H_2O_2 (eq. 1.6-1.8). These species act as scavengers during the photocatalytic process improving the reaction rate.[46]

$$O2^{\bullet -} + H+ \rightarrow HOO^{\bullet} \quad (1.6)$$

$$HOO^{\bullet} + e- \rightarrow HOO^- \quad (1.7)$$

$$HOO^- + H^+ \rightarrow H_2O_2 \quad (1.8)$$

These types of reactive oxygen species (ROS) can oxidize the organic species during the photocatalytic process and convert them into harmless by-products and the final formation CO_2 and H_2O.[46]

1.5 Nanotechnology

Nanotechnology has a key role in integrating chemistry and materials science in order to resolve the main issues of our society. Nanotechnology refers to the study, analysis and applications of materials at the nanoscale, defined as the size range between 1 to 100 nanometers (nm); materials that possess at least one dimension less than 100 nm are

defined as nanomaterials.[47] The nanostructured materials (see Figure 1.5) can be classified as:

- zero-dimensional (0-D), which include materials such as nanoparticles (NPs) and quantum dots (QDs).
- one-dimensional (1-D) materials like nanoribbons, nanorods and nanowires.
- two-dimensional (2-D) materials which are nanodisks, nanowalls, nanosheets and nanoplates.
- three-dimensional (3-D) bulk nanomaterials which are composed of a multiple arrangement of nanosized crystals.

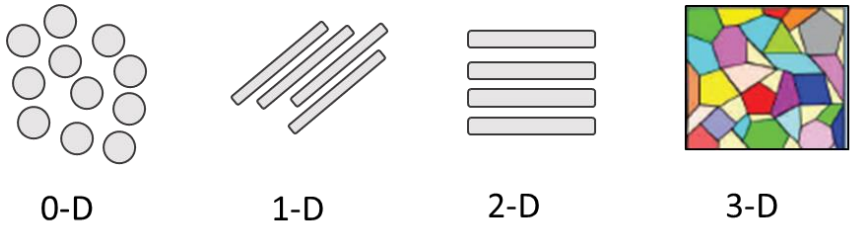

Figure 1.5. Classification of nanomaterials according to the dimensionality of nanostructures.[48]

Several types of nanomaterials have been used for water remediation, and in particular for the removal of toxic pollutants such as heavy metal ions, radioactive nuclides, organic and inorganic compounds.[2,49] The extensive use of nanomaterials in this field is due to their high surface area, and the possibility to control the size, morphology and chemical structures that affect the optical, adsorptive and catalytic properties.[47,48] The challenges associated with the treatment of water influenced researchers to explore nanotechnology and promote research in this field, as demonstrate by searching general keyword including

"nanostructures", "nanoparticles", "nanocomposites", "wastewater" and "treatment" as can be seen in the Figure 1.6.[50]

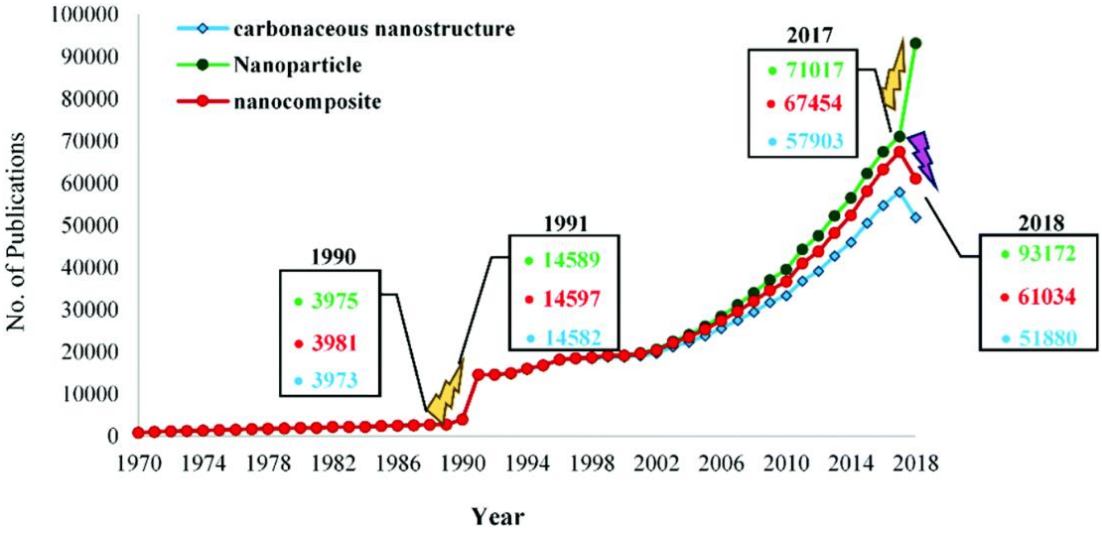

Figure 1.6. Number of publications by searching keywords including "nanostructures", "nanoparticles", "nanocomposites", "wastewater" and "treatment" during the period 1975-2018.[50]

An ideal photocatalyst is photo-stable, chemical inert, not hazardous for human and environment and available at an affordable cost. Several semiconductor nanoparticles have been reported as promising for water treatment such as: TiO_2, ZnO, SnO_2, CdS, CdSe, MoS_2 which are the most used (see Table 1.2).[44,51–53] The overall photocatalytic activity of metal nanoparticles (NPs) depend of their crystalline structure, surface area, density of surface hydroxyl groups and adsorption/desorption characteristics.[41]

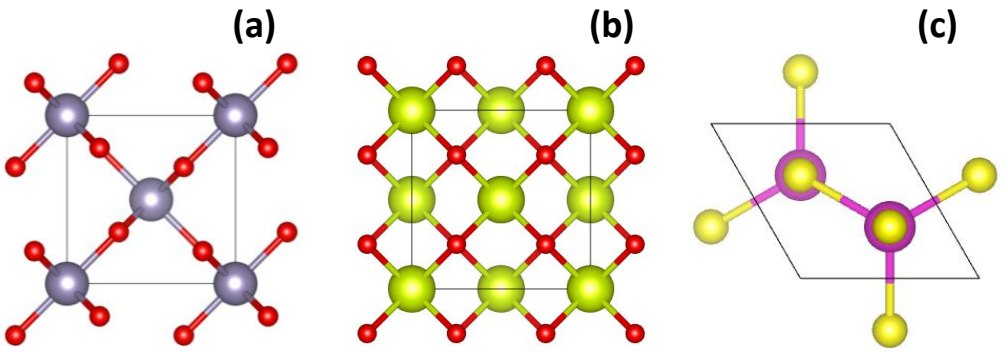

Figure 1.7. Crystal lattice structure of (a) tetragonal SnO_2, (b) cubic CeO_2 and (c) tetrahedral CdS.

The most common semiconductor catalysts used for photocatalytic processes are titanium dioxide (TiO_2) and zinc oxide (ZnO). They both have similar bandgaps (see Table 1.1), charge carrier mobility, low toxicity and low cost. In the last years, other types of semiconductors such as tin dioxide (SnO_2), the ceria (CeO_2) and cadmium sulfide (CdS) are also being explored and used in the decomposition of environmentally harmful compounds and toxins in wastewater. In fact, based on the fact that TiO_2 and ZnO have received the greatest attention in the water treatment research, the next paragraphs will be focused on the description of other emerging semiconductor nanomaterials that are more recently used in water remediation process such as SnO_2, CeO_2 and CdS. These nanostructures have a great potentiality to be used in water related applications and based of the fact that are not sufficiently explored for such application, the present PhD thesis is focused the exploration of their properties for wastewater applications.

Tin (IV) oxide or stannic oxide, is an n-type semiconductor , transparent in the visible up to the edge of the ultraviolet region of the solar spectrum, with a wide band-gap (E_g =3.6 eV) (wavelength of the absorption edge λ=350nm), and chemical stability and structure very similar to those of TiO_2 (rutile).[51,54,55] The rutile crystal structure of SnO_2, also known

as *Casserite,* has a tetragonal unit cell where the tin (IV) atom is surrounded by 6 oxygen atoms and every oxygen is bonded by 3 tin (IV) ions (see Figure 1.7 (a)).[55,56] The SnO_2 can be prepared by different techniques (e.g. microwave, hydrothermal, precipitation, sol-gel, electrodeposition, and chemical vapor deposition), with the resulting materials to be NPs of controlled-shaped with a large surface-area.[57–60] Furthermore, SnO_2 has no adverse health effects and is poorly adsorbed by the human body when inhaled or injected, as reported by Kim et al.[52]

Cerium dioxide or ceria (CeO_2) are promising NPs for wastewater treatment, used in a variety of applications ranging from oxygen sensors, fuel cells to therapeutics.[61,62] Ceria shows excellent ability to form oxygen vacancies due to the ability to alternate between the Ce^{4+} and Ce^{3+} oxidation states, and to drastically adjust its electronic configuration, and therefore its bandgap, according to its immediate environment.[63,64] The crystal structure of CeO_2, is composed of one cerium ion bonded with 8 oxygen ions, while each oxygen atom is four-fold coordinated (see Figure 1.7 (b)), with a face-centered cubic *(fcc)* fluorite lattice.[65] Furthermore, the growth process of CeO_2 NPs is easily controlled such that can maintain their small particles size and uniform morphology. CeO_2 NPs show interesting properties such as: strong oxidant capacity, long-term stability, non toxicity and high electron transfer capability, and for that is a promising material for photocatalytic applications.[62,66,67]

CdS is another promising material for photocatalytic applications. In particular, CdS has a long charge carrier diffusion length up to the micrometer scale with a bandgap of 2.4 eV, which is beneficial for the charge separation.[68] Considering its band-gap, CdS exhibits

excellent photochemical properties and quantum efficiency in the visible light region. CdS has two crystal structures; cubic and hexagonal (see Figure 1.7 (c)). In term of crystal morphology, the cubic crystal, also known as the zinc blend phase shows a tetrahedral structure, while the hexagonal structure shows a wurzite phase and the presence of these phases depends of the temperature used during its synthesis.[69] However, CdS suffers from severe photo corrosion under light illumination; and for that usually is covered with other types of semiconductor or protective layers to improve the stability under illumination.[70]

1.6 Doping of Semiconductors

Several structural modifications of the metal NPs can be made in order to improve the visible light absorption of the semiconductor photocatalysts, in fact the semiconductor nanomaterials are unable to adsorb the visible light, their peak adsorption according to their E_g (see Table 1.1) are deep in the UV region of the solar spectra. UV light is only 5% of the sun's energy, while the visible light accounting for the vast majority of the solar irradiation. In order to use the semiconductor material for realistic application in water treatment technology it is necessary the coupling with noble NPs to improve its photocatalytic performance and suppress electron-hole (e^-/h^+) recombination. One popular route in the introduction of noble metals such as Ag, Au, Pt and Pd onto the surface of the semiconductor NPs.[71,72] The catalytic properties of the noble metal NPs depend to a large extent on their size, geometry, and distribution, as well as on the interactions between them and the semiconductor NPs.[71]

During the irradiation, the key process is the charge separation mechanism, where the electrons are transferred from the CB to the VB and the consequently formation of holes, as reported in the Figure 1.4. The enhancement in the photocatalytic activity of the semiconductor can be explained by the decrease in the band/gap or the addition of intra/band gap states by the dopants. As the Fermi's levels of the plasmonic nanomaterials are lower with respect to the semiconductor, the photo-excited electrons can easily jump to the conduction band. Therefore, the e^-/h^+ recombination is not favorable in this case, resulting in the effective charge separation and the enhancement of the photocatalytic performance (as reported in the Figure 1.8).[73–75]

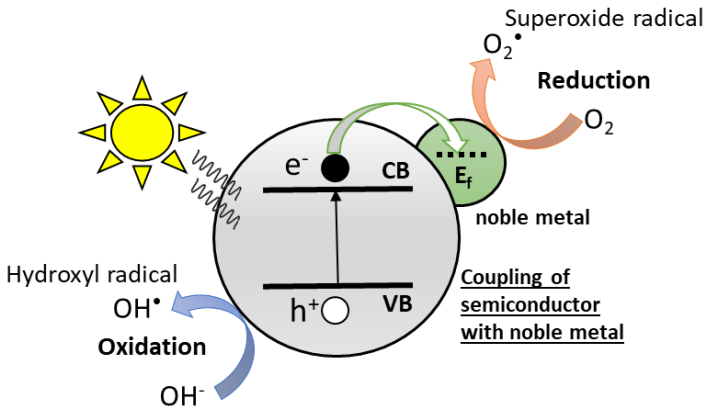

Figure 1.8. Diagram of heterogeneous photocatalytic steps by the presence of semiconductor catalyst coupled with noble metal.

When a plasmonic metal is in contact with n-type semiconductor a downward bending of the conduction band of the semiconductor will occur, resulting in the formation of Schottky barrier as can be seen in the Figure 1.8. This barrier functions as a filter allowing to the hot electrons with sufficient energy to pass across the metal/semiconductor interface, resulting in effective e^-/h^+ separation.[74] Moreover, to facilitate the hot electron injection, proper

alignment of the conduction band edge of the semiconductor with respect to the Fermi level of the plasmonic metal is required. The co-catalyst leads to a longer life-time of the charge carries and enhances the formation of ROS species in order to improve the catalytic performance.[71,72] The combination between these nanostructured materials allows to the hybrid structure to absorb the visible light (80%) from the solar spectrum.[73]

1.7 Polymer Nanocomposites, an alternative approach for water treatment

Although the NPs possess large surface area and can effectively act as photocatalysts of organic pollutants, they are not simple to manipulate, transport and recover when they are used in water remediation applications. On the top, due to their general tendency to aggregate in liquids, a significant reduction of their surface area may occur and therefore their catalytic activity may be significantly affected. Therefore, the stabilization of the NPs is essential for their good photocatalytic performance, and for this purpose, different substrates have been used, such as glass, metal plates, carbon derivatives and polymers. Among them, polymers are good host materials, as they confer flexibility and usability to the final material.[76,77] Although the use of nanomaterials have many applications even in the photocatalysis with a good photo activity, the impact on the aqueous environment of accidentally discharged nano-sized materials strongly limits their usability in real-world applications. The harmful effects of nanomaterials on aquatic organisms has been fully demonstrated and their toxicity has been connected to the concentration, exposure time and reactivity of the nanomaterials in water bodies.[61] Another limitation of the use of free nanomaterials is their recovery from the treated water, which usually do not result in their complete removal. Therefore, the potential risks on the ecosystems and on the human health, together with the

difficulties in separation and effective collection of the nanomaterials, have led to the development of composites for the immobilization of nanomaterials. The immobilization of the photo-active nanomaterials on a porous polymeric matrix allows the fabrication of functional solid composites, preventing their loss in the environment. The formation of an interconnected porous matrix ensures a high surface area material, in which organic pollutants can interact with a high number of active sites. Polymeric material and polymeric membrane have been recently proposed as supports for nanomaterials due to their low weight, flexibility and easy handling characteristic.[78]

Polymer nanocomposite supports with high surface area can be formed through two different methods: the bottom-up and the top-down approach. In the top-down approach, the preparation involves a simple mixing of the melt polymer solution and the NP fillers. This approach has a main drawback: the strongly tendency of the NPs to agglomerate leading a non-homogenous final product.[79] To overcome this limitation and reach a good NPs dispersion the bottom-up approach can be used. In this approach, the polymer matrix and the filler precursor are dissolved together in a suitable organic solvent. The use of precursor, instead of the pre-formed nanomaterial, leads to a lower viscosity and deeper phase mixing.[79,80] The consecutive light or thermally induced conversion of the precursor, results to the *in-situ* formation of NPs directly in the macromolecular solid phase. Among the many techniques reported in literature, the preparation of fibrous materials by electrospinning is one of the most promising for water treatment remediation because of the presence of a porous network and the handily properties of the nanocomposites.[81]

However, in most cases, the fabrication processes of the fibrous nanocomposite mats require multi-step procedures comprising the preparation of NPs and the subsequent dispersion in the polymeric solution before the electrospinning process. This may result in

mats with limited photocatalytic activity as it is expected the formation of agglomerates and a limited quantity of exposed NPs on the mats' surface. Alternatively, for the fabrication of fibrous mats for photocatalytic applications, the polymeric matrix has, often, a "sacrificial role" and it is eliminated during the conversion of the precursor salt in metal oxide NPs ($T>T_g$) by intense thermal treatment.[77] Following such approach, the final inorganic materials lose their favorable mechanical characteristics, which are usually offered by the presence of the polymer, compromising their usability.

As demonstrated by several research papers, the great interest and advantages of using polymers as support combining with the *in-situ* method provide a homogenous distribution of NPs on and in the internal porous network of the polymers.[81,82] Following this approach, recently, several types of nanocomposites are used as hosts for the thermal or photochemical conversion of semiconductor and metallic precursor salts for the photocatalytic degradation of organic dyes and pesticides. Different types of precursor can be used for this purpose, Morselli et al reported the incorporation of Cerium nanoparticles (CeNPs) in the poly(vinylidene fluoride-co-hexafluoropropylene) (PVDF-HFP).[82] The fibrous membranes were fabricated combining the electrospinning and the *in-situ* synthesis of CeNPs directly in the electrospun polymeric fibers by thermal conversion of the precursor salt in CeNPs. Therefore, to improve the catalytic activity of the fibers, gold nanoparticles (AuNPs) were synthesized by thermal treatment directly of the polymeric mats loaded with gold precursor (PVDF/CeO2/Au_in) or ex situ by thermal post treatment after the dipping of the PVDF/CeO2 in a gold precursor solution (PVDF/CeO2/Au_ex) resulting in valuable system with enhanced properties for photocatalytic degradation of

MB in water and bio-applications.[82] In another study, Campagnolo et al developed a system based on poly-methyl methacrylate (PMMA) with gold/zinc-oxide heterostructures. Specifically, the system was fabricated by a two step approach. First, branched ZnO NPs were fixed on PMMA upon the thermal conversion of zin-acetate-loaded PMMA electrospun mats; the doping with AuNPs was done directly on the surface of the mats though an adsorption dipping process, followed by thermal treatment. The authors also investigated the effect of the different loading of AuNPs formed on the surface of PMMA/ZnO fibers, establishing an effective metal-semiconductor interfacial interaction for a concentration of 1 wt% of AuNPs.[83] These nanocomposites have shown a good photocatalytic performance against MB and BPA under UV irradiation with a high degradation kinetic rate as $2.33 \cdot 10^{-3}$ min^{-1} and $1.12 \cdot 10^{-3}$ min^{-1} respectively.[83]

Podasca et al prepared a new type of hybrid nanocomposites, the film was prepared by a photo polymerization of some acrylic monomers with the in-situ generation of AgNPs under UV irradiation. The ZnO NPs were included in the monomer mixture as pre-formed particles before the photo-irradiation process. The final nanocomposites containing Ag/ZnO NPs with different ratios was employed for photocatalytic decomposition of MB in ethanol or water under UV and Visible light irradiation. The same group reported recently the in situ generation AgNPs in polypyrrole polymer induced by the photo generation technique, and with the presence of ZnO in the monomer solution. In this case, the film was used for the photocatalytic degradation of RhB in water under visible light irradiation.[84]

1.7.1 Polymers matrix with metal oxide NPs for photocatalysis

Polymers play a key role in the stabilization of the catalyst. Both of synthetic and natural polymers can be used as host matrices for the preparation of nanocomposites.

When combined with semiconductor NPs, acrylic polymers and copolymers, vinyl polymers, organosilicon compounds and fluorinated polymers are the most used as host matrices. However, the presence of NPs in the matrix could enhance the aging process of the polymer due to the photocatalytic action compromising the overall performance of the nanocomposite.[85]

On the other hand, natural based polymers stand out from synthetic ones because they are renewable, biocompatible and biodegradable. Even if their availability is lower compared to the common petrol polymer derivatives and require sophisticated extraction methods to obtain them, this kind of polymer is a good choice to develop eco-friendly materials.[86,87] The most common natural polymers used are alginate, chitosan, guar gum, dextrin, cellulose, starch and bio-based materials deriving directly from lignin. Lignin and cellulose materials are biocompatible and do not present harmful effects in the human body.[86,88] In fact, the Unites States Food and Drugs Administration (FDA) approved the use of some types of cellulose and lignin based polymers in the pharmaceutical pills for drug delivery and food packaging.[89] In this scenario, their use for photocatalytic applications against pollutants in water have attracted considerable scientific attention in the last years.

Various research activities have employed bio-based polymers for the degradation of organic pollutants in water. In this context, Linda et al.. demonstrated that the inclusion of cellulose in poly-vinyl chloride (PVC) by the presence of ZnO can degrade congo red

(CR) and crystal violet (CV) dyes under UV irradiation, with an efficiency close to 90% after 120 and 90 min of irradiation respectively.[90] Chen et al. fabricated a porous cellulose hydrogel/graphite oxide/TiO_2 NPs composite for the adsorption and photodegradation of MB reaching a value of 90%[91]. Ali et al. synthetized a CA nanocomposite filled with ZnO and black carbon nanoparticles (named ZCA) in which they deposited bimetallic Cu-Ag nanoparticles for the degradation of MO, CR, MB and RhB dyes by the presence of $NaBH_4$. The highest catalytic activity showed values between 89% and 98% after up 19 min of irradiation.[92] All the above-mentioned studies prove the versatility of cellulose and its derivatives to form composites materials by the presence of NPs and promote the degradation of dyestuffs.

In detail, in the last fifteen years a total of nineteen scientific articles based on lignin and cellulose nanocomposites have been reported and focused onto the degradation of organic pollutants in water with metal NPs by using $NaBH_4$ catalyst or photocatalytic techniques.[86] Among them, 84% used cellulose and its derivatives as polymer matrix, and studied the photodegradation process, using as light source the UV (73%), the visible light irradiation (20%) and the rest 7% directly the solar irradiation (7%). The most used semiconductors were metal oxide NPs, with the TiO_2 the most used for photodegradation process.[86] However, during the 2020 bio-based lignin materials were also used for the preparation of nanocomposites. This demonstrates that the wastewater treatment using bio-based polymer composites for the photocatalytic decontamination of wastewater is an interesting issue currently under investigation right now from the scientific community.

1.8 Research Aim and Scope

The previous chapters introduced a general overview of the photocatalysis and its potential role in wastewater treatment. Specifically, the first section introduced the wastewater sources and the water scarcity. In the second part an overview of the different types of pollutants is presented, and are described the different techniques which are currently used for their removal and degradation. More attention is paid to the AOPs, in particular the heterogeneous photocatalytic mechanism, and to the formation of ROS which play a key role in the photodegradation process. The last part of this chapter is focused on the use of nanomaterials and polymeric nanocomposites for photocatalytic applications in water treatment.

Considering these behaviors the aim of this dissertation is the synergic use of nano-photocatalysts and polymeric matrix to develop and characterize different nanocomposites for the photodegradation of organic pollutants in water.

In order to achieve this aim the research objectives of this dissertation are to:

- Explore the use of less studied semiconductor materials such as SnO2, CeO2 and CdS as photocatalyst for water treatment applications and optimize the condition for the synthesis of the metal NPs directly in the polymeric host materials.
- Evaluate the possibility to use a combination of NPs and noble metals in the polymeric host matrix to enhance the photocatalytic activity, under the visible light irradiation, of the final nanocomposites.
- Investigate the modification of the morphology of the obtained nanocomposites and of their chemical properties for an effective photocatalytic performance.

- Evaluate the photocatalytic degradation properties and efficiency of the developed photocalyst and investigate the by-products and the mineralization efficiency after the remediation process.
- Evaluate the kinetic behavior of the photocatalytic process.
- Understand the relationship between structural, physicochemical properties and pollutants adsorption on the nanocomposites with the photodegradation performance.

To reach these goals, different types of semiconductor NPs embedded in polymeric matrices are chosen, such as Tin dioxide (SnO_2), the heterostructure with Cerium dioxide (CeO_2)/PtNCs, and a combination of CdS with PdNPs, which are studied in details.

Chapter 2 addresses the first composites material, which is porous mats prepared through electrospinning procedure using CA as host matrix, the photoactive nanomaterial is directly formed in the polymeric matrix, obtaining a solid porous system. This combination of SnO2 and CA is used to evaluate and demonstrate the possibility of the in-situ formation of semiconductor NPs in the polymer matrix and the its photo activity under UV irradiation is confirmed against two common dyes used in textile industries such as MB and MO. However, the metal oxide NPs are unable to adsorb the visible light, their peak adsorption is deep in the UV region of solar spectrum, which represent only 5% of the sun's energy. In order to improve the light harvesting of the solar spectrum the combination of CeO_2/PtNCs, synthetized by in-situ method and the SCBD deposition on the electrospun CA matrix, is investigated and discussed in the Chapter 3. These nanocomposites are used for the photodegradation of the MB dye under visible light irradiation. In this case, to figure

out the mechanism of the photodegradation, the evolution of ROS species are investigated, with probe molecules, which are responsible of the photocatalytic process against MB dye. In the Chapter 4 a new functionalized photocatalytically active membranes is investigated. In this case a different approach is used, a bipolar membrane (BMP) is used as host materials and the photoactive nanostructures CdS and PdNPs are synthesized directly in the surface of the membrane. The final nanocomposite is tested for the photocatalytic degradation of nitro-phenolic and chloro-phenolic compounds. With this approach, the proof of an electron transfer cascade across a bipolar membrane by the presence of CdS/PdNPs for elevated catalytic turnover and convert these species in non harmful compounds are demonstrated.

1.9 References

(1) *Water Pollution and Remediation: Photocatalysis*; Inamuddin, Ahamed, M. I., Lichtfouse, E., Eds.; Environmental Chemistry for a Sustainable World; Springer International Publishing: Cham, 2021; Vol. 57. https://doi.org/10.1007/978-3-030-54723-3.

(2) Homaeigohar, S. Water Treatment with New Nanomaterials. **2020**, 4.

(3) Boretti, A.; Rosa, L. Reassessing the Projections of the World Water Development Report. *npj Clean Water* **2019**, *2* (1), 15. https://doi.org/10.1038/s41545-019-0039-9.

(4) *Water Reclamation and Sustainability*, First edition.; Ahuja, S., Ed.; Elsevier: Amsterdam ; Boston, 2014.

(5) Tzanakakis, V. A.; Paranychianakis, N. V.; Angelakis, A. N. Water Supply and Water Scarcity. *Water* **2020**, *12* (9), 2347. https://doi.org/10.3390/w12092347.

(6) Albert, J. S.; Destouni, G.; Duke-Sylvester, S. M.; Magurran, A. E.; Oberdorff, T.; Reis, R. E.; Winemiller, K. O.; Ripple, W. J. Scientists' Warning to Humanity on the Freshwater Biodiversity Crisis. *Ambio* **2021**, *50* (1), 85–94. https://doi.org/10.1007/s13280-020-01318-8.

(7) Escoz-Roldán, A.; Gutiérrez-Pérez, J.; Meira-Cartea, P. Water and Climate Change, Two Key Objectives in the Agenda 2030: Assessment of Climate Literacy Levels and Social Representations in Academics from Three Climate Contexts. *Water* **2019**, *12* (1), 92. https://doi.org/10.3390/w12010092.

(8) Muga, H. E.; Mihelcic, J. R. Sustainability of Wastewater Treatment Technologies. *Journal of Environmental Management* **2008**, *88* (3), 437–447. https://doi.org/10.1016/j.jenvman.2007.03.008.

(9) Sonune, A.; Ghate, R. Developments in Wastewater Treatment Methods. *Desalination* **2004**, *167*, 55–63. https://doi.org/10.1016/j.desal.2004.06.113.

(10) Rashid, R.; Shafiq, I.; Akhter, P.; Iqbal, M. J.; Hussain, M. A State-of-the-Art Review on Wastewater Treatment Techniques: The Effectiveness of Adsorption Method. *Environ Sci Pollut Res* **2021**, *28* (8), 9050–9066. https://doi.org/10.1007/s11356-021-12395-x.

(11) Deng, Y.; Zhao, R. Advanced Oxidation Processes (AOPs) in Wastewater Treatment. *Curr Pollution Rep* **2015**, *1* (3), 167–176. https://doi.org/10.1007/s40726-015-0015-z.

(12) Loo, S.-L.; Vásquez, L.; Athanassiou, A.; Fragouli, D. Polymeric Hydrogels—A Promising Platform in Enhancing Water Security for a Sustainable Future. *Advanced Materials Interfaces n/a* (n/a), 2100580. https://doi.org/10.1002/admi.202100580.

(13) Deblonde, T.; Cossu-Leguille, C.; Hartemann, P. Emerging Pollutants in Wastewater: A Review of the Literature. *International Journal of Hygiene and Environmental Health* **2011**, *214* (6), 442–448. https://doi.org/10.1016/j.ijheh.2011.08.002.

(14) McCarty, P. L.; Bae, J.; Kim, J. Domestic Wastewater Treatment as a Net Energy Producer–Can This Be Achieved? *Environ. Sci. Technol.* **2011**, *45* (17), 7100–7106. https://doi.org/10.1021/es2014264.
(15) Li, W.; Mu, B.; Yang, Y. Feasibility of Industrial-Scale Treatment of Dye Wastewater via Bio-Adsorption Technology. *Bioresource Technology* **2019**, *277*, 157–170. https://doi.org/10.1016/j.biortech.2019.01.002.
(16) Oron, G.; Campos, C.; Gillerman, L.; Salgot, M. Wastewater Treatment, Renovation and Reuse for Agricultural Irrigation in Small Communities. *Agricultural Water Management* **1999**, *38* (3), 223–234. https://doi.org/10.1016/S0378-3774(98)00066-3.
(17) Salleh, M. A. M.; Mahmoud, D. K.; Karim, W. A. W. A.; Idris, A. Cationic and Anionic Dye Adsorption by Agricultural Solid Wastes: A Comprehensive Review. *Desalination* **2011**, *280* (1–3), 1–13. https://doi.org/10.1016/j.desal.2011.07.019.
(18) Tkaczyk, A.; Mitrowska, K.; Posyniak, A. Synthetic Organic Dyes as Contaminants of the Aquatic Environment and Their Implications for Ecosystems: A Review. *Science of The Total Environment* **2020**, *717*, 137222. https://doi.org/10.1016/j.scitotenv.2020.137222.
(19) Benkhaya, S.; M'rabet, S.; El Harfi, A. Classifications, Properties, Recent Synthesis and Applications of Azo Dyes. *Heliyon* **2020**, *6* (1), e03271. https://doi.org/10.1016/j.heliyon.2020.e03271.
(20) Almeida Guerra, W. N.; Teixeira Santos, J. M.; Raddi de Araujo, L. R. Decolorization and Mineralization of Reactive Dyes by a Photocatalytic Process Using ZnO and UV Radiation. *Water Science and Technology* **2012**, *66* (1), 158–164. https://doi.org/10.2166/wst.2012.154.
(21) Rawtani, D.; Khatri, N.; Tyagi, S.; Pandey, G. Nanotechnology-Based Recent Approaches for Sensing and Remediation of Pesticides. *Journal of Environmental Management* **2018**, *206*, 749–762. https://doi.org/10.1016/j.jenvman.2017.11.037.
(22) Agboola, O.; Fayomi, O. S. I.; Ayodeji, A.; Ayeni, A. O.; Alagbe, E. E.; Sanni, S. E.; Okoro, E. E.; Moropeng, L.; Sadiku, R.; Kupolati, K. W.; Oni, B. A. A Review on Polymer Nanocomposites and Their Effective Applications in Membranes and Adsorbents for Water Treatment and Gas Separation. *Membranes* **2021**, *11* (2), 139. https://doi.org/10.3390/membranes11020139.
(23) Syafrudin, M.; Kristanti, R. A.; Yuniarto, A.; Hadibarata, T.; Rhee, J.; Al-onazi, W. A.; Algarni, T. S.; Almarri, A. H.; Al-Mohaimeed, A. M. Pesticides in Drinking Water—A Review. *IJERPH* **2021**, *18* (2), 468. https://doi.org/10.3390/ijerph18020468.
(24) Citterio, A.; Sebastiano, R.; Marion, A. *J. Org. Chem.* **1991**, *56*, 5328.
(25) Taha, S. M.; Amer, M. E.; Elmarsafy, A. E.; Elkady, M. Y. Adsorption of 15 Different Pesticides on Untreated and Phosphoric Acid Treated Biochar and Charcoal from Water. *Journal of Environmental Chemical Engineering* **2014**, *2* (4), 2013–2025. https://doi.org/10.1016/j.jece.2014.09.001.
(26) Mojiri, A.; Zhou, J. L.; Robinson, B.; Ohashi, A.; Ozaki, N.; Kindaichi, T.; Farraji, H.; Vakili, M. Pesticides in Aquatic Environments and Their Removal by

Adsorption Methods. *Chemosphere* **2020**, *253*, 126646. https://doi.org/10.1016/j.chemosphere.2020.126646.
(27) Carvalho, F. P. Pesticides, Environment, and Food Safety. *Food and Energy Security* **2017**, *6* (2), 48–60. https://doi.org/10.1002/fes3.108.
(28) Bera, S. P.; Godhaniya, M.; Kothari, C. Emerging and Advanced Membrane Technology for Wastewater Treatment: A Review. *Journal of Basic Microbiology n/a* (n/a). https://doi.org/10.1002/jobm.202100259.
(29) Paździor, K.; Bilińska, L.; Ledakowicz, S. A Review of the Existing and Emerging Technologies in the Combination of AOPs and Biological Processes in Industrial Textile Wastewater Treatment. *Chemical Engineering Journal* **2019**, *376*, 120597. https://doi.org/10.1016/j.cej.2018.12.057.
(30) Crini, G.; Lichtfouse, E. Advantages and Disadvantages of Techniques Used for Wastewater Treatment. *Environ Chem Lett* **2019**, *17* (1), 145–155. https://doi.org/10.1007/s10311-018-0785-9.
(31) Crittenden, J. C.; Suri, R. P. S.; Perram, D. L.; Hand, D. W. Decontamination of Water Using Adsorption and Photocatalysis. *Water Research* **1997**, *31* (3), 411–418. https://doi.org/10.1016/S0043-1354(96)00258-8.
(32) Matamoros, V.; Rodríguez, Y.; Albaigés, J. A Comparative Assessment of Intensive and Extensive Wastewater Treatment Technologies for Removing Emerging Contaminants in Small Communities. *Water Research* **2016**, *88*, 777–785. https://doi.org/10.1016/j.watres.2015.10.058.
(33) Herrmann, J.-M.; Guillard, C.; Pichat, P. Heterogeneous Photocatalysis : An Emerging Technology for Water Treatment. *Catalysis Today* **1993**, *17* (1–2), 7–20. https://doi.org/10.1016/0920-5861(93)80003-J.
(34) Komeily-Nia, Z.; Montazer, M.; Heidarian, P.; Nasri-Nasrabadi, B. Smart Photoactive Soft Materials for Environmental Cleaning and Energy Production through Incorporation of Nanophotocatalyst on Polymers and Textiles. *Polymers for Advanced Technologies* **2018**, *30* (2), 235–253. https://doi.org/10.1002/pat.4480.
(35) Melinte, V.; Stroea, L.; Chibac-Scutaru, A. L. Polymer Nanocomposites for Photocatalytic Applications. *Catalysts* **2019**, *9* (12), 986. https://doi.org/10.3390/catal9120986.
(36) Glaze, W. H.; Kang, J. W. Advanced Oxidation Processes. Description of a Kinetic Model for the Oxidation of Hazardous Materials in Aqueous Media with Ozone and Hydrogen Peroxide in a Semibatch Reactor. *Ind. Eng. Chem. Res.* **1989**, *28* (11), 1573–1580. https://doi.org/10.1021/ie00095a001.
(37) Vilhunen, S.; Sillanpää, M. Recent Developments in Photochemical and Chemical AOPs in Water Treatment: A Mini-Review. *Rev Environ Sci Biotechnol* **2010**, *9* (4), 323–330. https://doi.org/10.1007/s11157-010-9216-5.
(38) Ge, J.; Zhang, Y.; Heo, Y.-J.; Park, S.-J. Advanced Design and Synthesis of Composite Photocatalysts for the Remediation of Wastewater: A Review. *Catalysts* **2019**, *9* (2), 122. https://doi.org/10.3390/catal9020122.

(39) Ameta, R.; Benjamin, S.; Ameta, A.; Ameta, S. C. Photocatalytic Degradation of Organic Pollutants: A Review. *MSF* **2012**, *734*, 247–272. https://doi.org/10.4028/www.scientific.net/MSF.734.247.
(40) Tan, H. L.; Abdi, F. F.; Ng, Y. H. Heterogeneous Photocatalysts: An Overview of Classic and Modern Approaches for Optical, Electronic, and Charge Dynamics Evaluation. *Chem. Soc. Rev.* **2019**, *48* (5), 1255–1271. https://doi.org/10.1039/C8CS00882E.
(41) Ibhadon, A.; Fitzpatrick, P. Heterogeneous Photocatalysis: Recent Advances and Applications. *Catalysts* **2013**, *3* (1), 189–218. https://doi.org/10.3390/catal3010189.
(42) Chan, S. H. S.; Yeong Wu, T.; Juan, J. C.; Teh, C. Y. Recent Developments of Metal Oxide Semiconductors as Photocatalysts in Advanced Oxidation Processes (AOPs) for Treatment of Dye Waste-Water. *J. Chem. Technol. Biotechnol.* **2011**, *86* (9), 1130–1158. https://doi.org/10.1002/jctb.2636.
(43) Fitzmaurice, D. Using Spectroscopy to Probe the Band Energetics of Transparent Nanocrystalline Semiconductor Films. *Solar Energy Materials and Solar Cells* **1994**, *32* (3), 289–305. https://doi.org/10.1016/0927-0248(94)90265-8.
(44) Kamat, P. V. Photophysical, Photochemical and Photocatalytic Aspects of Metal Nanoparticles. *J. Phys. Chem. B* **2002**, *106* (32), 7729–7744. https://doi.org/10.1021/jp0209289.
(45) Nosaka, Y.; Nosaka, A. *Introduction to Photocatalysis: From Basic Science to Applications*; The Royal Society of Chemistry, 2016.
(46) Nosaka, Y.; Nosaka, A. Y. Generation and Detection of Reactive Oxygen Species in Photocatalysis. *Chem. Rev.* **2017**, *117* (17), 11302–11336. https://doi.org/10.1021/acs.chemrev.7b00161.
(47) Roco, M. Nanoparticles and Nanotechnology Research. *Journal of Nanoparticle Research* **1999**, *1* (1), 1–6. http://dx.doi.org/10.1023/A:1010093308079.
(48) Ngô, C.; Van de Voorde, M. H. Nanomaterials: Doing More with Less. In *Nanotechnology in a Nutshell*; Atlantis Press: Paris, 2014; pp 55–70. https://doi.org/10.2991/978-94-6239-012-6_4.
(49) Ghasemzadeh, G.; Momenpour, M.; Omidi, F.; Hosseini, M. R.; Ahani, M.; Barzegari, A. Applications of Nanomaterials in Water Treatment and Environmental Remediation. *Front. Environ. Sci. Eng.* **2014**, *8* (4), 471–482. https://doi.org/10.1007/s11783-014-0654-0.
(50) Taghipour, S.; Hosseini, S. M.; Ataie-Ashtiani, B. Engineering Nanomaterials for Water and Wastewater Treatment: Review of Classifications, Properties and Applications. *New J. Chem.* **2019**, *43* (21), 7902–7927. https://doi.org/10.1039/C9NJ00157C.
(51) Al-Hamdi, A. M.; Rinner, U.; Sillanpää, M. Tin Dioxide as a Photocatalyst for Water Treatment: A Review. *Process Safety and Environmental Protection* **2017**, *107*, 190–205. https://doi.org/10.1016/j.psep.2017.01.022.
(52) Kim, T. W.; Kwak, J. K.; Park, K. H.; Yun, D. Y.; Lee, D. U.; Son, D. I.; Han, J. H.; Lee, J. Y. Microstrucural and Optical Properties of SnO2 Nanoparticles

Formed by Using a Solvothermal Synthesis Method. *Journal of the Korean Physical Society* **2010**, *57* (6(1)), 1803–1806. https://doi.org/10.3938/jkps.57.1803.
(53) Gopidas, K. R.; Bohorquez, Maria.; Kamat, P. V. Photophysical and Photochemical Aspects of Coupled Semiconductors: Charge-Transfer Processes in Colloidal Cadmium Sulfide-Titania and Cadmium Sulfide-Silver(I) Iodide Systems. *J. Phys. Chem.* **1990**, *94* (16), 6435–6440. https://doi.org/10.1021/j100379a051.
(54) Dimitrov, M.; Guncheva, M.; Zhiryakova, D.; Lazarova, Tz.; Lalev, G.; Tsoncheva, T. Nanostructured Tin Dioxide – a Promising Multipurpose Support Material for Catalytic and Biocatalytic Applications. *Chemical Engineering Journal* **2014**, *252*, 55–63. https://doi.org/10.1016/j.cej.2014.04.052.
(55) Ma, C. M.; Hong, G. B.; Lee, S. C. Facile Synthesis of Tin Dioxide Nanoparticles for Photocatalytic Degradation of Congo Red Dye in Aqueous Solution. *Catalysts* **2020**, *10* (7), 792. https://doi.org/10.3390/catal10070792.
(56) Guan, X.; Wang, Y.; Luo, P.; Yu, Y.; Chen, D.; Li, X. Incorporating N Atoms into SnO2 Nanostructure as an Approach to Enhance Gas Sensing Property for Acetone. *Nanomaterials* **2019**, *9* (3), 445. https://doi.org/10.3390/nano9030445.
(57) Caputo, G.; Scarpellini, A.; Palazon, F.; Athanassiou, A.; Fragouli, D. One-Pot Hybrid SnO2 /Poly(Methyl Methacrylate) Nanocomposite Formation through Pulsed Laser Irradiation. *ChemPhysChem* **2017**, *18* (12), 1635–1641. https://doi.org/10.1002/cphc.201700132.
(58) Ayeshamariam, A.; Ramalingam, S.; Bououdina, M.; Jayachandran, M. Preparation and Characterizations of SnO2 Nanopowder and Spectroscopic (FT-IR, FT-Raman, UV–Visible and NMR) Analysis Using HF and DFT Calculations. *Spectrochimica Acta Part A: Molecular and Biomolecular Spectroscopy* **2014**, *118*, 1135–1143. https://doi.org/10.1016/j.saa.2013.09.030.
(59) Wang, J.; Li, H.; Meng, S.; Ye, X.; Fu, X.; Chen, S. Controlled Synthesis of Sn-Based Oxides via a Hydrothermal Method and Their Visible Light Photocatalytic Performances. *RSC Advances* **2017**, *7* (43), 27024–27032. https://doi.org/10.1039/C7RA04041E.
(60) Wang, Y.; Lee, J. Y.; Zeng, H. C. Polycrystalline SnO2Nanotubes Prepared via Infiltration Casting of Nanocrystallites and Their Electrochemical Application. *Chemistry of Materials* **2005**, *17* (15), 3899–3903. https://doi.org/10.1021/cm050724f.
(61) Adamopoulos, O.; Kungl. Tekniska högskolan; Institutionen för materialvetenskap. A Study on Nanosized Cerium Oxides Systems for Environmental Catalysis, Stockholm, 2003.
(62) Bellardita, M.; Fiorenza, R.; Palmisano, L.; Scirè, S. Photocatalytic and Photothermocatalytic Applications of Cerium Oxide-Based Materials. In *Cerium Oxide (CeO_2): Synthesis, Properties and Applications*; Elsevier: Amsterdam, The Netherlands, 2020; pp 109–167. https://doi.org/10.1016/B978-0-12-815661-2.00004-9.
(63) Hu, Q.; Huang, B.; Li, Y.; Zhang, S.; Zhang, Y.; Hua, X.; Liu, G.; Li, B.; Zhou, J.; Xie, E.; Zhang, Z. Methanol Gas Detection of Electrospun CeO2 Nanofibers by

Regulating Ce3+/ Ce4+ Mole Ratio via Pd Doping. *Sensors and Actuators B: Chemical* **2020**, *307*, 127638. https://doi.org/10.1016/j.snb.2019.127638.
(64) Khan, M. E.; Khan, M. M.; Cho, M. H. Ce3+-Ion, Surface Oxygen Vacancy, and Visible Light-Induced Photocatalytic Dye Degradation and Photocapacitive Performance of CeO2-Graphene Nanostructures. *Sci Rep* **2017**, *7* (1), 5928. https://doi.org/10.1038/s41598-017-06139-6.
(65) Xu, C.; Qu, X. Cerium Oxide Nanoparticle: A Remarkably Versatile Rare Earth Nanomaterial for Biological Applications. *NPG Asia Mater* **2014**, *6* (3), e90–e90. https://doi.org/10.1038/am.2013.88.
(66) Cui, Q.; Dong, X.; Wang, J.; Li, M. Direct Fabrication of Cerium Oxide Hollow Nanofibers by Electrospinning. *Journal of Rare Earths* **2008**, *26* (5), 664–669. https://doi.org/10.1016/S1002-0721(08)60158-1.
(67) Melchionna, M.; Trovarelli, A.; Fornasiero, P. Synthesis and Properties of Cerium Oxide-Based Materials. In *Cerium Oxide (CeO_2): Synthesis, Properties and Applications*; Elsevier, 2020; pp 13–43. https://doi.org/10.1016/B978-0-12-815661-2.00002-5.
(68) Banerjee, R.; Jayakrishnan, R.; Banerjee, R.; Ayyub, P. Effect of the Size-Induced Structural Transformation on the Band Gap in CdS Nanoparticles. *J. Phys.: Condens. Matter* **2000**, *12* (50), 10647–10654. https://doi.org/10.1088/0953-8984/12/50/325.
(69) Pandey, G.; Dixit, S. Growth Mechanism and Optical Properties Determination of CdS Nanostructures. *J. Phys. Chem. C* **2011**, *115* (36), 17633–17642. https://doi.org/10.1021/jp2015897.
(70) Harris, C.; Kamat, P. V. Photocatalytic Events of CdSe Quantum Dots in Confined Media. Electrodic Behavior of Coupled Platinum Nanoparticles. *ACS Nano* **2010**, *4* (12), 7321–7330. https://doi.org/10.1021/nn102564x.
(71) Wang, P.; Huang, B.; Dai, Y.; Whangbo, M.-H. Plasmonic Photocatalysts: Harvesting Visible Light with Noble Metal Nanoparticles. *Phys. Chem. Chem. Phys.* **2012**, *14* (28), 9813. https://doi.org/10.1039/c2cp40823f.
(72) Chakraborty, I.; Pradeep, T. Atomically Precise Clusters of Noble Metals: Emerging Link between Atoms and Nanoparticles. *Chem. Rev.* **2017**, *117* (12), 8208–8271. https://doi.org/10.1021/acs.chemrev.6b00769.
(73) Lin, Y.; Cao, Y.; Yao, Q.; Chai, O. J. H.; Xie, J. Engineering Noble Metal Nanomaterials for Pollutant Decomposition. *Ind. Eng. Chem. Res.* **2020**, *59* (47), 20561–20581. https://doi.org/10.1021/acs.iecr.0c04258.
(74) Yang, T.-H.; Ahn, J.; Shi, S.; Wang, P.; Gao, R.; Qin, D. Noble-Metal Nanoframes and Their Catalytic Applications. *Chem. Rev.* **2021**, *121* (2), 796–833. https://doi.org/10.1021/acs.chemrev.0c00940.
(75) Zhu, C.; Du, D.; Eychmüller, A.; Lin, Y. Engineering Ordered and Nonordered Porous Noble Metal Nanostructures: Synthesis, Assembly, and Their Applications in Electrochemistry. *Chem. Rev.* **2015**, *115* (16), 8896–8943. https://doi.org/10.1021/acs.chemrev.5b00255.

(76) Melinte, V.; Stroea, L.; Chibac-Scutaru, A. L. Polymer Nanocomposites for Photocatalytic Applications. *Catalysts* **2019**, *9* (12), 986. https://doi.org/10.3390/catal9120986.
(77) Tanahashi, M. Development of Fabrication Methods of Filler/Polymer Nanocomposites: With Focus on Simple Melt-Compounding-Based Approach without Surface Modification of Nanofillers. **2010**, 27.
(78) Mark, J. E. Some Novel Polymeric Nanocomposites. *Acc. Chem. Res.* **2006**, *39* (12), 881–888. https://doi.org/10.1021/ar040062k.
(79) Vaia, R. A.; Maguire, J. F. Polymer Nanocomposites with Prescribed Morphology: Going beyond Nanoparticle-Filled Polymers. *Chem. Mater.* **2007**, *19* (11), 2736–2751. https://doi.org/10.1021/cm062693+.
(80) Gangopadhyay, R.; De, A. Conducting Polymer Nanocomposites: A Brief Overview. *Chem. Mater.* **2000**, *12* (3), 608–622. https://doi.org/10.1021/cm990537f.
(81) Morselli, D.; Valentini, P.; Perotto, G.; Scarpellini, A.; Pompa, P. P.; Athanassiou, A.; Fragouli, D. Thermally-Induced in Situ Growth of ZnO Nanoparticles in Polymeric Fibrous Membranes. *Composites Science and Technology* **2017**, *149*, 11–19.
(82) Morselli, D.; Campagnolo, L.; Prato, M.; Papadopoulou, E. L.; Scarpellini, A.; Athanassiou, A.; Fragouli, D. Ceria/Gold Nanoparticles in Situ Synthesized on Polymeric Membranes with Enhanced Photocatalytic and Radical Scavenging Activity. *ACS Applied Nano Materials* **2018**, *1* (10), 5601–5611. https://doi.org/10.1021/acsanm.8b01227.
(83) Campagnolo, L.; Lauciello, S.; Athanassiou, A.; Fragouli, D. Au/ZnO Hybrid Nanostructures on Electrospun Polymeric Mats for Improved Photocatalytic Degradation of Organic Pollutants. *Water* **2019**, *11* (9), 1787. https://doi.org/10.3390/w11091787.
(84) Podasca, V. E.; Buruiana, T.; Buruiana, E. C. Photocatalytic Degradation of Rhodamine B Dye by Polymeric Films Containing ZnO, Ag Nanoparticles and Polypyrrole. *Journal of Photochemistry and Photobiology A: Chemistry* **2019**, *371*, 188–195. https://doi.org/10.1016/j.jphotochem.2018.11.016.
(85) Duncan, T. V. Release of Engineered Nanomaterials from Polymer Nanocomposites: The Effect of Matrix Degradation. *ACS Appl. Mater. Interfaces* **2015**, *7* (1), 20–39. https://doi.org/10.1021/am5062757.
(86) Roa, K.; Oyarce, E.; Boulett, A.; ALSamman, M.; Oyarzún, D.; Pizarro, G. D. C.; Sánchez, J. Lignocellulose-Based Materials and Their Application in the Removal of Dyes from Water: A Review. *Sustainable Materials and Technologies* **2021**, *29*, e00320. https://doi.org/10.1016/j.susmat.2021.e00320.
(87) Ciardelli, F.; Bertoldo, M.; Bronco, S.; Passaglia, E. *Polymers from Fossil and Renewable Resources: Scientific and Technological Comparison of Plastic Properties*; Springer International Publishing: Cham, 2019. https://doi.org/10.1007/978-3-319-94434-0.
(88) Dodero, A.; Alloisio, M.; Vicini, S.; Castellano, M. Preparation of Composite Alginate-Based Electrospun Membranes Loaded with ZnO Nanoparticles.

Carbohydrate Polymers **2020**, *227*, 115371. https://doi.org/10.1016/j.carbpol.2019.115371.
(89) Pucci, A.; Donati, F.; Bernabò, M.; Ruggeri, G.; Ciardelli, F. Smart Polymer Nanomaterials for Food Packaging Traceability. **2009**, 24.
(90) Linda, T.; Muthupoongodi, S.; Sahaya Shajan, X.; Balakumar, S. Photocatalytic Degradation of Congo Red and Crystal Violet Dyes on Cellulose/ PVC/ZnO Composites under UV Light Irradiation. *Materials Today: Proceedings* **2016**, *3* (6), 2035–2041. https://doi.org/10.1016/j.matpr.2016.04.106.
(91) Chen, Y.; Xiang, Z.; Wang, D.; Kang, J.; Qi, H. Effective Photocatalytic Degradation and Physical Adsorption of Methylene Blue Using Cellulose/GO/TiO_2 Hydrogels. *RSC Adv.* **2020**, *10* (40), 23936–23943. https://doi.org/10.1039/D0RA04509H.
(92) Khan, S. A.; Khan, S. B.; Farooq, A.; Asiri, A. M. A Facile Synthesis of CuAg Nanoparticles on Highly Porous ZnO/Carbon Black-Cellulose Acetate Sheets for Nitroarene and Azo Dyes Reduction/Degradation. *International Journal of Biological Macromolecules* **2019**, *130*, 288–299. https://doi.org/10.1016/j.ijbiomac.2019.02.114.

CHAPTER 2: CELLULOSE ACETATE TIN DIOXIDE FIBROUS MEMBRANE FOR THE PHOTOCATALYTIC DEGRADATION OF ORGANIC DYES

ABSTRACT

We present a novel fibrous membrane based on Cellulose Acetate and SnO_2 NPs and its utilization for the photocatalytic degradation of MB and MO dyes. The SnO_2 directly grown on the surface of the ultrafine fibers upon mild thermal treatment condition. The developed mats are able to photodegrade both anionic and cationic dyes with an efficiency of more than 90%. The TOC results confirm that 54% and 79% of the MO and MB respectively are mineralized, while the rest are products of a demethylation process that occurred in both types of dyes as well as of a hydroxylation process in the MO azo-dye, as confirmed by the LC-MS characterization of the treated solutions. We demonstrate with this approach the possibility to form directly in the mats SnO_2 NPs, using innocuous solvents and a precursor agent with nontoxic byproducts. These kind of nanocomposites can open up the possibility to use them as efficient materials for water remediation of organic pollutants.

This Chapter is based on: Costantino, F., Armirotti, A., Carzino, R., Gavioli, L., Athanassiou, A., & Fragouli, D. (2020). In situ formation of SnO2 nanoparticles on cellulose acetate fibrous membranes for the photocatalytic degradation of organic dyes. *Journal of Photochemistry and Photobiology A: Chemistry*, *398*, 112599.[1]

2.1 Introduction

In the previous chapter, the photocatalytic properties of semiconductor NPs and their use as photocatalyst for water treatment and the necessity of their immobilization in a solid substrate, such as a polymeric matrix, for a safe and easily handle application have been explained.

In the present chapter, we present a study on the fabrication of tin dioxide (SnO_2 NPs) directly into the polymer matrix of Cellulose Acetate (CA), and we explore the possibility to be used for the photocatalytic degradation of organic dyes. CA is chosen as a host matrix due to its bio-based origin, cost effectiveness and easy manageability.[2,3] Tin dioxide NPs are chosen as photocatalysts considering that their chemical stability and structure are very similar to the TiO_2, the most common photocatalyst. Furthermore, SnO_2 has no adverse health effects and is poorly adsorbed by the human body when inhaled or injected.[4,5] However, despite the large-scale utilization of SnO_2 powders in different applications, and many reports devoted to their preparation methods, it is not frequently used for photocatalytic applications.[4] This could be attributed to the fact that following common preparation procedures like solvo-thermal and precipitation methods, the NPs usually are composed of the combination of both Sn^{4+} and Sn^{2+} states.[6] Its stannous oxide form (Sn^{2+}) is not recommended for photocatalytic processes due to the oxygen vacancies in its structure, which lead it to act as a reducing agent.[7]

However, with the present study we realize a simple, green and low-cost method based on the electrospinning technique, in order to form CA/SnO_2 polymer nanocomposites that can be effectively used for photocatalysis.

The fibrous mats are obtained by the electrospinning of a tin precursor/CA solution and the subsequent thermally induced in situ growth of SnO_2 NPs in the solid mats. With the proposed fabrication method, we obtain CA/ SnO_2 nanocomposite fibrous mats with the NPs homogenously distributed in the polymer fibers. Their ability to photodegrade anionic and cationic dyes is tested MO and MB as model dyes. We prove that the obtained material is a feasible candidate for the development of novel bio-composite fibrous photocatalysts, and given the broad applicability of the SnO_2 based materials this method can be also used for the fabrication of fibrous nanocomposites for sensing applications.

2.2 Materials and Methods

2.2.1 Chemicals

Cellulose Acetate (CA, average MW~40.000 Da), tin (II) ethyl-hexanoate (SnPrec, $C_{16}H_{30}O_4Sn$ 99.99%), Acetone (> 99.5%, GC grade), N,N-Dimethylformamide (DMF, Cromasolv Plus), Methylene Orange (MO) and Methylene Blue (MB) were purchased by Sigma Aldrich. All chemicals were used without further purification.

2.2.2 Fibers Preparation

Typically, 1.00 g of CA polymer is dissolved in 10 mL of an Acetone/DMF (volume ratio 7:3) mixture after stirring at 60°C and 400 rpm until a clear solution is obtained. Subsequently, 0.227 g of SnPrec was dissolved in 3 mL of the same solvent mixture upon stirring at 45°C and 400 rpm for 30 minutes. Then, the two above-mentioned solutions were mixed obtaining a stable solution.

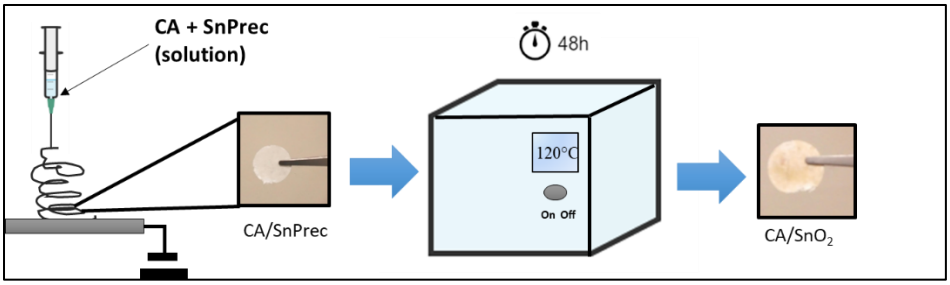

Scheme 2. Procedure for the preparation of CA/SnO_2 fiber mats, starting from the electrospinning of CA-SnPrec solution and then the thermal treatment of the fibers at 120°C for 48h. The pics are representative samples of CA/SnPrec after the electrospinning procedure, and after the thermal treatment (CA/SnO_2).

Electrospinning was performed in a closed box using a vertical geometry. In particular, the solution was placed in a 10 mL syringe and a syringe pump (NE-1000, New Era Pump Systems Inc.) was used to control the flow rate, while a blunt 19-gauge needle was used as spinneret. The needle was connected to a positive electrode of a high voltage power supply, while the aluminum collector was grounded. The spinning voltage, the nozzle-collector distance and the injection flow rate were 22kV, 15 cm and 0.3 mL/h respectively. The obtained fiber mats (CA/SnPrec) were dried under vacuum for 10 hours in order to remove any solvent residue. Then, to promote the nucleation and growth of SnO_2 NPs, the fibrous mats were placed in an oven at 120°C for 48 hours in air (see Scheme 2). Considering a total conversion of the precursor salt in metal oxide, the expected content is approximately ~10% wt. for SnO_2 with respect to the polymer.

2.3 Photodegradation experiment

The photocatalytic activity of the porous nanocomposites was studied by monitoring the degradation of MO and MB. For each experiment, 3 mL of the dye (5 ppm of MO and 5 ppm for MB) aqueous solution were placed in a quartz cuvette containing 0.004 g of the

CA/SnO_2 fibrous mat suspended in it. The experiments were carried out in a closed box, equipped with UV-lamp (AnalytikJena UVP UVGL-58, 6 Watt, 0.16 Amps, λ= 254 nm). Before starting the irradiation, the electrospun nanocomposite mats were kept in the dyes solutions in the dark, to reach the adsorption/desorption equilibrium of the dyes on the surface of the samples. The cuvettes were then placed in a fixed position at a distance of 6 cm under the UV lamp. The concentration of dyes was determined by a calibration curve of each dye, using a Varian Cary 6000i UV-Vis-NIR spectrophotometer and MilliQ water as a reference. In both cases, the calibration curve is acquired by recording the absorbance of solutions with known dyes concentrations (from 5 to 0.1 ppm) (for further details see Appendix C and related Figure C1). The photodegradation tests were performed by recording the decrease of the characteristic absorption peak (664 nm for MB and 465 nm for MO) for both dyes at the corresponding λ_{max} every 30 minutes.

The % degradation of the dyes was calculated using the following equation:

$$(\%) = \frac{C_0 - C(t)}{C_0} \times 100\% \qquad (2.1)$$

Where C_0 is the standard concentration of each dye before irradiation and C(t) is the concentration of the dye solutions at time t during the photocatalytic process.

The same experiment was performed in the dark in order to confirm that the observed behavior is attributed solely to the photocatalytic degradation of the dye and not to adsorption processes. Furthermore, to assure that the photodegradation of the dyes is attributed to the mats and not to their self-degradation, the same irradiation experiments were performed to the dyes solutions in the absence of the mats.

2.3.1 Analysis of photodegraded products

All liquid samples, before and after the photocatalytic process, were analyzed by a high-resolution liquid chromatography-mass spectroscopy (LC-MS) using a Synapt G2 quadrupole-time of flight system coupled with an Acquity UPLC chromatographic system equipped with a HSS T3 (2.1 x 100 mm^2, 1.8 µm particle size) reversed phase column. The column and UPLC-MS system were purchased from Waters Inc. Milford, USA. The flow rate was set at 0.5 ml/min. Eluents were A = water and B = acetonitrile, both added with 0.1% formic acid. The samples were diluted three fold in eluent A and transferred to LC-MS vials. 4 µl of samples were loaded on the system and separated with a linear gradient of eluent B in A (3% to 100% B in 8 minutes). Mass spectra were recorded in electrospray positive and negative modes over the range of 50 to 600 m/z mass to charge ratio. The identification of the degradation products was performed based on their measured accurate mass (maximum allowed tolerance 5 ppm) and isotopic profile compared to the calculated one.

MembrPure uniTOC analyzer is used to measure the total organic carbon (TOC) before and after the photocatalytic process in all liquid samples. Before the analysis the liquid samples were filtered with a PTFE membrane with 0.2 µm pore size, 1 mL of each dye was diluted with 20mL of milliQ H_2O.

Considering the mineralization process, the % of efficiency is calculated as follow:

$$mineralization\ (\%) = \frac{[TOC]_i - [TOC]_f}{[TOC]_i} \cdot 100 \qquad (2.2)$$

Where TOC_i ($mg \cdot L^{-1}$) and TOC_f ($mg \cdot L^{-1}$) are the TOC concentrations in solution before and after the photodegradation process.

2.4 Results and Discussion

2.4.1 Morphological Characterization of the CA/SnO_2

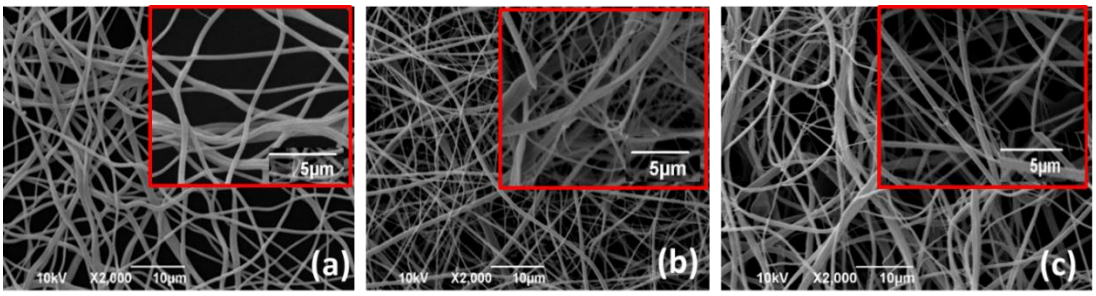

Figure 2. FE-SEM morphology of the fibrous mats. (a) CA, (b) CA/SnPrec and (c) CA/SnO_2. (Inset) high magnification of (c).

The morphology of the fibrous mats is investigated by SEM analysis (the details of the experimental procedure is in the Appendix A) and as shown in Figure 2, the structure of the CA fibers does not significantly change after the addition of the SnPrec and after the thermal treatment.

In all cases, the mats are composed of randomly distributed fibers with defect free well-defined morphology and smooth surface. The mean diameter of the CA fibers is 1.2±0.4 μm, slightly greater than the diameter of the CA/SnPrec and CA/SnO_2 (1.0±0.4 μm and 1.1±0.4 μm), possibly attributed to the eventual small change of the viscosity of the solution containing the SnPrec. Most importantly, the thermal treatment of the CA/SnPrec mat does not affect the morphology of the polymer fibers, as their size before and after the thermal treatment is similar, as can be seen in the Figure 2.

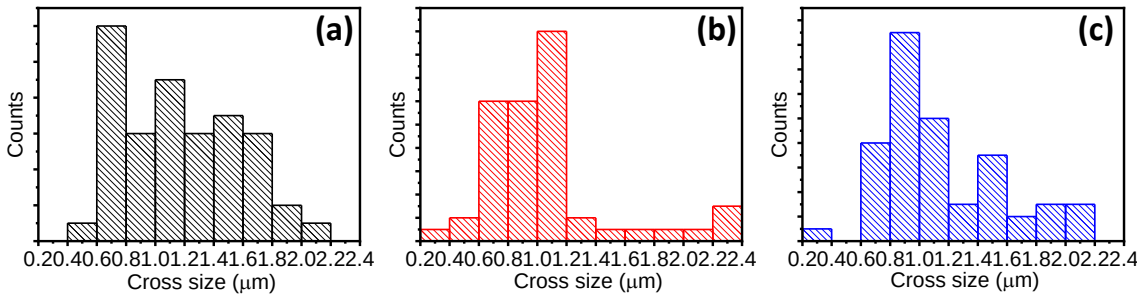

Figure 2.1. Size distribution of fibers (a) CA. (b) CA/SnPrec and (c) CA/SnO_2.

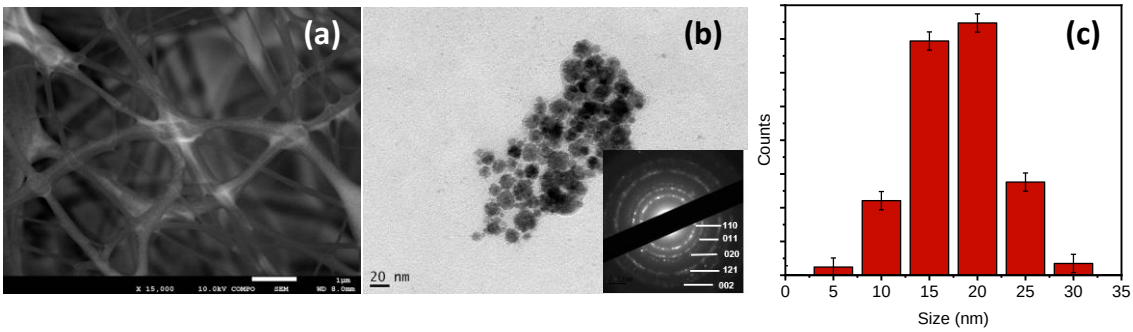

Figure 2.2 (a) HR-SEM, (b) TEM image of the SnO_2 NPs. (Inset) The SAED pattern of (b) and (c) size distribution of the SnO_2 NPs.

A closer look to the CA/SnO_2 fibers by HR-SEM (Figure 2.2 (a)) reveals the presence of bright features on the surface of the polymer fibers attributed to the presence of SnO_2 NPs but their size is small and therefore difficult to be detected with the specific imaging method. Therefore, in order to identify the SnO_2 NPs, the TEM analysis in the dissolved CA/SnO_2 fibers was carried out. As can be seen in Figure 2.2 (b), the presence of spherical NPs is evident with an average diameter of 16.3 ±3.5 nm as can be seen in the Figure 2.2 (c). The corresponding selected-area electron diffraction (SAED) pattern (inset in the Figure 2.2 (b)), presents spotty ring patterns without any additional diffraction spots and

rings of second phases, and is characteristic of the presence of highly crystalline SnO_2 NPs.[8,9]

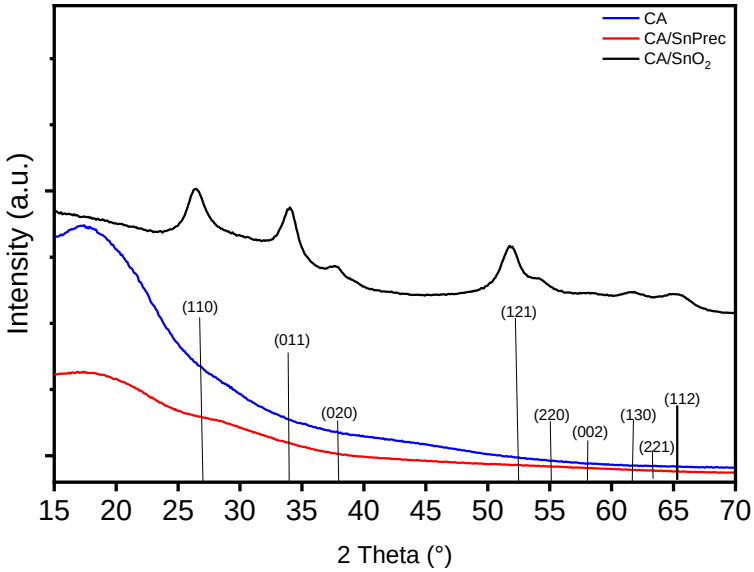

Figure 2.3. XRD pattern of prepared fibers: CA (blue line), CA/SnPrec (red line) and CA/SnO_2 (black line), the vertical lines correspond to the JCPDS card No. 96-100-0063.

The XRD analysis of the CA/SnO_2 mats confirms the presence of crystalline SnO_2 NPs after the thermal treatment of the CA/SnPrec as presented in Figure 2.3. Specifically, before the thermal treatment, the CA/SnPrec sample is amorphous as the CA neat polymer. However, after the thermal treatment of the sample the diffraction peaks emerge indicating the crystalline form of the sample. The analysis of the peaks reveals that they are representative of the *Casserite* structure of SnO_2 with typical peaks centered in the positions (110), (011), (020), (121), (220), (130), (221) and (112) [JCPDS card No. 96-100-0063].[10] The crystalline domain is calculated using the Scherrer's equation (see equation B.1 Appendix B for the details); the analysis of the characteristic peak centered at 26.58° (110), and it is revealed that the crystalline size is 12.8 nm, similar with the NPs

size obtained by the TEM analysis. In addition, the lattice parameter detected with the XRD matched well with the SAED pattern, and this confirms the high crystallinity and pure phase of SnO_2 NPs in the fibrous mats.

The successful conversion of the SnPrec to SnO_2 crystalline NPs after the thermal treatment of the CA/SnPrec fibers is confirmed by the FTIR-ATR analysis as reported in Figure 2.4. In all spectra presented, are apparent the typical peaks of the CA polymer: the stretching mode of carbonyl groups centered at 1740 cm^{-1}, the $–CH_3$ groups of the acetyl moiety located at 1215 cm^{-1} and 1368 cm^{-1}, the $-CH_2$ vibration at 1431 cm^{-1}, the typical stretching of -C-O-C- bridge centered at 1040 cm^{-1} and the peak centered at 900 cm^{-1} representative of the saccharide structure.[11]

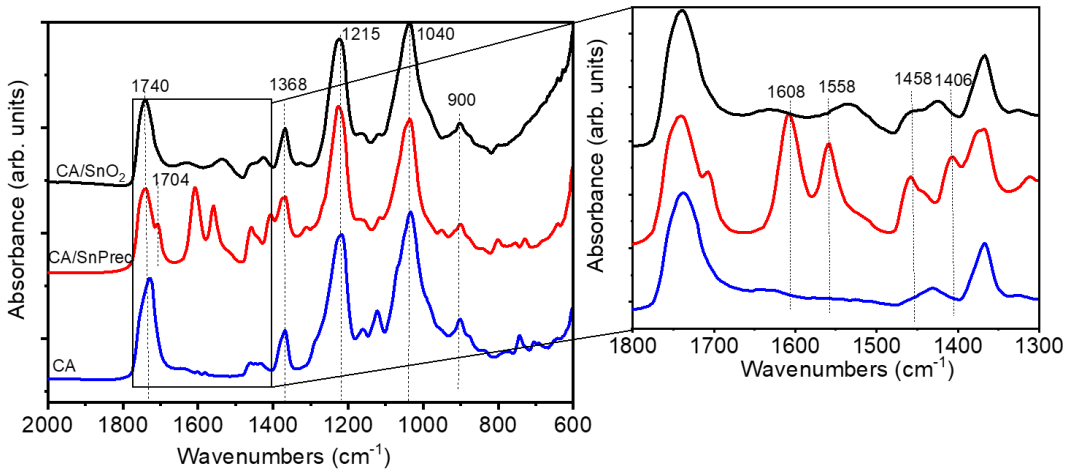

Figure 2.4. FTIR spectra of neat CA (blue line), CA/SnPrec (red line) and CA/SnO_2 (black line). (Inset) FTIR spectra of all prepared samples in the region (1800-1300 cm-^{1}.

However, in the CA/SnPrec sample are also present the peaks of ethyl hexanoate.[12] In particular, can be observed a small peak at 1704 cm^{-1} corresponding to an asymmetrical –COO stretching, typical for a coordinated 2-ethylhexanoate acid ligand with tin.[12,13] Most

importantly, two main peaks centered at 1608 cm^{-1} and 1554 cm^{-1} referred to the asymmetrical stretching of the carboxylate group $\nu_{as}(COO^-)$, and other two absorption bands centered at 1458 cm^{-1} and 1406 cm^{-1} (see Inset Figure 2.4) attributed to the symmetrical stretches $\nu_s(COO^-)$, are typical of the coordination of the carboxylic groups to a metal ion.[12] The $\nu_{as}(COO^-)$ and $\nu_s(COO^-)$ bands are split into different components indicating different coordination modes with the Sn metal ion. The frequency difference between the asymmetrical and symmetrical stretches ($\Delta\nu=\nu_{as}(COO^-)-\nu_s(COO^-)$) is used to determine the coordination type of the carboxylates with the metal.[14] The difference between the ν_{as}, located at 1558 cm^{-1} and the ν_s located at 1406 cm^{-1} is $\Delta\nu$ 152 cm^{-1} and reveals the bridging coordination of the ligands with the metal ion (140 $cm^{-1} < \Delta\nu < 200$ cm^{-1}). Also, the difference between the band located at 1558 cm^{-1} and the ν_s at 1458 cm^{-1} is 100 cm^{-1} representative of the bidentate coordination.[12] The peak at 1608 cm^{-1} may be the result of band splitting (a doublet at 1608 and 1554 cm^{-1}) due to the presence of the two coordination modes (bidentate and bridging). After the thermal treatment, and therefore in the spectrum obtained using the CA/SnO_2 sample, the intensity of all peaks representative of the Sn precursor decreases significantly proving that the thermal treatment results in the precursor's efficient decomposition. On the top a single $\nu_s(COO^-)$ band is present at 1458 cm^{-1} (see Inset Figure 2.4), while the $\nu_{as}(COO^-)$ is evident at 1535 cm^{-1} with a difference $\Delta\nu$ of 83 cm^{-1}, indicating that the metal ions are coordinated with the carboxylate groups of the composite with the bidentate mode.[15]

XPS analysis is performed in order to elucidate the oxidation state of the Sn in the CA/SnO_2 sample. The O1s high-resolution spectrum of the CA in the Figure 2.5 (a) showed the

typical behavior related to the –C-O- and –C-O-H- located at 531.83 eV and 532.90eV, respectively.[16] While the XPS spectra of CA/SnO_2 (Figure 2.5 (b)) indicates the presence of different oxygen species representative of the CA polymer and the Sn based nanoparticles. In particular, the bands correspond to -C-O- and –C-O-H- respectively and match well with the ones referred to the pure CA polymer. The peak centered at 530.7 eV can be assigned at to the O-Sn^{4+} bonds in the SnO_2 lattice, indicating that the oxidation state of Sn is +4.[16,17] This is confirmed by studying the Sn 3 d high-resolution spectrum. As shown in Figure 2.5 (c), the two peaks centered at 495.3eV and 486.9eV correspond to Sn $3d_{(3/2)}$ and $3d_{(5/2)}$ respectively, with the Sn oxidation state +4.[7] Finally, the valence band (VB) spectrum corresponds at the core level structures of Sn 5s (Figure 2.5 (d)). According to the literature, a dominant peak at E_B ~ 5.2 eV is an O 2p- derived structure, which is characteristic for the SnO_2.[18]

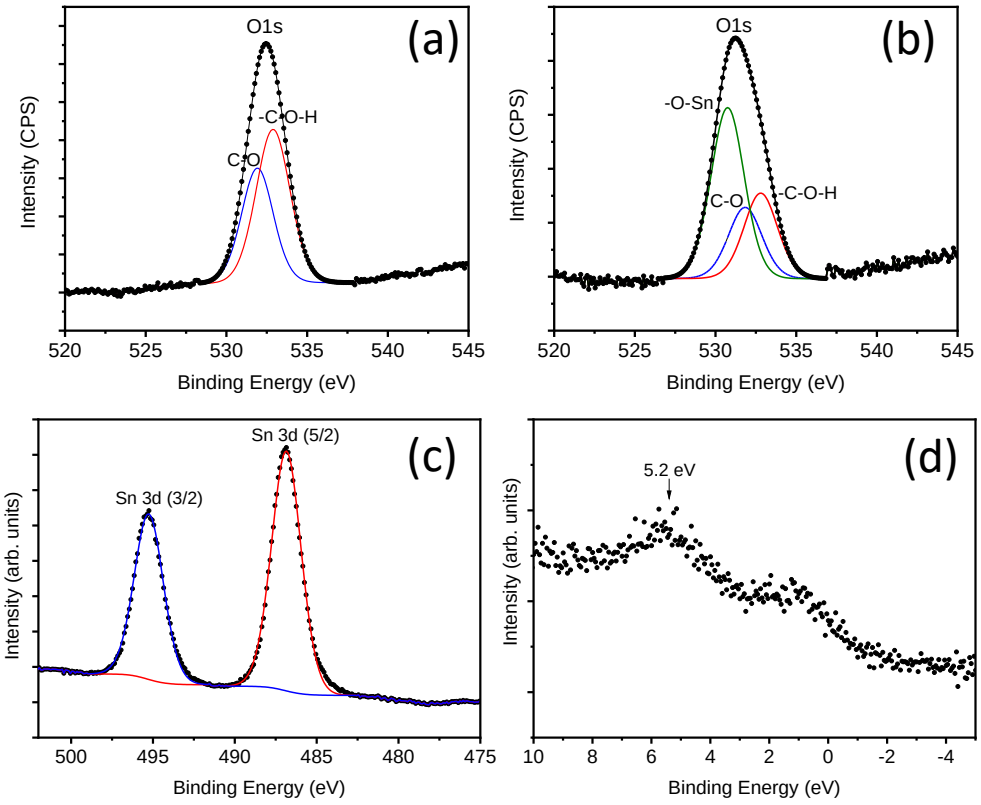

Figure 2.5. (a) XPS core level of O1s of CA, (b) O1s of CA/SnO_2, (c) Sn 3d of CA/SnO_2 and (d) valence band spectra of CA/SnO_2.

As proved so far, with this innovative route it is possible to prepare SnO_2 NPs based nanocomposite fibrous mats starting from CA polymer fibers filled with the SnPrec. The thermal annealing process of the CA/SnPrec mats at a relatively low temperature (120°C), induces the decomposition of the precursor and its transformation into crystalline SnO_2 NPs without the need of the presence of any solvent or oxidative agent. In fact, as shown in the following reaction, it can be expected that upon the thermal treatment of the solid porous system, the 2-ethylhexanoate ligand is released, with the subsequent nucleation of

Sn^{4+} species and the growth of SnO_2 NPs, and the consequently release of organic heptene, heptane and CO_2 .

$$[CH_3(CH_2)_3CH(C_2H_5)CO_2]_2Sn \rightarrow SnO_2 + 6CO_2 + 3CH_3(CH_2)_5CH_3 + 3CH_3CH = CH(CH_2)3CH_3.$$

2.5 Photocatalytic degradation of MO and MB

The band-gap energy of the SnO_2 NPs present at the CA fibers is evaluated by diffused reflectance spectroscopy and the Kubelka-Munk approximation (See Appendix B for more details of the calculation). The calculated energy band gap of the formed NPs is 3.26 ± 0.16 eV in accordance with the semiconductor nature of the SnO_2 NPs reported in other studies, as can be seen in the Figure 2.6 (b).[4]

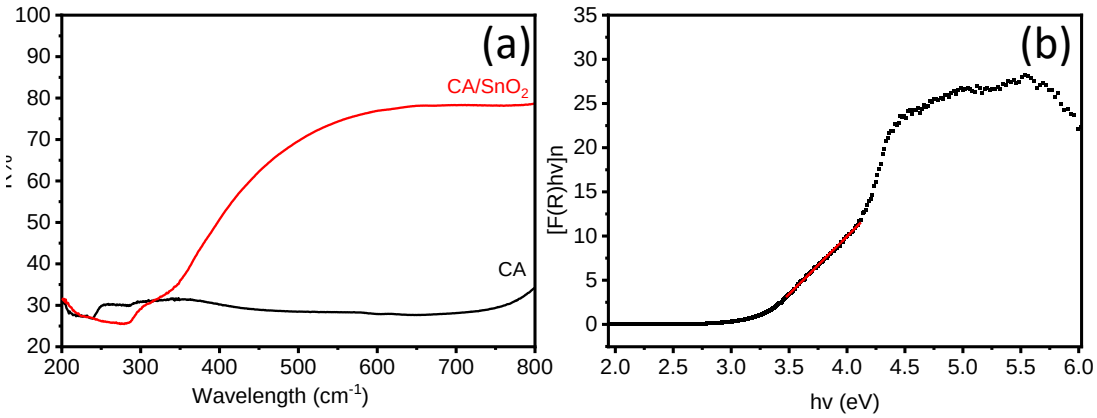

Figure 2.6. Diffuse reflectance spectra of CA and CA/SnO_2 (a) and Kubelka-Munk plot of CA/SnO_2 (b) (R^2=0.99).

As it can be seen from Figure 2.6 (a), CA/SnO_2 absorbs light stronger than neat CA, increases absorption under UV to complete 80% as well as under visible range. It is possible to observe the characteristic absorption of SnO_2 NPs in the UV region originated

by the direct band transition. The wettability property of the membrane is studied as well, to understand the role of the polymer matrix during the photocatalytic process see Figure 2.7.

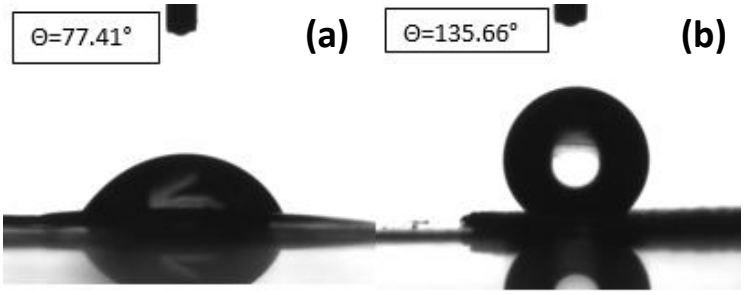

Figure 2.7. Water contact angle of (a) neat CA (a) and (b) CA/SnO_2.

The contact angle of neat CA is 77.4°±7.5°, confirming the hydrophilic nature of the polymer matrix; while the CA/SnO_2 mats are hydrophobic (water contact angle of 135.6° ±6.2°). The increase in the hydrophobicity proves for once more the presence of a rough surface and of a different surface chemistry at the fibers due to the NPs formed in situ on their surface.[19]

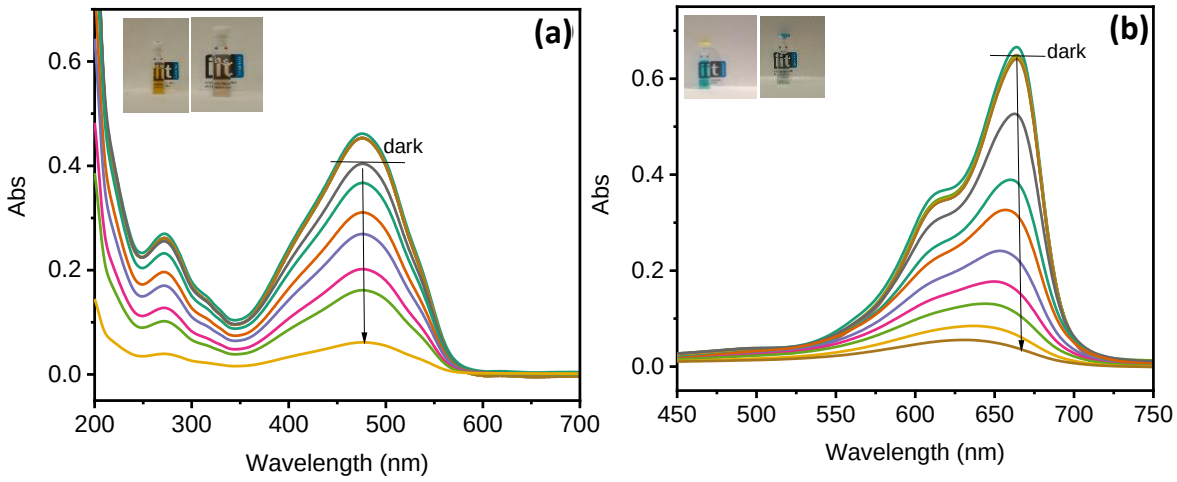

Figure 2.8. Absorbance spectra of MO and MB in presence of CA/SnO_2, in both cases the system reached the equilibrium in the dark for 180 minutes, then the experiment was performed under UV irradiation for 210 for MO and 240 min for MB. The Inset represent the dye solution before and after the photocatalytic process.

The CA/SnO_2 mats were left in contact with both dyes under dark for 180 min in order to reach the equilibrium and then they are subjected to UV light irradiation in order to explore their photocatalytic properties. As shown in Figure 2.8 (a), and in Figure 2.8 (b), the UV light causes the decrease of the intensity of the main peaks of the MO and MB dyes, centered at 464 nm and 664 nm respectively, over time, while both solutions become colorless in the end of the process, as can be seen in the inset of the Figure 2.8.

After 210 min and 240 min of irradiation, the concentration of MO and MB is 92% and 95% (see Appendix B for the details) lower than the initial one respectively, indicating that the SnO_2 NPs formed in situ on the CA fibers exhibit a good photocatalytic activity under

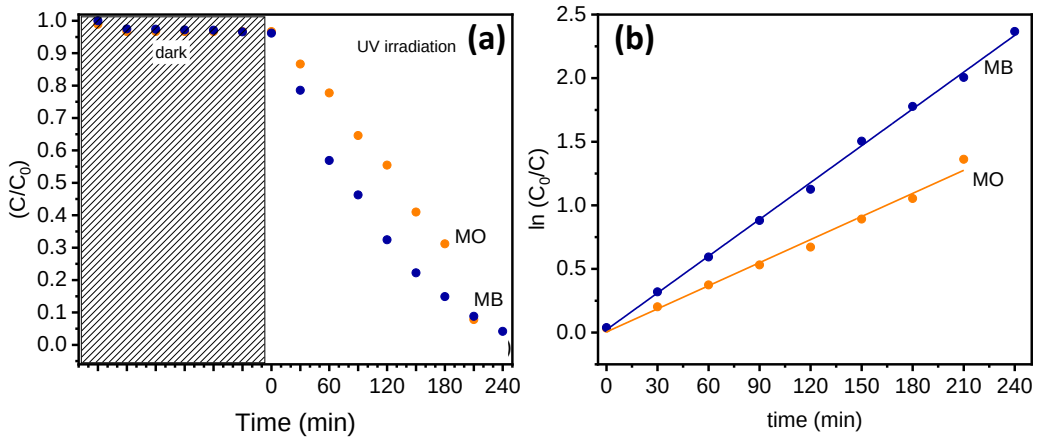

Figure 2.9. (a) Concentration degradation profiles of MO and MB versus time, (b) linear fit of log (C_0/C) vs time of CA/SnO2 in presence of MO and MB.

UV light irradiation. In fact, this is solely attributed to the NPs since preliminary experiments confirm that the CA substrates had no influence on the photocatalytic reaction. The ln(C_0/C) has a linear dependence with irradiation time confirming the pseudo first-order decay, and based on this, the degradation rate of both dyes was estimated. Starting from the absorbance and considering the Lambert Beer's law (A=ε•*l*•*C*) it is possible to estimate the concentration during the process see Figure 2.9 (a), and then it is possible calculate the rate constant of photodegradation process, See Figure 2.9 (b). The rate constant *k*, indicates how fast the reaction occurs, and can be calculated using the equation:

$$ln\frac{C_0}{C} = k \cdot t$$

The *k* for MO is 0.006 min^{-1} (R^2=0.99) and for MB 0.010 min^{-1} (R^2=0.99). Although the MB degradation rate of the bare SnO_2 nanoparticles is double, something expected due to the smaller surface area of the fibrous mats compared to the pure nanoparticles, the overall

degradation % is quite similar indicating the good potentiality of the proposed material for soft photocatalysts applications.

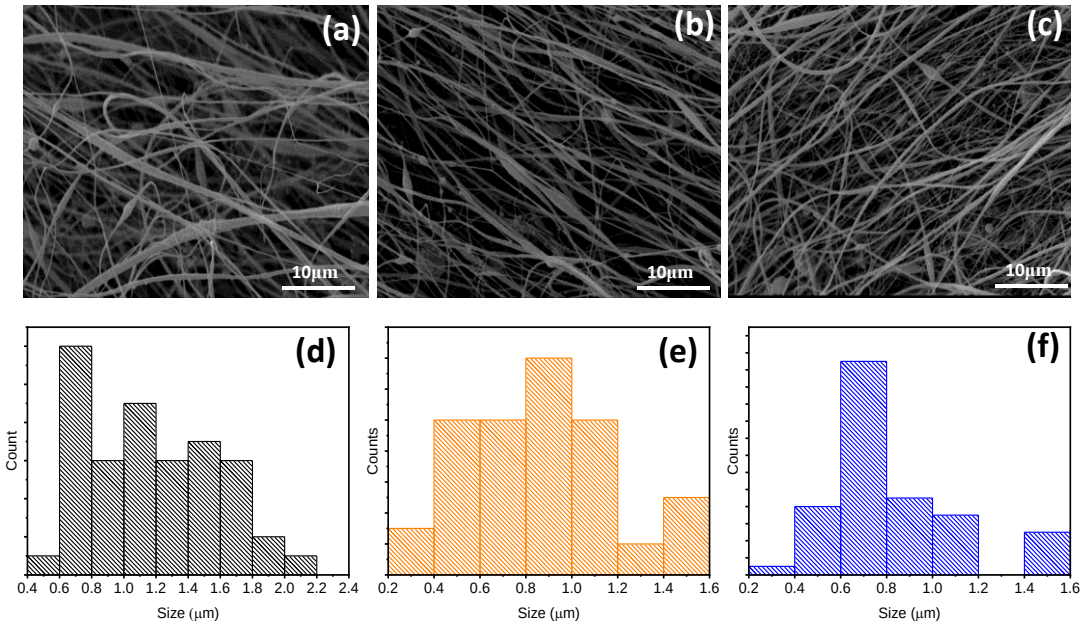

Figure 2.10. (a) SEM image of CA/SnO_2 mats before photodegradation process (PD), (b) CA/SnO_2 mats after PD of MO, (c) CA/SnO_2 mats after PD of MB. (d) Size distribution of CA/SnO_2 mats before PD process. (e) Size distribution of CA/SnO_2 after PD of MO and (f) size distribution of CA/SnO2 after PD of MB. The scale bar for all SEM images is 10µm.

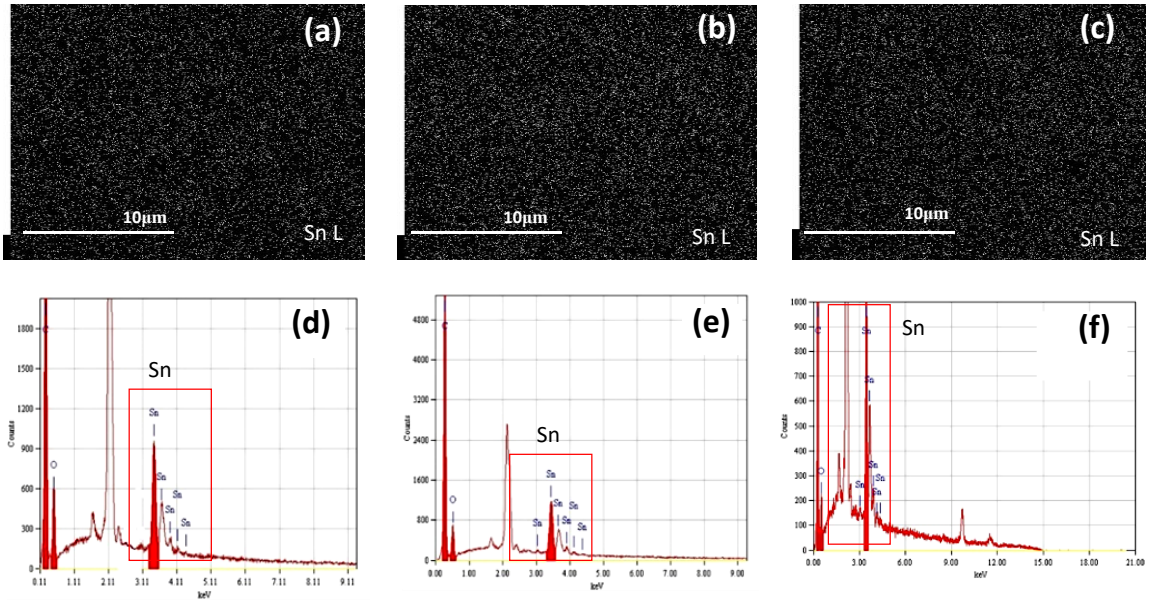

Figure 2.11. SEM- EDS mapping and quantitative analysis of (a-d) CA/SnO2 before PD process, (b-e) CA/SnO2 after PD of MO and (c-f) CA/SnO2 after PD of MB.

Table 2. Mass (%) and Atomic (%) percentage values of elemental composition of all fibrous mats.

Sample	**CA/SnO_2**			**CA/SnO_2_after_MO**			**CA/SnO_2_after_MB**		
Size of mats	0.87±0.34 µm			0.86±0.31 µm			0.82±0.27 µm		
Element	C	O	Sn	C	O	Sn	C	O	Sn
Mass (%)	28.0	19.7	52.31	34.16	18.61	47.23	35.21	19.42	45.37
Atom (%)	66.38	21.98	11.64	64.56	26.41	9.03	65.02	26.88	8.1

It should be mentioned that the photodegradation process had no effect on the mean diameter and morphology of the CA/SnO_2 fibers (see Figure 2.10) as well as on their surface chemistry (see Table 2) analyzed by EDS analysis , suggesting the stability of the fibrous mats during the photocatalytic process. In all cases the Sn element is uniformly distributed on the whole mat as the EDS analysis demonstrates, see Figure 2.11. This

suggests that the surface chemistry of the mats is not altered. In fact, the composition of all mats is similar before and after the degradation process

After the photocatalytic process, the degree of the conversion of both dyes and all of the generated intermediates into CO_2 and H_2O, ions and some mineral acids, the so-called mineralization, is determined by TOC analysis (see Appendix A for the details). For both dye solutions, the presence of the CA/SnO_2 fiber mats in combination with the UV irradiation cause the decrease of the TOC values (Table 2.1, see Appendix B for details related to the calculations). In fact, in contrary to the pure CA fibers where no difference is observed, CA/SnO_2 mats mineralized about 54% of the MO and 79% of the MB dyes. Apart the slightly higher duration of the MB photodegradation process, the observed difference may be mainly attributed to the different structure of the dyes. The MO dye has a more complex structure due to the double bond (-N=N-) and the presence of sulfonate groups (SO_3^-) making more difficult its mineralization process, that convert the only carbon species present in the molecule in CO_2.[20]

Table 2.1. TOC values of pristine dye and after the photocatalytic process in presence of CA/SnO_2, for comparison the TOC value is reported for the bare CA matrix under UV irradiation.

Sample name	**TOC (mg/L)**
MO	1.24
MO/after-210minUV	0.57
MB	1.30
MB/after-240minUV	0.27
CA-H_2O-UV	0.38

2.6 Liquid Chromatography analysis after photodegradation

The analysis of the non-mineralized photodegradation byproducts of both dyes is performed by LC-MS. As shown in the profiles of Figure 2.12 (a,b), in the end of the irradiation process the characteristic peaks of MO and MB dyes are significantly reduced suggesting that the photocatalytic process caused an appreciable degree of decomposition of both types of dyes.

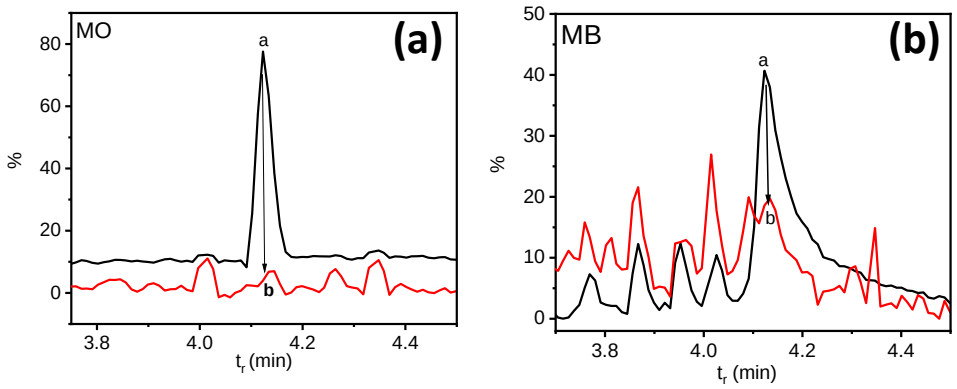

Figure 2.12. (a) LC-MS chromatograms of MO and (b) LC-MS chromatograms of MB before and after UV irradiation in presence of CA/SnO2 photocatalyst.

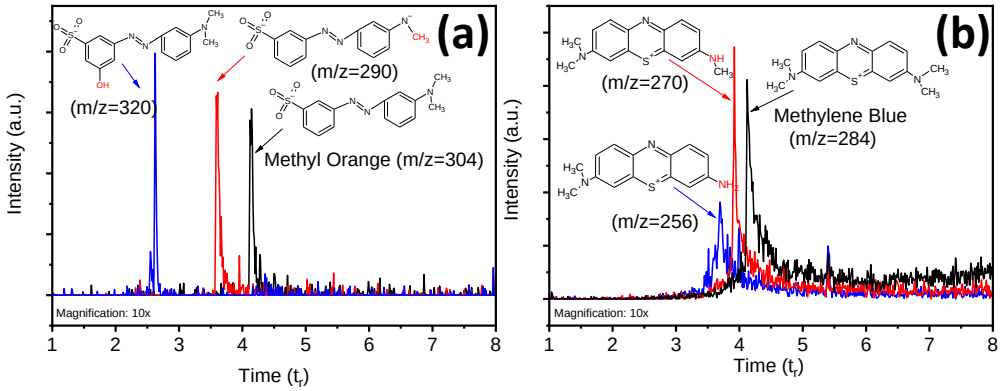

Figure 2.13. Chromatographic run of degradation products of MO, (a) chromatogram of degradation products of MB (b) in presence of CA/SnO2 after the photodegradation process.

At the same time new peaks are detected at lower retention times, corresponding to new molecules produced by the photodegradation of the pristine dyes as demonstrated in Figure 2.13 (a, b).

Concerning the MO, the signal detected in the negatively charged, deprotonated, form at 304 m/z is attributed to the dye molecule which in neutral solutions is present its benzene-sulfonic form (Figure 2.13(a)). The major degradation byproducts observed are formed by the cleavage of $–CH_3$ from the N-alkyl group linked with the benzene ring and the addition of -OH group to the benzenesulfonic ring of MO, and these two forms are detected at 290 and 320 m/z, respectively. Figure 2.13 (b) demonstrates the MB photodegradation byproducts.[21] The signal at 284 m/z is attributed to the MB, which is a conjugated benzene ring with an intense blue color in neutral solutions. During the photocatalytic process, the parent dye is degraded by a cleavage of one or more $–CH_3$ substituents on the amine groups. In fact two new products are detected at 270 m/z and 256 m/z that corresponding to Azure B and Azure A, respectively.[22]

2.7 Conclusions

This Chapter deals with the preparation of CA/SnO_2 nanocomposites focusing mainly on the degradation of MO and MB dyes in water.

Summarizing, the most relevant results of the study are:

- The proposed CA/SnO_2 fibrous mats can be fabricated by electrospinning starting from a CA/Tin (II) ethylhexanoate precursor solution, and subsequently by the thermal treatment of the formed fibers.

- The microscopy and physicochemical studies prove the presence of the *Casserite* structure of SnO_2 crystalline NPs on the fibers, with a Sn^{+4} oxidation state.

- Using these fibrous mats about 92% of the MO and 95% of the MB can be decomposed by the presence of the fibers upon UV light irradiation and the demineralization reaches 79% for the MB and 54% for MO dyes.

- The NPs are fixed stably on the fibers and the overall structure of the mat is stable after the photodegradation process.

- With the herein presented in situ process, toxic solvents and complicated preparation methods for the SnO_2 NPs as well as drawbacks coming from the direct mixture of colloidal NPs with polymers, which often compromise their surface chemistry and therefore their functionality, can be prevented. Furthermore, the presence of the CA polymer as a host matrix facilitates the handling and transportation of the photocatalysts, and eliminates additional processing steps after

the remediation process for the removal of the photocatalysts as in the case of powders.

With the present work, the use of such promising, economical and environmentally friendly process based on CA/SnO_2 could pave the way for the development of fibrous nanocomposite materials for water treatment.

2.8 References

(1) Costantino, F.; Armirotti, A.; Carzino, R.; Gavioli, L.; Athanassiou, A.; Fragouli, D. In Situ Formation of SnO2 Nanoparticles on Cellulose Acetate Fibrous Membranes for the Photocatalytic Degradation of Organic Dyes. *Journal of Photochemistry and Photobiology A: Chemistry* **2020**, *398*, 112599. https://doi.org/10.1016/j.jphotochem.2020.112599.

(2) Hon, N.-S. Photodegradation of Cellulose Acetate Fibers. *Journal of Polymer Science: Polymer Chemistry Edition* **1977**, *15* (3), 725–744. https://doi.org/10.1002/pol.1977.170150319.

(3) Bayer, I. S.; Fragouli, D.; Attanasio, A.; Sorce, B.; Bertoni, G.; Brescia, R.; Di Corato, R.; Pellegrino, T.; Kalyva, M.; Sabella, S.; Pompa, P. P.; Cingolani, R.; Athanassiou, A. Water-Repellent Cellulose Fiber Networks with Multifunctional Properties. *ACS Appl. Mater. Interfaces* **2011**, *3* (10), 4024–4031. https://doi.org/10.1021/am200891f.

(4) Al-Hamdi, A. M.; Rinner, U.; Sillanpää, M. Tin Dioxide as a Photocatalyst for Water Treatment: A Review. *Process Safety and Environmental Protection* **2017**, *107*, 190–205. https://doi.org/10.1016/j.psep.2017.01.022.

(5) Dimitrov, M.; Guncheva, M.; Zhiryakova, D.; Lazarova, Tz.; Lalev, G.; Tsoncheva, T. Nanostructured Tin Dioxide – a Promising Multipurpose Support Material for Catalytic and Biocatalytic Applications. *Chemical Engineering Journal* **2014**, *252*, 55–63. https://doi.org/10.1016/j.cej.2014.04.052.

(6) Mahana, S.; Sapkota, P.; Ghosh, S.; Manju, U.; Topwal, D. Structural and Electronic Phase Evolution of Tin Dioxide. 6.

(7) Xia, X.; Dong, X. J.; Wei, Q. F.; Cai, Y. B.; Lu, K. Y. Formation Mechanism of Porous Hollow SnO2 Nanofibers Prepared by One-Step Electrospinning. *Express Polym. Lett.* **2012**, *6* (2), 169–176. https://doi.org/10.3144/expresspolymlett.2012.18.

(8) Chang, C.-H.; Rufner, J. F.; Benthem, K. van; Castro, R. H. R. Design of Desintering in Tin Dioxide Nanoparticles. *Chem. Mater.* **2013**, *25* (21), 4262–4268. https://doi.org/10.1021/cm402330u.

(9) Toupance, T.; El Hamzaoui, H.; Jousseaume, B.; Riague, H.; Saadeddin, I.; Campet, G.; Brötz, J. Bridged Polystannoxane: A New Route toward Nanoporous Tin Dioxide. *Chem. Mater.* **2006**, *18* (26), 6364–6372. https://doi.org/10.1021/cm061964d.

(10) Wang, N.; Xu, J.; Guan, L. Synthesis and Enhanced Photocatalytic Activity of Tin Oxide Nanoparticles Coated on Multi-Walled Carbon Nanotube. *Materials Research Bulletin* **2011**, *46* (9), 1372–1376. https://doi.org/10.1016/j.materresbull.2011.05.014.

(11) Agarwal, U. P. Analysis of Cellulose and Lignocellulose Materials by Raman Spectroscopy: A Review of the Current Status. *Molecules* **2019**, *24* (9), 1659. https://doi.org/10.3390/molecules24091659.

(12) Epifani, M.; Tang, P.-Y.; Genç, A.; Morante, J. R.; Arbiol, J.; Díaz, R.; Wicker, S. The Ethylhexanoate Route to Metal Oxide Nanocrystals: Synthesis of CoO Nanooctahedra from CoII2-Ethylhexanoate. *European Journal of Inorganic Chemistry* **2016**, *2016* (24), 3963–3968. https://doi.org/10.1002/ejic.201600511.
(13) Epifani, M.; Arbiol, J.; Díaz, R.; Perálvarez, M. J.; Siciliano, P.; Morante, J. R. Synthesis of SnO2and ZnO Colloidal Nanocrystals from the Decomposition of Tin(II) 2-Ethylhexanoate and Zinc(II) 2-Ethylhexanoate. *Chemistry of Materials* **2005**, *17* (25), 6468–6472. https://doi.org/10.1021/cm051642u.
(14) Zhu, H. J.; Hill, R. H. The Photochemical Metal Organic Deposition of Manganese Oxide Films from Films of Manganese(II) 2-Ethylhexanoate: A Mechanistic Study. *Journal of Non-Crystalline Solids* **2002**, *311* (2), 174–184. https://doi.org/10.1016/s0022-3093(02)01369-8.
(15) Bronstein, L. M.; Huang, X.; Retrum, J.; Schmucker, A.; Pink, M.; Stein, B. D.; Dragnea, B. Influence of Iron Oleate Complex Structure on Iron Oxide Nanoparticle Formation. *Chemistry of Materials* **2007**, *19* (15), 3624–3632. https://doi.org/10.1021/cm062948j.
(16) Kim, T. W.; Kwak, J. K.; Park, K. H.; Yun, D. Y.; Lee, D. U.; Son, D. I.; Han, J. H.; Lee, J. Y. Microstrucural and Optical Properties of SnO2 Nanoparticles Formed by Using a Solvothermal Synthesis Method. *Journal of the Korean Physical Society* **2010**, *57* (6(1)), 1803–1806. https://doi.org/10.3938/jkps.57.1803.
(17) Hanyš, P.; Janeček, P.; Matolı´n, V.; Korotcenkov, G.; Nehasil, V. XPS and TPD Study of Rh/SnO2 System – Reversible Process of Substrate Oxidation and Reduction. *Surface Science* **2006**, *600* (18), 4233–4238. https://doi.org/10.1016/j.susc.2006.01.150.
(18) Hyun, G.; Cho, S.-H.; Park, J.; Kim, K.; Ahn, C.; Tiwari, A. P.; Kim, I.-D.; Jeon, S. 3D Ordered Carbon/SnO2 Hybrid Nanostructures for Energy Storage Applications. *Electrochimica Acta* **2018**, *288*, 108–114. https://doi.org/10.1016/j.electacta.2018.08.064.
(19) Gupta, V. K.; Pathania, D.; Singh, P.; Rathore, B. S.; Chauhan, P. Cellulose Acetate–Zirconium (IV) Phosphate Nano-Composite with Enhanced Photo-Catalytic Activity. *Carbohydrate Polymers* **2013**, *95* (1), 434–440. https://doi.org/10.1016/j.carbpol.2013.02.045.
(20) Chen, T.; Zheng, Y.; Lin, J.; Chen, G. Study on the Photocatalytic Degradation of Methyl Orange in Water Using Ag/ZnO as Catalyst by Liquid Chromatography Electrospray Ionization Ion-Trap Mass Spectrometry. *Journal of the American Society for Mass Spectrometry* **2008**, *19* (7), 997–1003. https://doi.org/10.1016/j.jasms.2008.03.008.
(21) Baiocchi, C.; Brussino, M. C.; Pramauro, E.; Prevot, A. B.; Palmisano, L.; Marcì, G. Characterization of Methyl Orange and Its Photocatalytic Degradation Products by HPLC/UV–VIS Diode Array and Atmospheric Pressure Ionization Quadrupole Ion Trap Mass Spectrometry. *International Journal of Mass Spectrometry* **2002**, *214* (2), 247–256. https://doi.org/10.1016/S1387-3806(01)00590-5.
(22) Rauf, M. A.; Meetani, M. A.; Khaleel, A.; Ahmed, A. Photocatalytic Degradation of Methylene Blue Using a Mixed Catalyst and Product Analysis by LC/MS.

Chemical Engineering Journal **2010**, *157* (2–3), 373–378. https://doi.org/10.1016/j.cej.2009.11.017.

(23) Costantino, F.; Cavaliere, E.; Gavioli, L.; Carzino, R.; Leoncino, L.; Brescia, R.; Athanassiou, A.; Fragouli, D. Photocatalytic Activity of Cellulose Acetate Nanoceria/Pt Hybrid Mats Driven by Visible Light Irradiation. *Polymers* **2021**, *13* (6), 912. https://doi.org/10.3390/polym13060912.

CHAPTER 3: DIRECT FORMATION OF CERIA/PLATINUM NANOSTRUCTURES ON POLYMERIC MATS FOR DEGRADATION OF METHYLENE BLUE DRIVEN BY VISIBLE IRRADIATION

ABSTRACT

In this study, we developed a photocatalytic nanocomposite based on Ceria/platinum hybrid nanoclusters on cellulose acetate fiber mats. The catalytic materials are fabricated by supersonic beam deposition of Pt nanoclusters directly on the surface of electrospun cellulose acetate fibrous mats, which are pre-loaded with a cerium precursor salt. Upon the thermal treatment of the mats, the cerium precursor is converted in the CeNPs. The presence of Pt enhances the oxygen vacancies on the surface of the formed ceria nanoparticles and reduces their band gap, resulting in a significant improvement of the photocatalytic performance of the composite mats under visible light irradiation. The mats reach 70% of degradation efficiency against the MB dye, due to the presence of $^{\bullet}OH$ radicals and holes during the photodegradation process. This study provided a mechanistic insight of the photo driven degradation of organic species in water, and understand the photocatalytic process detecting different type of radicals during the irradiation.

The present chapter is based on: Costantino, F., Cavaliere, E., Gavioli, L., Carzino, R., Leoncino, L., Brescia, R. & Fragouli, D. (2021). Photocatalytic Activity of Cellulose Acetate Nanoceria/Pt Hybrid Mats Driven by Visible Light Irradiation. *Polymers*, *13*(6), 912.[1]

3.1 Introduction

The main goal of the AOPs process is the use of the visible region of solar energy to provide the effective photocatalysis of harmful compound in water. Semiconductor nanoparticles (NPs) with their band-gap (E_g>3.2 eV), show excellent photocatalytic activity under ultraviolet (UV) irradiation, which represents only ~5% of the entire solar energy.[2] A possible solution to improve the semiconductor NPs efficiency is to lower their E_g by coupling with metallic NPs, or doping them with transition or noble metals.[3–5]

In this chapter, we describe a novel photocatalytic system for the degradation of aqueous organic pollutants under visible light irradiation, by, exploiting Pt nanoclusters (PtNCs) deposition onto a hybrid polymeric fibrous membrane and subsequent *in situ* formation of ceria NPs. Specifically, PtNCs are deposited by Supersonic Cluster Beam Deposition (SCBD) on the surface of electrospun cellulose acetate (CA) mats pre-loaded with a cerium (IV) salt precursor. We investigate the effect of different PtNCs amounts on the CeNPs growth and on the properties of the hybrid mats, as well as on the membranes' photocatalytic performance under visible light irradiation.

We evaluate the effect of the adsorbed methylene blue (MB) on the photocatalytic performance of the mats, and we demonstrate that the presence of PtNCs improves significantly the photocatalytic activity of the mats reaching an overall degradation efficiency of 70%. This is attributed to the enhanced oxygen vacancies on the surface of the formed ceria nanoparticles and to their reduced band gap energy. The study of the photodegradation mechanism demonstrates the formation of reactive oxygen species (ROS) during the photocatalytic process such as holes and hydroxyl radicals (•OH), which

are prominent species during the dye degradation. The results demonstrate that, with this versatile method, it is possible to fabricate flexible and easily handled polymeric nanocomposite fibrous mats for visible light-induced photocatalytic applications.

3.2 Materials and Method

3.2.1 Chemicals

Cellulose Acetate (CA, average MW~40.000 Da), Ammonium Cerium (IV) Nitrate (CePrec, $H_8CeN_8O_{18}$, 99,99%), Acetone (> 99.5%, GC grade), N,N-Dimethylformamide (DMF, Cromasolv Plus), Isopropyl alcohol (ISO, C_3H_8O <100%), Formic acid (FA, CH_2O_2, >100% ACS reagent), Fluorescein salt (FL, $C_{20}H_{12}O_5$ >100%), Thymoquinone (TQN, $C_{10}H_{12}O_2$, <100%) and Methylene Blue (MB, $C_{16}H_{18}ClN_3S$, <100%) were purchased by Sigma Aldrich. All chemicals were used as received without further purification.

3.2.2 Fiber preparation

Typically, 1.00 g of CA polymer was dissolved in 10 mL of an Acetone/DMF (volume ratio 7:3) mixture by stirring at 50°C and 400 rpm until a clear solution was obtained. Subsequently, 0.107 g of CePrec were dissolved in 5 mL of the same solvent mixture (Acetone/DMF, volume ratio 7:3) upon stirring at 45°C and 400 rpm for 30 min. Then, the two solutions were mixed and left under stirring for 24h to obtain a stable solution. Electrospinning was performed in a closed box using a vertical geometry. The solution was placed in a 10 mL syringe and a syringe pump (NE-1000, New Era Pump Systems Inc.)

was used to control the flow rate, while a blunt 19-gauge needle was used as spinneret. The needle was connected to a positive electrode of a high voltage power supply, while the aluminum collector was grounded. The spinning voltage, the nozzle-collector distance and the injection flow rate were 25 kV, 20 cm and 0.2 mL/h, respectively. The obtained fiber mats (CA/CePrec) were dried under low vacuum for 10 h in order to remove any solvent residue.

The surface of the prepared mats was decorated with PtNCs deposited by SCBD, a gas phase synthesis method producing a beam of nanoclusters from a target rod of the desired material. In this work PtNCs were obtained from a Pt rod (purity 99.99%) using He at P=50 bar as a carrier gas. The plasma generated by a 0.9 kV pulsed discharge ablates the Pt rod generating NPs that are extracted through a set of aerodynamic lenses and reach the sample's surface. The amount of the deposited PtNCs is measured by a quartz microbalance and by AFM on a silicon substrate co-deposited with the mat substrate, and is expressed as an equivalent layer thickness. The thickness of the PtNCs layers deposited on the mats were measured to be either 1 nm or 5 nm.

To promote the nucleation and growth of CeNPs with or without the presence of PtNCs, the fibrous mats with the CePrec were placed in an oven at 150°C for 48 hours in air (see Scheme 3). Considering a total conversion of the precursor salt in metal oxide, the expected CeO_2 NPs content is approximately ~8% wt. with respect to the polymer. The fabricated mats will be called for simplicity: CA/CePrec, CA/CeNPs, CA/CeNPs/Pt1 and CA/CeNPs/Pt5 and correspond to the CA mats loaded with precursor, thermally induced

grown CeNPs, and thermally induced grown CeNPs with PtNCs at the two different deposition conditions, respectively (i.e 1 nm and 5 nm).

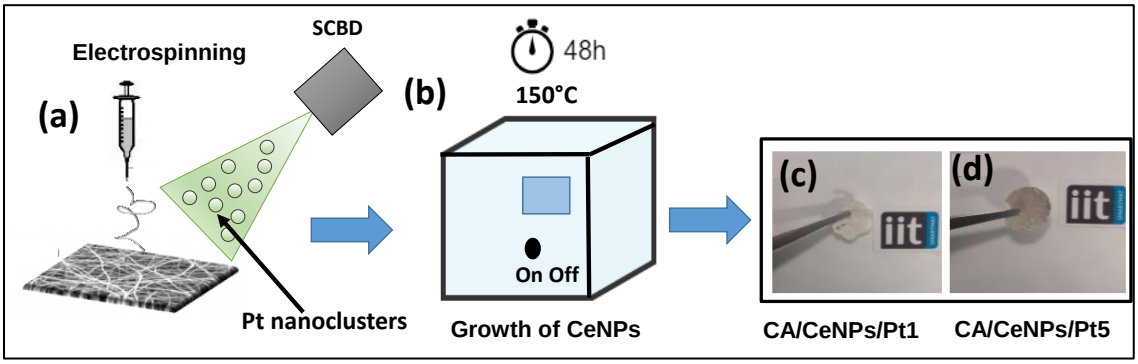

Scheme 3. Procedure for the preparation of CA/CeO_2 fiber mats, (a) starting from the electrospinning of CA/CePrec (b) the subsequent SBCD of Pt nanocluster in the surface of the mats, followed by the thermal treatment of the fiber at 150°C for 48h. The pic (c) and (d) represent the CA/CeNPs/Pt1 and CA/CeNPs/Pt5 respectively.

3.3 Photocatalytic tests

The photocatalytic activity of all the prepared mats was studied by monitoring the MB concentration change upon irradiation with visible light irradiation. The MB concentration variation was determined with UV-visible absorption spectroscopy using a Varian Cary 6000i (Agilent), by monitoring the absorption peak of MB at 664 nm and by correlating the absorbance with the concentration using a calibration curve (see Appendix C Figure C3 and related discussion).

For each experiment, 3 mL of the MB dye (5 ppm) aqueous solution was placed in a quartz cuvette containing 0.005 g of the fibrous mat suspended in it. Then, the cuvette was placed under a fluorescent lamp (LT-T8, 15W Colourlux plus) emitting in the 400 to 600 nm wavelength range.

Two types of degradation experiments were conducted. In the first one, before any irradiation, the mats were maintained in contact with the dye solution overnight while in the second case the mats were left in contact with the dye for 1 h, both under dark conditions.

The degradation efficiency (%) was calculated using the equation (2.1) see Chapter 2, paragraph 2.3. While the rate constant of the photodegradation process (k, min^{-1}) was calculated by fitting the experimental data with the pseudo-first order kinetics model expressed in the equation (3).

$$\ln \frac{C_0}{C} = kt \qquad (3.1)$$

Before and after the photocatalytic degradation of the MB, the total organic carbon (TOC) was determined by the MembraPure uniTOC analyzer. Before the analysis, all samples were filtered with a PTFE membrane (0.2 μm pore size), and then 1 mL of each solution was further diluted with 20 mL of milliQ H_2O. The mineralization efficiency (%) is calculated considering the equation (2.2).

3.4 Reactive Oxygen Species Identification

To determine the •OH formation during the visible light irradiation of the fibrous mats, the fluorescein (FL) sodium salt was used as selective radical quencher. In particular, for each type of mat, 0.005 g of the sample was added in 3 mL of an aqueous solution of FL (8 μM) in a 1 cm path length quartz cuvette, and then the irradiation with visible light for 270 min, in the same conditions as described in the photocatalytic experiments, took place. The •OH formed by the mats upon irradiation react selectively with the FL, and therefore their

concentration was calculated using equation (3.4), by monitoring the time-dependent reduction of the emission peak of the FL at 515 nm, using a Fluoromax ®- 4 Spectrofluorimeter (excitation wavelength: $\lambda_{ex} = 303$ nm). The variation of the emission peak intensity was attributed to the variation of the FL concentration, which was deduced by a calibration process, which correlates the emission intensity of an unknown concentration to the intensity of known FL concentrations (see Appendix C, Figure C2). In particular, the evolution of the FL concentration during the visible light irradiation in the presence of the fibrous mat is attributed to its equimolar reaction with the •OH formed by the mats. Therefore, the [•OH] concentration, is calculated by Equation 3.4:

$$[^{\bullet}OH] = \Delta[Fl] = \Delta I/slope \quad (3.4)$$

Where ΔI is the difference of the initial emission intensity I_0, and the intensity at a specific time I_t (I_0-I_t) at λ_{em}=515 nm, while the *slope* is obtained from the calibration curve (see Appendix C).

For identifying the ROS (Reactive Oxygen Species) during the photocatalysis, three quenchers were added in an aqueous solution of 5 ppm MB: 1 mM of a hydroxyl radicals quencher (isopropyl alcohol, Sigma-Aldrich, > 99.7%), 1 mM of a superoxide radicals quencher (thymoquinone, Sigma-Aldrich, > 98%), 1 mM of an electron holes quencher (formic acid, Sigma-Aldrich, > 99%), respectively. For each case, 3 mL of the prepared solution was left in contact with 0.005 g of the mats for 1 hour in dark. Subsequently the irradiation with visible light was conducted following the same process as described in the photocatalytic experiments and the absorption peak intensity of MB at 664 nm before and after 270 min of irradiation was recorded.

3.5 Results and Discussion

3.5.1 Morphological Characterization of the mats

All the electrospun mats developed, even after deposition of the PtNCs and thermal treatment, consist of a net of randomly distributed defect-free polymeric fibers in the micron and submicron size range, and irregularly shaped interconnected pores as can be seen from a representative image in the Figure 3(a). This proves that the deposition of the PtNCs and the thermal treatment for the CeNPs formation, do not alter the mats' morphology at the microscale, see Figure 3(a,h). After the thermal treatment the EDS mapping shows that the fibers' composition is homogeneous at the micrometric scale, as well as the Ce and Pt distribution (see Figure 3(b)-(i)). As determined by EDS analyses, the Pt/C atomic ratio is more than 10 times higher for the CA/CeNPs/Pt5 mats (0.0034) compared to the CA/CeNPs/Pt1 (0.0003), in line with the SCBD deposition time, while the Pt/Ce atomic ratio is 0.02 and 0.37 for the CA/CeNPs/Pt1 and CA/CeNPs/Pt5 respectively (see Table 3).

The coexistence of Pt and Ce in the form of NPs is indicated by the STEM-EDS elemental mapping of the CA/CeNPs/Pt1 and CA/CeNPs/Pt5 samples (Figure 3.1 (b-f)) after the removal of the CA polymer. In particular, in both cases, features in the form of NPs are evident, and the CeNPs (red) are distributed all over the PtNCs (green), indicating that they grow in close contact with them, as the nanostructures are co-localized, densely packed, and with a uniform distribution.

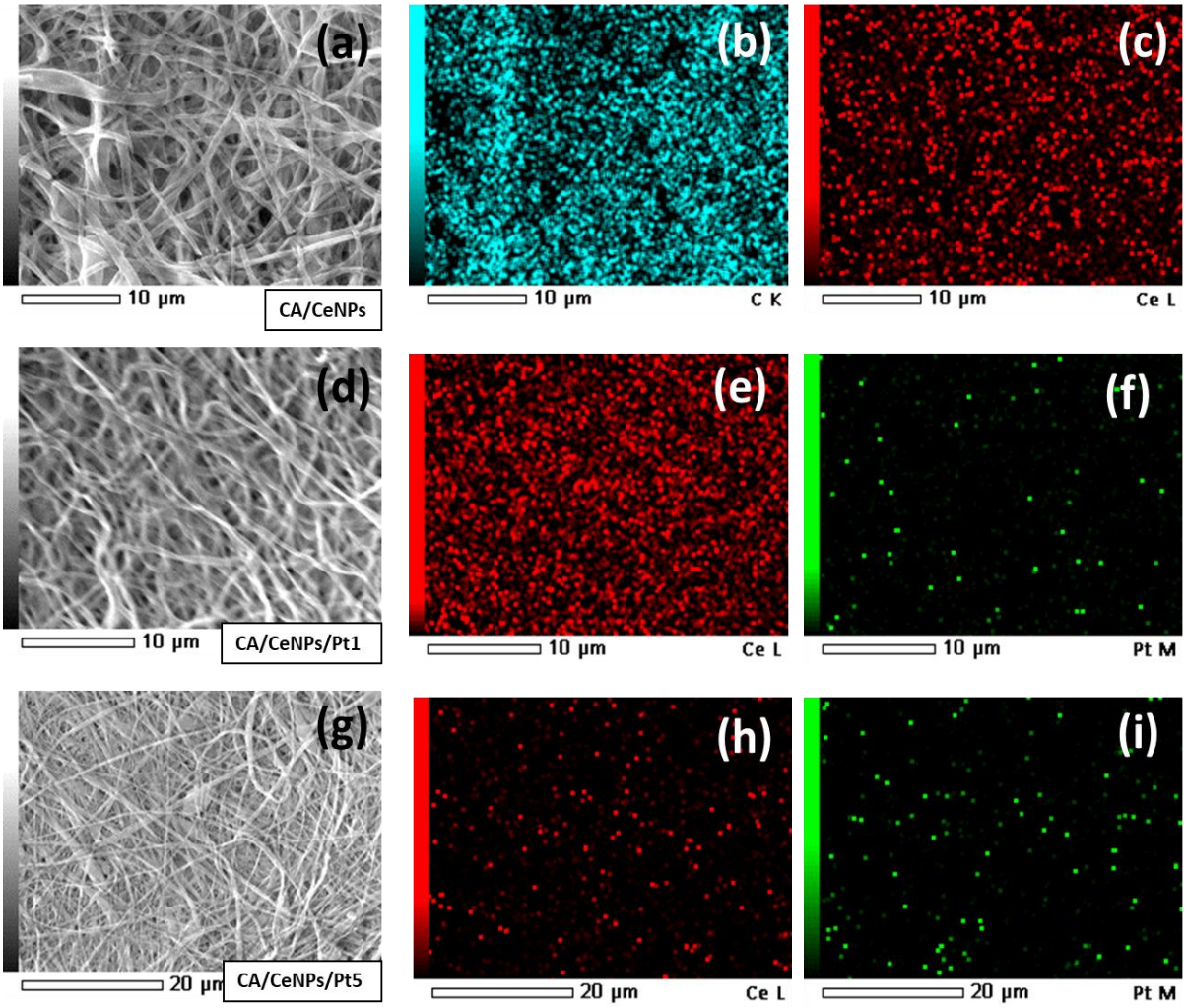

Figure 3. Top view SEM image of (a) CA/CeNPs and corresponding EDS mapping of the surface of fiber mats (b) elemental maps for C, (c) and Ce. (d) SEM image of CA/CeNPs/Pt1 and corresponding EDS analysis of the surface (e) for Ce and (f) for Pt. (g) SEM image of CA/CeNPs/Pt5 and corresponding EDS analysis of the surface (h) for Ce and (i) for Pt.

Table 3. Atomic percentage (%) of elements on the surface of the mats (according to SEM-EDS analysis)

Samples	C (%)	O (%)	Ce (%)	Pt (%)
CA/CeNPs	**75.87**	**22.62**	**1.03**	**-**
CA/CeNPs/Pt1	**76.70**	**21.81**	**1.06**	**0.02**
CA/CeNPs/Pt5	**73.13**	**25.51**	**0.67**	**0.25**

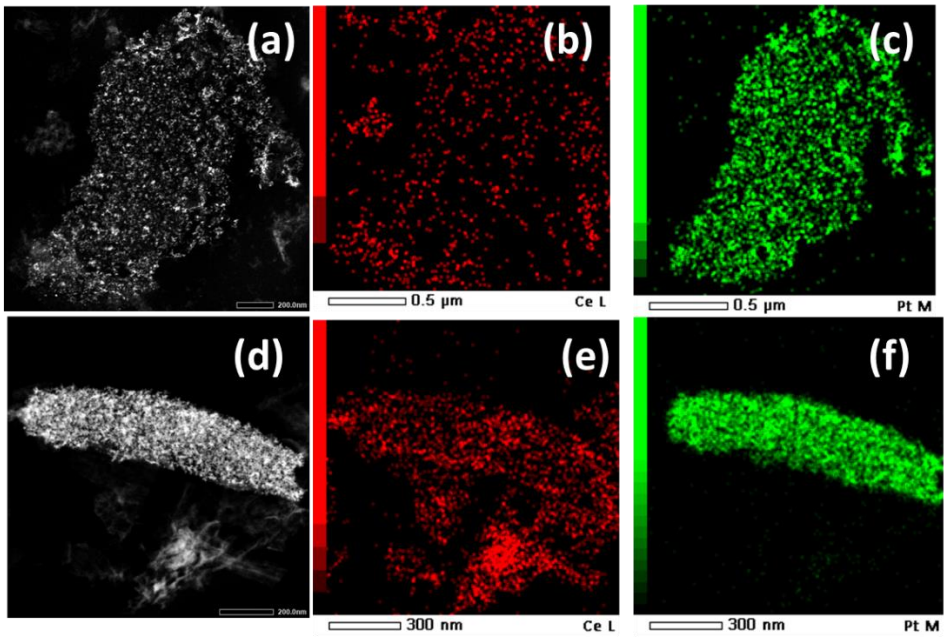

Figure 3.1. Annular-Dark-field STEM images and the corresponding STEM-EDS mapping of the (a-c) CeNPs/Pt1 and (d-f) CeNPs/Pt5 (red indicates the Ce and green the Pt element).

In all samples, the CeNPs have spherical shape with mean size ranging between 2-3 nm depending on the sample type (Figure 3.2). The SAED patterns of the particles (Figure 3.2 (b,d,f)) exhibit a sequence of diffraction rings, as expected for randomly oriented nanocrystals..

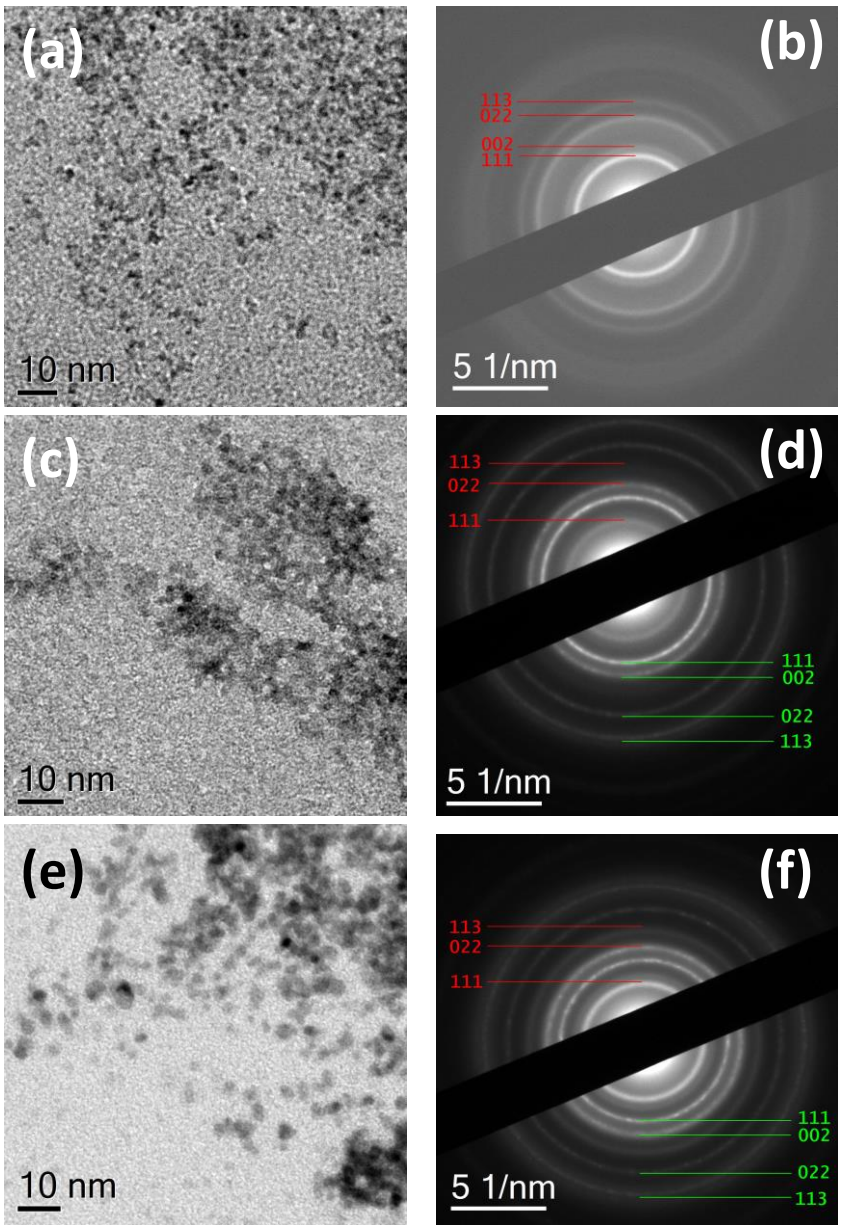

Figure 3.2. (a) Overview BFTEM images of cerium NPs (from sample CA/CeNPs), (c) Cerium (CeO2) NPs from sample CA/CeNPs/Pt1 and (e) cerium NPs and Pt aggregates from CA/CeNPs/Pt5. To the right the SAED pattern of (b) CeNPs and (d), (f) SAED patterns of sample CeNPs/Pt1 and CeNPs/Pt5 respectively. The diffraction rings in the patterns are indexed according to the database (ICSD) structures 55284 (CeO2) and 243678 (Pt).

In particular, for all samples the patterns confirm the presence of crystalline CeNPs (CeO_2 with a fluorite cubic structure) and the presence of randomly oriented crystalline PtNCs, as

clearly evidenced in the CA/CeNPs/Pt1 and CA/CeNPs/Pt5 samples (Figure 3.2 (d,f)). The mean size of the CeNPs formed in the presence of the PtNCs is slightly increasing from the Pt-free mats to the Pt-rich mats: 2.02±0.61nm for CA/CeNPs, 2.55±0.66nm for CA/CeNPs/Pt1 and 3.14±0.85nm for CA/CeNPs/Pt5 (as reported in the Figure 3.3 and Table 3.1). This suggests that the PtNCs presence on the surface of the mats influences the nucleation and growth of CeNPs.[6,7]

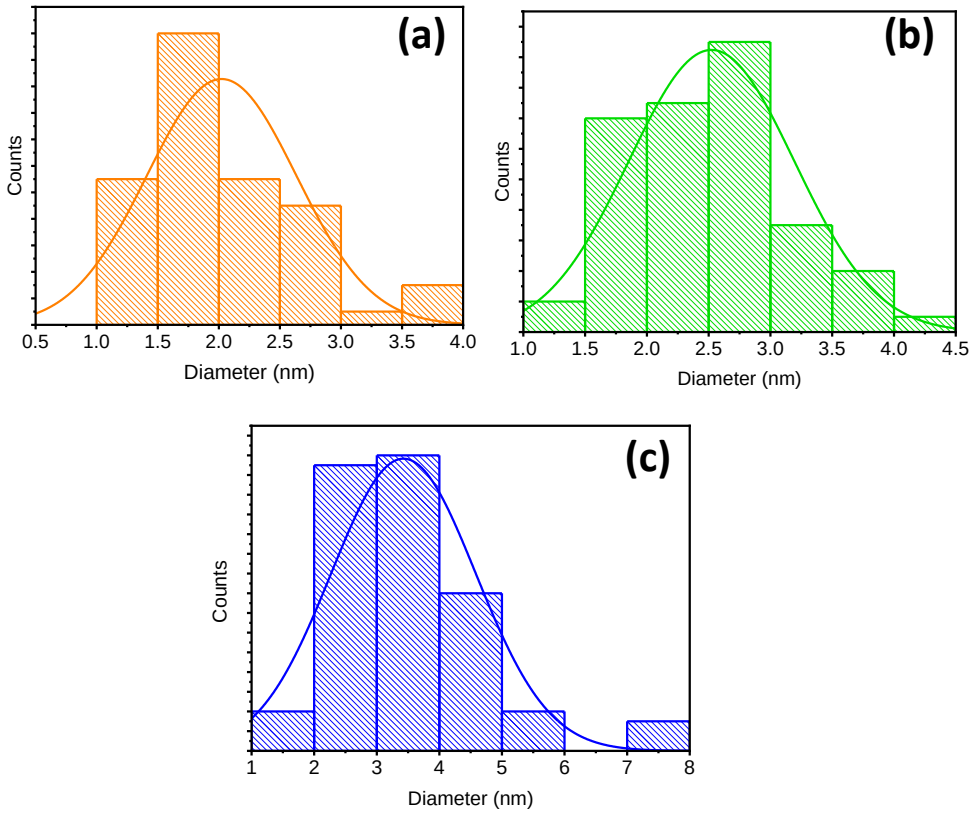

Figure 3.3. Size distribution of NPs (a) CeNPs, (b) CeNPs/Pt1, (c) CeNPs/Pt5.

Table 3.1. Size of NPs calculated from the TEM analysis.

Method	**TEM**
Samples	**Size (nm)**
CA/CeNPs	2.0±0.6
CA/CeNPs/Pt1	2.6±0.7
CA/CeNPs/Pt5	3.1±0.8

The single-crystal nature of individual Pt and Ce particles is further confirmed by the HR-TEM analysis, and Figure 3.4 shows the representative example of the NPs present in the CA/CeNPs/Pt5 mats. A closer look to the Figure 3.4 further demonstrates that the CeNPs grow in contact with the PtNCs, which is also supported by the STEM-EDS analysis as can be seen from the Figure 3.5, where the CeNPs appear uniformly dispersed and anchored to the PtNCs.

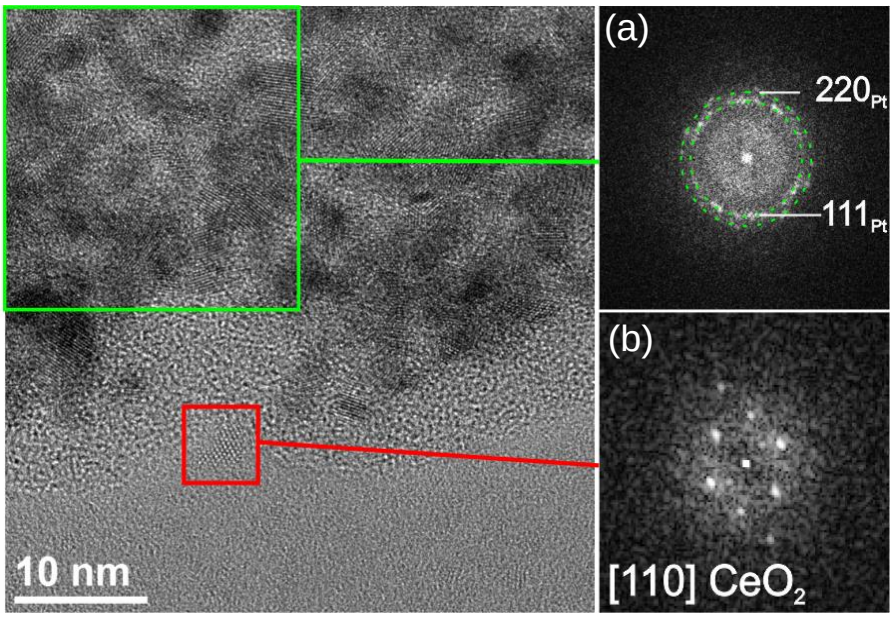

Figure 3.4. HR-TEM images of the edge region of CA/CeNPs/Pt5 and Fast Fourier transformation (FFT) analysis of (a) a groups of PtNCs and (b) a CeNPs, respectively.

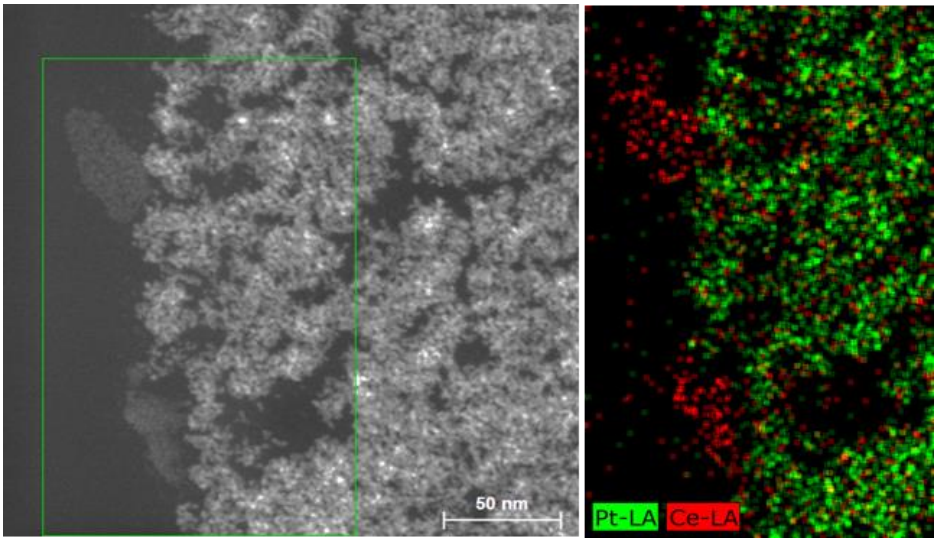

Figure 3.5. (Left) HAADF-STEM image and (right) corresponding STEM-EDS mapping of the selected surface of CA/CeNPs/Pt5 sample.

The XRD data shown in Figure 3.6 indicate the prevalence of the CeO_2 crystalline phase in all the prepared mats. In accordance to SAED profiles, see Figure 3.7 (a-b), all samples

present the main diffraction peaks at 28.5°, 33.1°, 47.5°, 56.3° and a small peak at 69.4°, which are assigned to the reflections from the (111), (002), (022), (113) and (004) lattice planes of cerium oxide (ICSD: 55284), with no evidence of Ce_2O_3 or $Ce(OH)_3$ crystalline structures.[6] The Pt crystalline phase is not detected due to the low concentration of the PtNCs as compared to the CeNPs. However, the presence of the Pt is detected in the SAED spectra of the final nanocomposites as can be seen from the Figure 3.7 (a, b).

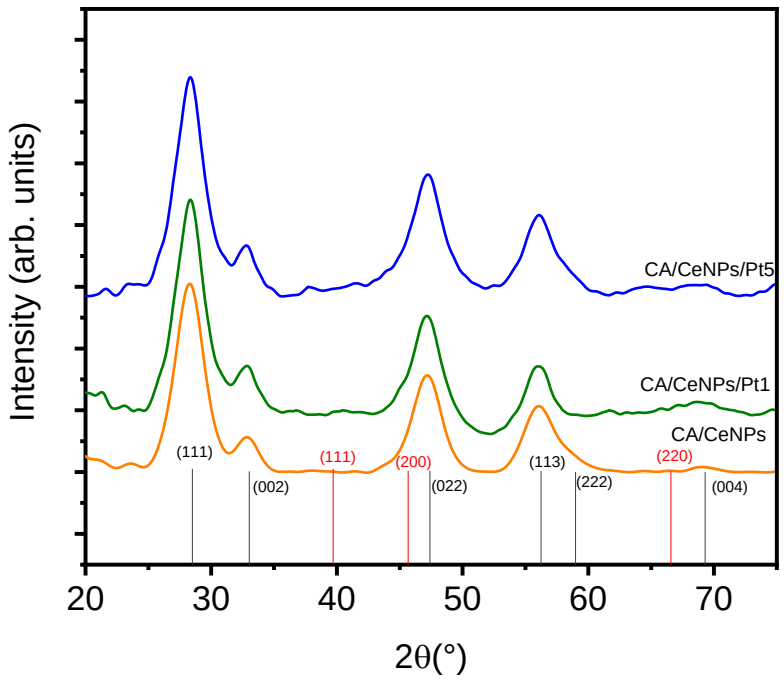

Figure 3.6. XRD diffractogram of all prepared fiber mats, CA/CeNPs (orange line), CA/CeNPs/Pt1 (green line) and CA/CeNPs/Pt5 (blue line). At the bottom, CeO_2 patterns ICDD: 96-900-9009 (black) and Pt patters ICDD: 00-004-0802 (red).

.

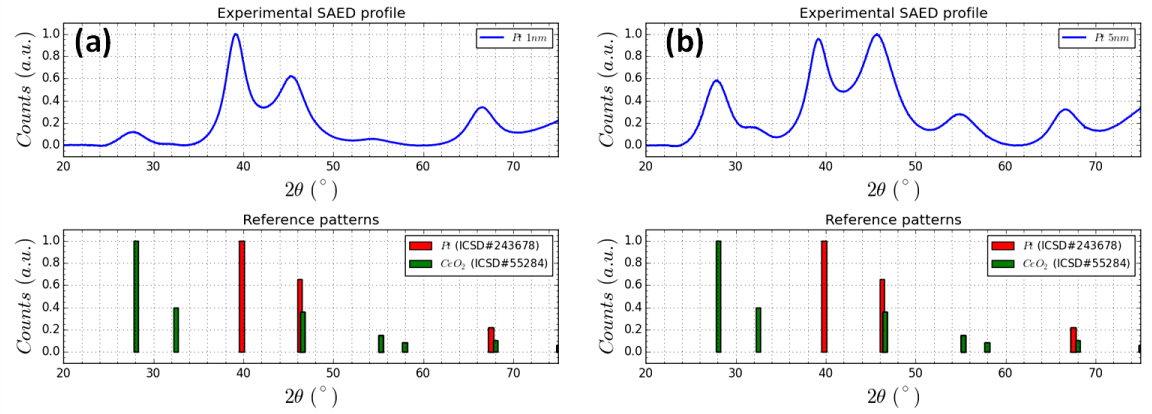

Figure 3.7. Profiles obtained by azimuthal integration, followed by background subtraction, from SAED patterns of (a) CeNPs/Pt1 and (b) CeNPs/Pt5, proving the presence of crystalline CeNPs and PtNCs in accordance with the references (ICSD:#55284) and (ICSD:#243678) respectively. Processing of SAED patterns (azimuthal integration + background subtraction) was carried out using the PASAD plugin of Gatan Digital Micrograph. The 2θ Bragg value was calculated assuming the kα line of Cu, for ease of comparison with XRD data.

The surface chemistry of the mats is investigated with XPS. All mats present the Ce3d, O1s and C1s peaks, with the CA/CeNPs/Pt mats showing also the metallic Pt (4f) as shown in the Figure 3.8 (a,b).[8] The atomic concentrations listed in Table 3.2 indicate that C (carbon) is slightly increased and O (oxygen) is slightly reduced in the presence of Pt. While, the Ce % on the surface of the mats is not significantly altered by the presence of the Pt in the surface composition of the CA/CeNPs/Pt mats. For all the prepared mats, the detailed Ce3d spectrum exhibits Ce $3d_{5/2}$ and Ce $3d_{3/2}$ spin-orbit peaks, indicating the co-existence of Ce^{3+} and Ce^{4+} bonding states. When the CePrec, is introduced in the CA polymer and the CA/CePrec mats are formed, the composition of the precursor's Ce oxidation states (Ce^{4+} and Ce^{3+} 70% and 30% respectively, as deduced from the spectra deconvolution) does not vary as can be seen from the Figure 3.8 (c). However, after the thermal treatment the profile of the peaks changes significantly (Figure 3.8 (d)), indicating that the Ce^{3+} state prevails significantly over the Ce^{4+}.

Table 3.3. Atomic compositions (%) of all prepared fiber mats

Samples	C (%)	O (%)	Ce (%)	Pt (%)
CA	69.78	30.21	/	/
CA/CeNPs	69.95	29.72	0.32	/
CA/CeNPs/Pt1	71.47	23.43	0.24	3
CA/CeNPs/Pt5	76.47	20.21	0.30	4

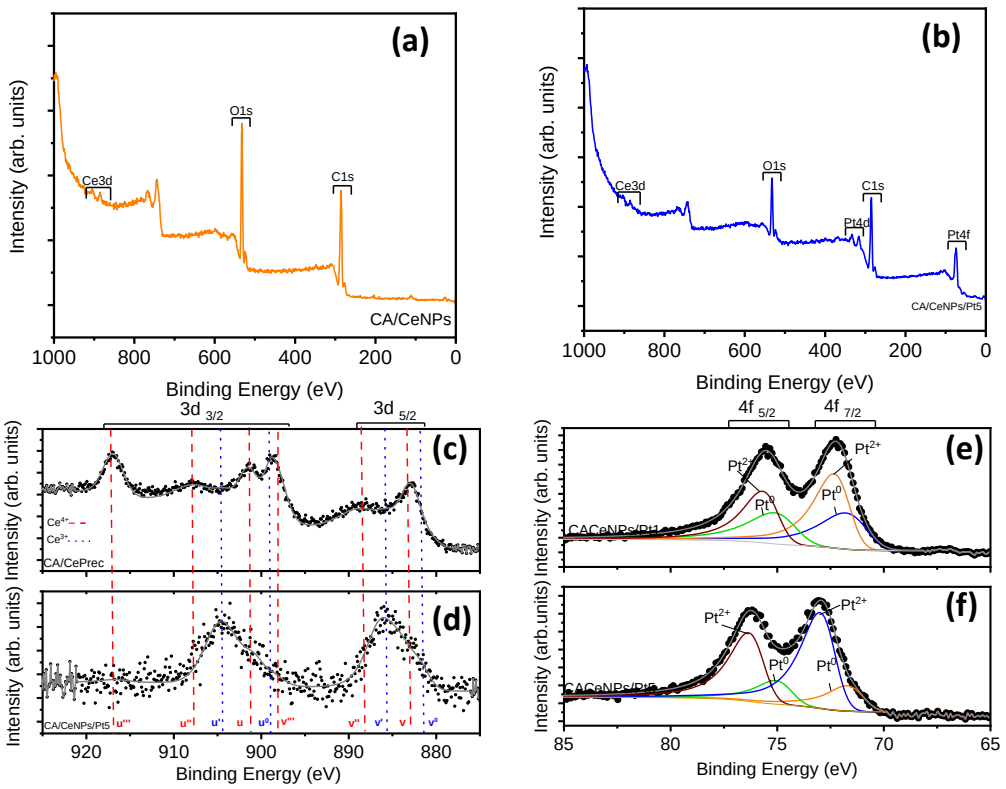

Figure 3.8. Survey XPS spectrum of (a) CA/CeNPs, (b) CA/CeNPs/Pt5, and high resolution Ce3d XPS spectrum of (c) CA/CePrec and (d) CA/CeNPs/Pt5 (red dashes for Ce4+ and blue dashes for Ce3+). High-resolution XPS spectra of platinum (Pt4f) in the (e) CA/CeNPs/Pt1 and (f) CA/CeNPs/Pt5.

The deconvolution of the O1s spectra of the bare CePrec and CA/CePrec reveals the presence of two distinct peaks, see Figure 3.9 (a) and Figure 3.9 (b) respectively. The one

at 530.08 eV can be attributed to the Ce^{4+}-O lattice, whereas the one at 532.66 eV can be assigned to both the Ce^{3+}-O lattice and to the overall oxygen groups in the CA matrix (O=C, O-C, O-H) (see Figure 3.9).[9,10] After thermal treatment, the signal attributed to the Ce^{4+}-O lattice disappears, and the O1s peak located around 532.5eV range (see Figure 3.9 (c)) can be attributed to the overall oxygen groups of the cellulosic membrane, as well as to the oxygen vacancies possibly due to the prevalent presence of Ce^{3+} on the surface of the mats.[10]

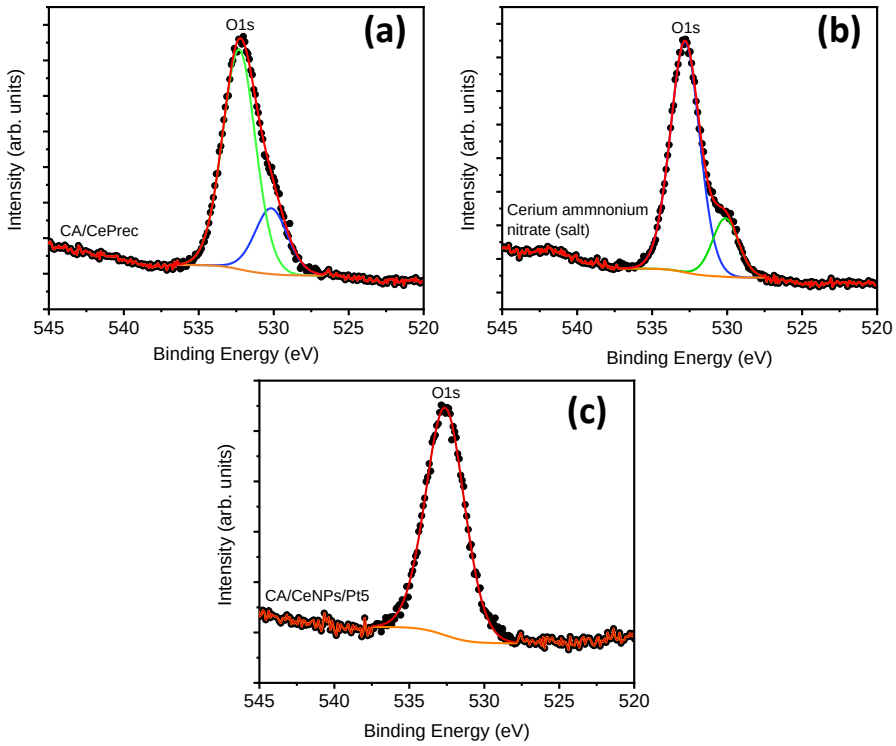

Figure 3.9. O1s XPS spectra of (a) CePrec (salt), (b) CA/CePrec, (c) CA/CeNPs/Pt5**.**

Concerning the CA/CeNPs/Pt mats, the Pt4f spectra (Figure 3.8 (e-f)) present the typical binding energies of Pt species in the Pt (4f) region due to the presence of multiple oxidation states. In particular, the signals of Pt ($4f_{5/2}$ and $4f_{7/2}$) were deconvoluted into two sets of

spin-orbit doublets, indicating the presence of Pt in two forms, the Pt^0 and Pt^{2+} on the surface of the mats, the latter being present as PtO or $Pt(OH)_2$.[11,12] Therefore, considering that the Pt deposition on the mats was performed using a fully metallic (Pt^0) rod in vacuum, the subsequent thermally induced growth of the CeNPs in air may cause the modification of its oxidation state. In fact, it has been proved that the oxidation state of Pt can be modified by thermal treatment in air, as also by the presence of Ce^{3+}/Ce^{4+} and related species.[7,12]

The presence of the trivalent Ce^{3+} ions on the surface of the CA/CeNPs, CA/CeNPs/Pt1 and CA/CeNPs/Pt5 mats, is strictly related to the number of oxygen vacancies and the presence of Ce_2O_3 or $Ce(OH)_3$.[13]

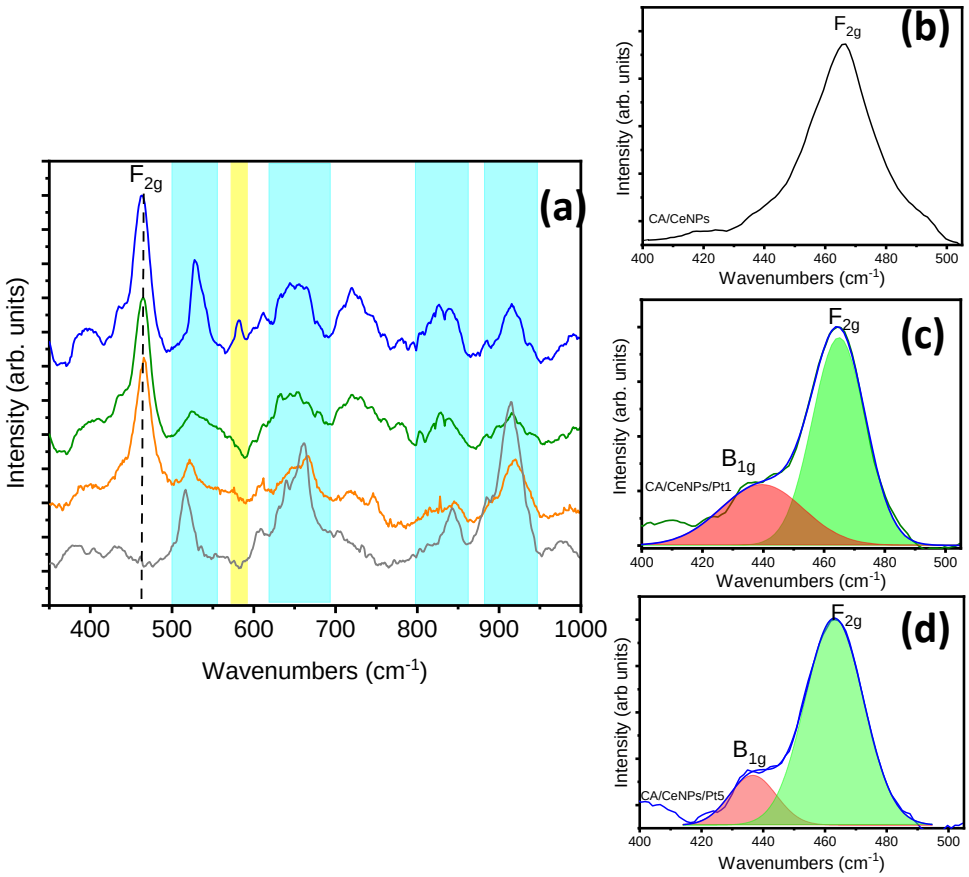

Figure 3.10. (a) Raman spectra of all fibrous mats, CA/CeNPs (orange line), CA/CeNPs/Pt1 (green line) and CA/CeNPs/Pt5 (blue line) and CA (therm. treated) matrix (grey line). The blue shadowed peaks correspond to the CA signals and the yellow to the vibrational mode of CeNPs at 580cm-1. (b) Deconvoluted Raman spectra of CA/CeNPs (c) CA/CeNPs/Pt1 and (d) CA/CeNPs/Pt5 in the region 400-500cm-1 show the F2g peak characteristic of CeO2 and the B2g signal referred to PtNCs.

To have an insight on this, the micro-Raman spectra of all prepared mats were acquired, and reported in Figure 3.10 (a). In all cases, the signals of the CA polymer matrix appear in the region from 300 cm^{-1} to 550 cm^{-1}, and are assigned to the C-C-C, O-C-O and C-C-O deformations, while the peaks at 918, 834, 659 and 350 cm^{-1} are attributed to the vibrations of the C-H, O-H, C-OH and C-O bonds respectively.[14,15] In comparison to the CA polymer before any treatment, it should be mentioned that some peaks become sharper

and more evident after the thermal treatment, due to the formation of crystal domains in the structure of the amorphous CA.

Apart from the presence of the characteristic peaks of the CA matrix, the Raman spectra clearly demonstrate the presence of the F_{2g} mode, originating from the symmetric stretching of the octahedral CeO_8, of the CeO_2 cubic fluorite structure at about 466.0 cm^{-1}.[16,17] On the basis of the theoretical work performed by Xu et al the F_{2g} mode is attributed to the breathing vibration of the wagging O atom between two Ce^{4+} ions, and the peak position varies with the length of the Ce-O bonds due to the formation of oxygen defects or the doping metal ions.[18]

In the present mats, a slight red shift of the peak is observed when the CeNPs grow in the presence of the PtNCs (from 465.7 cm^{-1} for the CA/CeNPs to 464.6 cm^{-1} for the CA/CeNPs/Pt1 and to 463.9 cm^{-1} for the CA/CeNPs/Pt5).[19] The red shift observed can be attributed to the conversion of the Ce^{4+} to the Ce^{3+} oxidation state with localized electrons in the 4f state and the formation of oxygen vacancies in the CeNPs lattice structure in the presence of Pt. In fact, the higher number of oxygen defects in the PtNCs loaded mats results to the slight expansion of the CeNPs supercell, due to the larger radius of the Ce^{3+} (1.07 Å) ions compared to that of Ce^{4+} (0.97 Å), and to the slight elongation of the Ce-O bonds.[20]

Concerning the PtNCs loaded mats, the Pt has two Raman active modes the B_{1g} and E_g.[19] The B_{1g} is located at ~438 cm^{-1} in both cases very close to the vibrational signal of ceria and for this a deconvolution method is adopted to prove its presence as reported in the Figure 3.10 (c,d). The E_g mode is located at 657 cm^{-1}, but the presence of the polymer

matrix makes it difficult to detect. The B_{1g} mode can be related to the presence of PtO species in the surface of mats, in agreement with the XPS analysis. Most importantly, the peak appearing at ~580 cm^{-1} in the CA/CeNPs/Pt5 sample can be assigned to the bridging Pt−O−Ce vibration i.e. to the interaction between PtNCs and CeNPs, strongly supporting the hypothesis that the CeNPs grow in close contact to the PtNCs.[7,20]

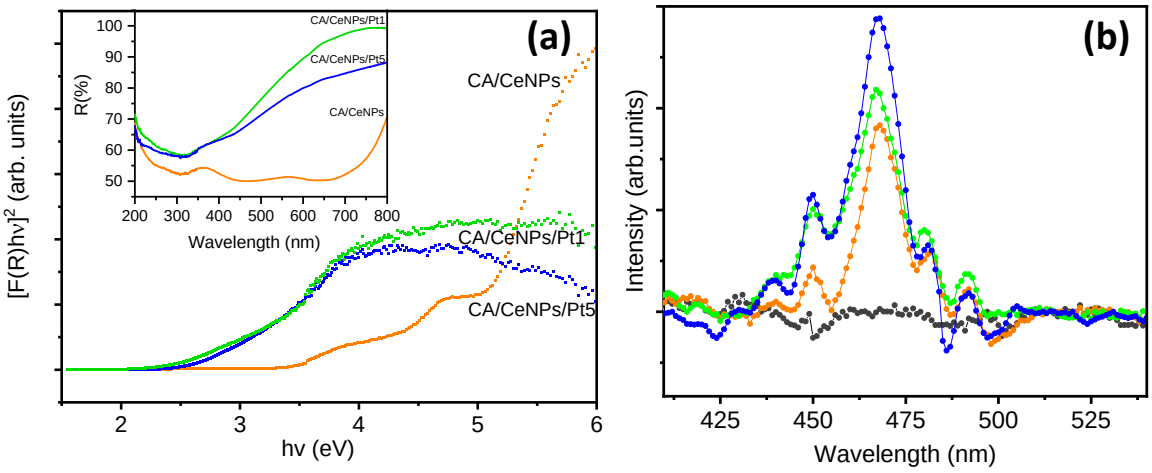

Figure 3.11. (a) Reflectance spectra (inset) and Kubelka-Munk approximation of fibrous mats: CA/CeNPs (orange), CA/CeNPs/Pt1 (green) and CA/CeNPs/Pt5 (blue). (b) Fluorescence emission spectra of all prepared fibrous mats: pristine CA (black), CA/CeNPs (orange), CA/CeNPs/Pt1 (green) and CA/CeNPs/Pt5 (blue) (excitation wavelength λ_{exc}=350 nm).

The evaluation of the E_g was carried out by UV-Vis DRS. As shown in the inset of Figure 3.11 (a), the R(%) spectrum of the CA/CeNPs presents a peak at 364 nm, which is related to the charge transfer from the 2p level of O to the 4f level of Ce and to the electronic transition 4f→5d in Ce^{3+}, while it is not detected when CeNPs grown in the presence of the PtNCs, because the presence of the noble metal causes the enhancement of the absorption in the visible range.[21]

In order to evaluate the E_g of all the fiber mats, the Kubelka-Munk approximation was used (details presented in the Appendix B). Two energy values, were derived, which could be

attributed to the E_g (3.3 eV) and to a possible "mid-gap" (4 eV), due to the energy states generated by defects of the ceria, within the gap, mainly by oxygen vacancies that exist in the CeNPs and that could be formed by the CeO_2 to Ce_2O_3 reduction reaction.[9,22] On the other hand, in the presence of Pt, the E_g decreases from 3.3 eV to 2.6 and 2.4 eV for CA/CeNPs/Pt1 and CA/CeNPs/Pt5 respectively, denoting that the absorption window of the mats is red-shifted, allowing thus to have a photocatalysis activated by visible light.

The modification of the E_g and the increase of oxygen vacancies are due to the modification of the valance band in the nanostructure by the coexistence of CeNPs and PtNCs on the surface of the mats. In particular, the decrease of the E_g can be attributed to the presence of Ce^{3+} at the grain boundaries with PtNCs, which were able to modify the electronic structure in the oxidation states of CeNPs.[7] The E_g decreases with the increase of Ce^{3+} and Pt concentration and by the presence of oxygen vacancies on the surface of the membrane, which are able to form an interface with some localized gap states. On the basis of computational studies, CeNPs in contact with Pt clusters have modified electronic density. In particular, the Pt facilitates the formation of oxygen vacancies at the metal particles surface, and this implies the creation of centers with propensity for reduction and, at the same time, the formation of holes in the boundaries of cerium, which are good centers for the oxidation process.[23]

To get an insight to the recombination of photogenerated carriers with oxygen vacancies and defects by the coexistence of Ce^{3+}/Ce^{4+} species, PL studies were performed for all the prepared fibrous mats (Figure 3.11 (b)). The emission peaks between 450 nm and 500 nm, are mostly associated with oxygen vacancies, such as F^+ (oxygen vacancies with one

trapped electron), F^{2+} (oxygen vacancies without any electron) and F (oxygen vacancies with one electron).[24] In particular, in the fluorite CeO_2 structure, the oxygen atoms are not closely packed, so they could form many oxygen vacancies, while maintaining the basic fluorite structure.[22] The CA/CeNPs loaded with PtNCs showed a higher PL intensity with respect the bare CA/CeNPs, which leads to an enhancement of the optical properties. Therefore, the high intensity can be related of high content of oxygen vacancies and an increase of Ce^{3+} and other defects. In particular the higher intensity observed in the case of CA/CeNPs/Pt5 than CA/CeNPs/Pt1, suggests a higher separation rate of photoinduced charge carriers, higher separation between the photoelectrons and holes and subsequently more efficient oxidative process.

3.6 Photocatalytic degradation performance under visible light irradiation

When heterogeneous photocatalysts are used for pollutants removal under light irradiation, both adsorption processes and photocatalytic activity are critical for the photodegradation process. Therefore, to establish how the contact of the dye with the fiber mats in the dark may influence the photodegradation mechanism, two different pretreatment conditions were adopted before the light irradiation: the mats and MB solutions are left in contact under dark i) overnight or ii) for 1 hour.

As can be seen from the Figure 3.12 (a), when the mats are left overnight under dark in contact with the MB solution, a decrease of the absorbance is observed in all cases. This can be attributed to the MB physical adsorption of the dye on the surface of the mats by electrostatic interactions with the porous CA network. Here the adsorption efficiency for

overnight interaction is of 10% and further increases in the presence of the CeNPs and the PtNCs (22%, 19% and 16% for CA/CeNPs, CA/CeNPs/Pt1 and CA/CeNPs/Pt5, respectively).

The subsequent visible light irradiation induces significant differences on the degradation performance of the different mats (Figure 3.12 (a,b)). The CA/CeNPs mat which exhibits low photocatalytic activity ~29%, is notably improved when the CeNPs are grown in the presence of the PtNCs, reaching ~70% for CA/CeNPs/Pt5 and ~60% for CA/CeNPs/Pt1 respectively. This is attributed to the enhanced photocatalytic response of the CeNPs/Pt to the visible light irradiation in combination with the prolonged time of interaction between the dye and the composites, which optimizes the interactions (e.g. adsorption and diffusion) of the organic molecules with the composite mats. [25,26]

When the interaction of the mats with the dye is adjusted to 1 hour under dark, less dye molecules are interacting with the mats, resulting in adsorption efficiencies of ~4% for neat CA fibers mats and CA/CeNPs, ~6% for CA/CeNPs/Pt1, and ~10% for CA/CeNPs/Pt5, respectively, see Figure 3.13 (a). Moreover, the trend of the degradation performance is quite similar also in this case, with the CA/CeNPs/Pt5 to show the best performance, with an efficiency of ~50%, while for CA/CeNPs/Pt1 and CA/CeNPs are ~43%, and ~36%, respectively.

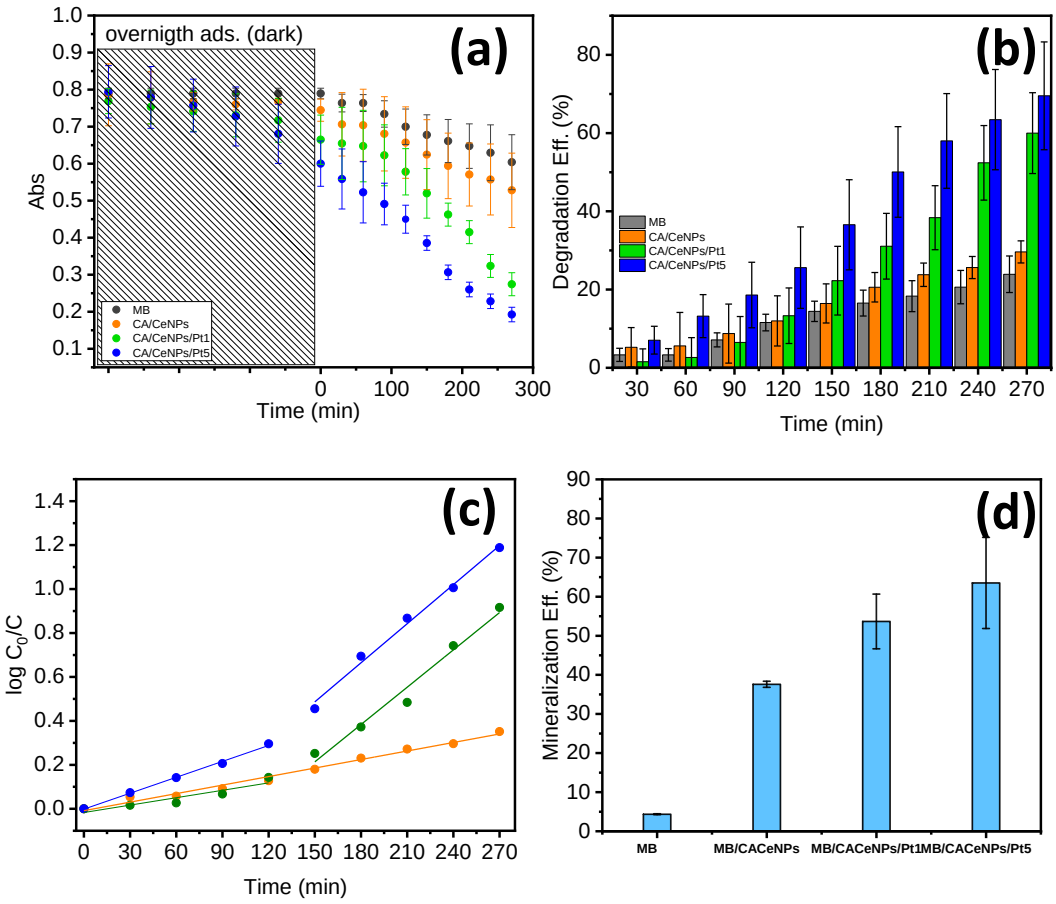

Figure 3.12. Photodegradation of MB under visible-light irradiation. (a) Time dependence of the absorbance at λ=664 nm. (b) Degradation efficiency (%) vs time of irradiation. (c) Fitting of the pseudo first-order kinetic model to the experimental data. (d) MB mineralization efficiency (%) of the MB after the photodegradation process for the different samples. For comparison, the value of the MB solution without any mat and under the same irradiation conditions is also presented.

The MB degradation kinetics shown in Figure 3.12 (c), after the overnight dark contact, reveals a distinct behavior depending on the presence of the Pt NPs. For CA/CeNPs, the ln (C_0/C) increases linearly with time (with a kinetics rate constant (k) obtained from eq.3.2 k==1.3 10^{-3} min^{-1}. When Pt NPs are present, two different trends emerge. The kinetics rates change from k=0.7 10^{-3} min^{-1} and k=2.4 10^{-3} min^{-1} in the first two hours to k=4.7 10^{-3} min^{-1} and k=6.0 10^{-3} min^{-1} for the CA/CeNPs/Pt1 and the CA/CeNPs/Pt5, respectively (further details in Table 3.3). This can be attributed to the fact that in the first minutes, the

photocatalytic process is mainly focused on the bleaching of the MB adsorbed on the mats, and therefore the MB concentration in the liquid is changing slowly.[27,28] When the MB is photodegraded, the photocatalytic process accelerates and the MB in solution is rapidly destroyed due to the favorable interaction between the dye molecules and the photocatalysts.[29]

Table 3.3. Rate constant of photodegradation process under visible irradiation of all fiber mats at different time contact with MB dye.

Time contact in dark	**CA/CeNPs**	**CA/CeNPs/Pt 1**	**CA/CeNPs/Pt 5**
	***k* (min^{-1})**	***k* (min^{-1})**	***k* (min^{-1})**
Overnight	$1.3\ 10^{-3}$	$0.7\ 10^{-3}$	$2.4\ 10^{-3}$
		R^2=0.82	R^2=0.99
		$4.7\ 10^{-3}$	$5.9\ 10^{-3}$
R^2	0.99	0.98	0.99
1 hours	$1.6 \cdot 10^{-3}$	$1.9 \cdot 10^{-3}$	$2.4 \cdot 10^{-3}$
R^2	0.99	0.99	0.99

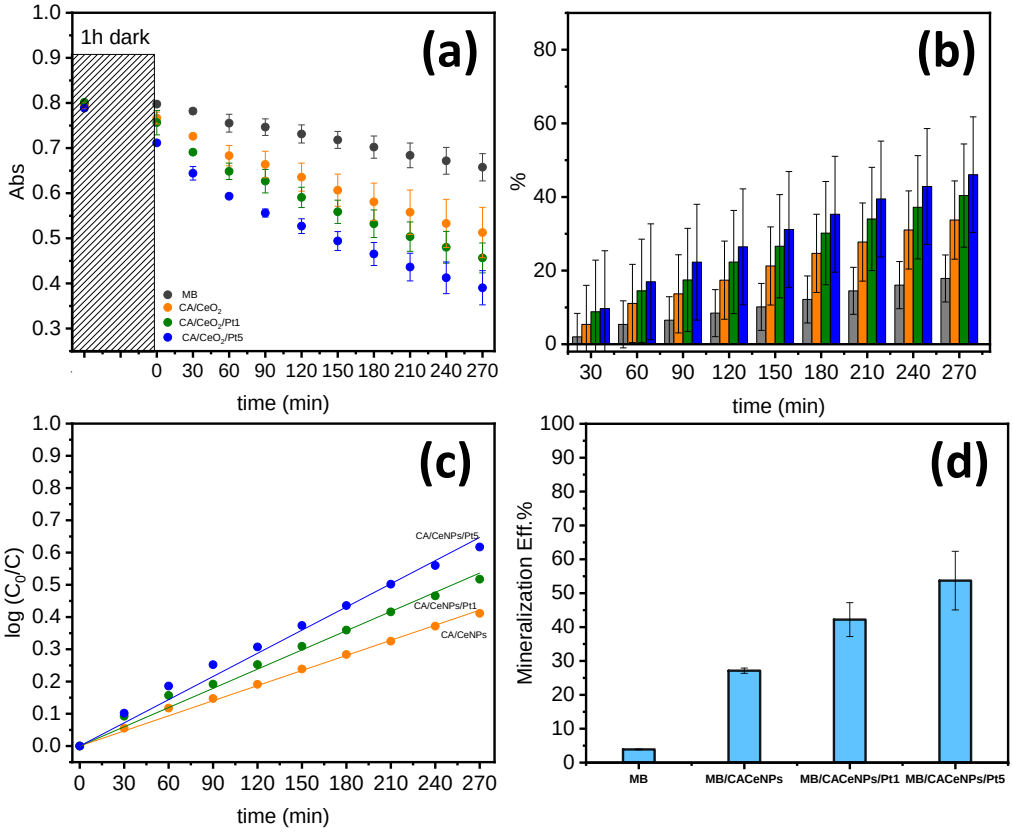

Figure 3.13. Photodegradation of MB under visible-light irradiation (1h dark condition). (a) Time dependence of the absorbance at λ=664 nm. (b) Degradation efficiency (%) vs time of irradiation. (c) Fitting of the pseudo first-order kinetic model to the experimental data. (d) MB mineralization efficiency (%) of the MB after the photodegradation process for the different samples. For comparison, the value of the MB solution without any mat and under the same irradiation conditions is also presented

The role of the adsorption process is evidenced by the photocatalytic kinetics at the mats stored for 1 hour under dark, see Figure 3.12 (c), where the slight decrease of the initial MB concentration indicates lower adsorption. The visible light induced decrease of the MB concentration is linear (eq. 3.2) for all cases in the entire time scale, proving that the rate change observed after the overnight storage is indeed due to the different dark storage time. The previous reaction rate trend is maintained also in this case, being faster ($2.4\ 10^{-3}$ min^{-1}) for the CA/CeNPs/Pt5 than that of CA/CeNPs/Pt1 and CA/CeNPs ($1.9\ 10^{-3}$ min^{-1} and

1.6 10^{-3} min^{-1}, respectively, see Table 3.3. It is worth noting that although in the case of CA/CeNPs the difference in the kinetics rate is not so pronounced possibly due to its low photo reactivity under visible light, in the case of the CA/CeNPs/Pt mats the rate is significantly higher when they are stored overnight (second step rate). This could be attributed to the optimized interaction between the dye and the mats surface due to the prolonged contact, but also due to the lower concentration of the MB molecules in the solution due to the adsorption step, which permits the more efficient interaction of the light with the photocatalyst, as the solution is more transparent. Overall, it can be concluded that the PtNCs presence on the surface of the mats improves the visible-light photo reactivity, with a better photocatalytic performance for higher Pt concentration.

Finally, the MB mineralization efficiency into CO_2, H_2O, ions and some mineral acids is calculated using eq. (3.3). Figure 3.12 (d) shows that MB mineralization efficiencies obtained for the CA/CeNPs/Pt5 mats (~63%), and CA/CeNPs/Pt1 mats (~53%) are significantly higher than the one obtained for CA/CeNPs mats (~37%). A similar trend is observed when the mats are left in dark for 1h, as reported in the Figure 3.13 (d), where the mineralization efficiency reached 52% the CA/CeNPs/Pt5 mats and 42% CA/CeNPs/Pt1 mats and 27% for CA/CeNPs mats.

3.7 Reactive oxygen species (ROS) identification

The photocatalytic effect is stemming from the redox reactions caused by photoinduced charge carriers (e^-/h^+) exploited in the formation on the surface of the photocatalysts of reactive oxygen species (ROS), such as superoxide anion radicals, hydrogen peroxide,

singlet oxygen and •OH.[30] Although •OH are the main actors in the mineralization mechanism of persistent organic pollutants, it is also important to consider the formation of oxygen superoxide and singlet oxygen species. Moreover, the different photocatalytic activities strongly depend on the kinetics of formation of each ROS.

We evaluated the •OH formation during the photocatalytic process from the FL fluorescence quenching, considering the eq 3.4 and using the fluorescein as probe molecules for this porpoise.

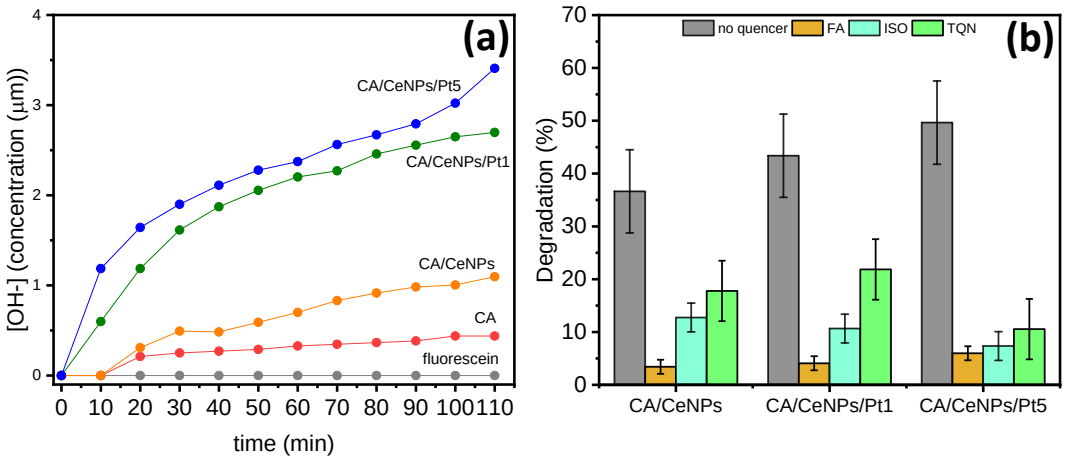

Figure 3.14. (a) Formation of •OH in the MB solution with FL solution (8µL) without any photocalyst, and by the presence of neat CA mats (red dots), CA/CeNPs (orange dots), CA/CeNPs/Pt1 (blue dots) and CA/CeNPs/Pt5 (green dots). (b) Trapping experiment of active species during the MB photodegradation under visible irradiation (λ > 400 nm) of the, CA/CeNPs, CA/CeNPsPt1, and CA/CeNPsPt5 mats (0.4 mg mL-1). FA, ISO, and CQN are used to indicate formic acid, isopropyl alcohol, and thymoquinone quenchers, respectively.

As shown in Figure 3.14 (a) the time-dependent •OH formation during the visible light irradiation is higher for the CA/CeNPs/Pt5 mats, followed by the CA/CeNPs/Pt1 and then by the CA/CeNPs mats. This confirms the higher responsivity of the Pt loaded mats to the visible light irradiation, in agreement with the photodegradation process trend of MB.

The •OH may be formed by a) reactions of photogenerated holes or electrons with the water adsorbed on the mat surface or with hydroxyl ions; b) reactions of protons with superoxide radicals; c) photolysis of water, which can be excluded in our case, as it may happen only upon UV light irradiation.[31]

To determine the role of the superoxide radicals, of the photogenerated holes and of the •OH to the photodegradation process, trapping experiments of the active species during the MB photocatalytic degradation have been performed adding scavengers in the MB aqueous solution: Formic acid (FA) to trap the photogenerated holes, thymoquinone (TQN) for trapping the superoxide radicals and isopropyl alcohol (ISO) for the •OH. As shown in Figure 3.14 (b), the photodegradation efficiency of the mats is significantly decreased in the presence of the scavengers compared to the degradation efficiency of the hybrid mats in the same experimental conditions.[30,31]

This behavior demonstrates that the dominant factor during the photodegradation process is the holes formation. However, for the CA/CeNPs/Pt5 mats, there is also a notable contribution of the hydroxyl (ISO quencher) and superoxide radicals (TQN quencher). Therefore, the good photocatalytic activity of the CA/CeNPs/Pt5 mats under visible light irradiation can be attributed to the greater number of photogenerated holes, hydroxyl and superoxide radicals and to the higher rate of their production. This can be attributed to the improved light trapping efficiency given by the combination of CeNPs and PtNCs in the surface of the mats, which causes an electronic modification of the interfaces with a substantial reduction of the bandgap energy and the efficient separation of electron-hole

pairs, which are able to trap holes and to produce the $^{\bullet}OH$ on the surface of the CeNPs/PtNCs.

3.8 Conclusions

In this Chapter, we report an innovative and versatile route for the preparation of polymer-based mats decorated with ceria nanoparticles and platinum nanoclusters for photocatalytic applications. In particular, the most relevant results of this study are:

- The possibility to obtain composite nanostructures on fibrous membranes upon the combination of the in-situ technique for the growth of CeNPs in the whole volume of mats and the use of Supersonic Cluster Beam Deposition to deposit directly on the surface of the mats the Pt nanoclusters. This fabrication method avoids the use of chemical reagents for the synthesis of the nanostructured materials in the final nanocomposites.
- The thermally induced solid-state reaction in the mats results in the nucleation and growth of CeNPs in contact with the deposited PtNCs.
- The presence of Ce^{3+}/Ce^{4+} and of the oxygen defects in combination with the PtNCs result in a material with good photocatalytic properties under visible light irradiation as proved by the study on the photocatalytic degradation of MB, which reached 70% of efficiency.
- The combination of PtNCs and CeNPs is responsible for the effective photocatalytic performance of the mats, due to the formation of oxygen vacancies on the surface due to the presence of mixed ceria nanoparticles with different

oxidation states (3+ and 4+). Also, the presence of noble PtNCs on the surface of the mats which are close in contact with the ceria nanoparticles, are able to reduce the band-gap of the final mats..

- The detection of ROS species clarify the role of these species during the photodegradation process, showing that the formation of super hydroxyl radicals and holes are the mainly responsible of the photocatalytic degradation of MB .

3.9 References

(1) Costantino, F.; Cavaliere, E.; Gavioli, L.; Carzino, R.; Leoncino, L.; Brescia, R.; Athanassiou, A.; Fragouli, D. Photocatalytic Activity of Cellulose Acetate Nanoceria/Pt Hybrid Mats Driven by Visible Light Irradiation. *Polymers* **2021**, *13* (6), 912. https://doi.org/10.3390/polym13060912.

(2) Anastasescu, C.; Negrila, C.; Angelescu, D. G.; Atkinson, I.; Anastasescu, M.; Spataru, N.; Zaharescu, M.; Balint, I. Particularities of Photocatalysis and Formation of Reactive Oxygen Species on Insulators and Semiconductors: Cases of SiO_2, TiO_2 and Their Composite SiO_2–TiO_2. *Catal. Sci. Technol.* **2018**, *8* (21), 5657–5668. https://doi.org/10.1039/C8CY00991K.

(3) Chatterjee, D.; Dasgupta, S. Visible Light Induced Photocatalytic Degradation of Organic Pollutants. *Journal of Photochemistry and Photobiology C: Photochemistry Reviews* **2005**, *6* (2–3), 186–205. https://doi.org/10.1016/j.jphotochemrev.2005.09.001.

(4) Kamat, P. V. Photophysical, Photochemical and Photocatalytic Aspects of Metal Nanoparticles. *J. Phys. Chem. B* **2002**, *106* (32), 7729–7744. https://doi.org/10.1021/jp0209289.

(5) Wang, P.; Huang, B.; Dai, Y.; Whangbo, M.-H. Plasmonic Photocatalysts: Harvesting Visible Light with Noble Metal Nanoparticles. *Phys. Chem. Chem. Phys.* **2012**, *14* (28), 9813. https://doi.org/10.1039/c2cp40823f.

(6) Morselli, D.; Campagnolo, L.; Prato, M.; Papadopoulou, E. L.; Scarpellini, A.; Athanassiou, A.; Fragouli, D. Ceria/Gold Nanoparticles in Situ Synthesized on Polymeric Membranes with Enhanced Photocatalytic and Radical Scavenging Activity. *ACS Applied Nano Materials* **2018**, *1* (10), 5601–5611. https://doi.org/10.1021/acsanm.8b01227.

(7) Daelman, N.; Capdevila-Cortada, M.; López, N. Dynamic Charge and Oxidation State of Pt/CeO2 Single-Atom Catalysts. *Nat. Mater.* **2019**, *18* (11), 1215–1221. https://doi.org/10.1038/s41563-019-0444-y.

(8) Paparazzo, E. Use and Mis-Use of x-Ray Photoemission Spectroscopy Ce3d Spectra of Ce_2O_3 and CeO_2. *J. Phys.: Condens. Matter* **2018**, *30* (34), 343003. https://doi.org/10.1088/1361-648X/aad248.

(9) Ansari, S. A.; Khan, M. M.; Ansari, M. O.; Kalathil, S.; Lee, J.; Cho, M. H. Band Gap Engineering of CeO_2 Nanostructure Using an Electrochemically Active Biofilm for Visible Light Applications. *RSC Adv.* **2014**, *4* (32), 16782–16791. https://doi.org/10.1039/C4RA00861H.

(10) Qi, L.; Yu, Q.; Dai, Y.; Tang, C.; Liu, L.; Zhang, H.; Gao, F.; Dong, L.; Chen, Y. Influence of Cerium Precursors on the Structure and Reducibility of Mesoporous CuO-CeO2 Catalysts for CO Oxidation. *Applied Catalysis B: Environmental* **2012**, *119–120*, 308–320. https://doi.org/10.1016/j.apcatb.2012.02.029.

(11) Romanchenko, A.; Likhatski, M.; Mikhlin, Y. X-Ray Photoelectron Spectroscopy (XPS) Study of the Products Formed on Sulfide Minerals Upon the Interaction with Aqueous Platinum (IV) Chloride Complexes. *Minerals* **2018**, *8* (12), 578. https://doi.org/10.3390/min8120578.

(12) Manwar, N. R.; Chilkalwar, A. A.; Nanda, K. K.; Chaudhary, Y. S.; Subrt, J.; Rayalu, S. S.; Labhsetwar, N. K. Ceria Supported Pt/PtO-Nanostructures: Efficient Photocatalyst for Sacrificial Donor Assisted Hydrogen Generation under Visible-NIR Light Irradiation. *ACS Sustainable Chem. Eng.* **2016**, *4* (4), 2323–2332. https://doi.org/10.1021/acssuschemeng.5b01789.

(13) Calvache-Muñoz, J.; Prado, F. A.; Tirado, L.; Daza-Gomez, L. C.; Cuervo-Ochoa, G.; Calambas, H. L.; Rodríguez-Páez, J. E. Structural and Optical Properties of CeO2 Nanoparticles Synthesized by Modified Polymer Complex Method. *J Inorg Organomet Polym* **2019**, *29* (3), 813–826. https://doi.org/10.1007/s10904-018-01056-1.

(14) Agarwal, U. P. Analysis of Cellulose and Lignocellulose Materials by Raman Spectroscopy: A Review of the Current Status. *Molecules* **2019**, *24* (9), 1659. https://doi.org/10.3390/molecules24091659.

(15) Fischer, S.; Schenzel, K.; Fischer, K.; Diepenbrock, W. Applications of FT Raman Spectroscopy and Micro Spectroscopy Characterizing Cellulose and Cellulosic Biomaterials. *Macromolecular Symposia* **2005**, *223* (1), 41–56. https://doi.org/10.1002/masy.200550503.

(16) Sartoretti, E.; Novara, C.; Giorgis, F.; Piumetti, M.; Bensaid, S.; Russo, N.; Fino, D. In Situ Raman Analyses of the Soot Oxidation Reaction over Nanostructured Ceria-Based Catalysts. *Sci Rep* **2019**, *9* (1), 3875. https://doi.org/10.1038/s41598-019-39105-5.

(17) Kosacki, I.; Suzuki, T.; Anderson, H. U.; Colomban, P. Raman Scattering and Lattice Defects in Nanocrystalline CeO2 Thin Films. *Solid State Ionics* **2002**, *149* (1), 99–105. https://doi.org/10.1016/S0167-2738(02)00104-2.

(18) Xu, Y.; Wang, F.; Liu, X.; Liu, Y.; Luo, M.; Teng, B.; Fan, M.; Liu, X. Resolving a Decade-Long Question of Oxygen Defects in Raman Spectra of Ceria-Based Catalysts at Atomic Level. *J. Phys. Chem. C* **2019**, *123* (31), 18889–18894. https://doi.org/10.1021/acs.jpcc.9b00633.

(19) McBride, J. R.; Graham, G. W.; Peters, C. R.; Weber, W. H. Growth and Characterization of Reactively Sputtered Thin-film Platinum Oxides. *Journal of Applied Physics* **1991**, *69* (3), 1596–1604. https://doi.org/10.1063/1.347255.

(20) Derevyannikova, E. A.; Kardash, T. Y.; Stadnichenko, A. I.; Stonkus, O. A.; Slavinskaya, E. M.; Svetlichnyi, V. A.; Boronin, A. I. Structural Insight into Strong Pt–CeO_2 Interaction: From Single Pt Atoms to PtO_x Clusters. *J. Phys. Chem. C* **2019**, *123* (2), 1320–1334. https://doi.org/10.1021/acs.jpcc.8b11009.

(21) López, R.; Gómez, R. Band-Gap Energy Estimation from Diffuse Reflectance Measurements on Sol–Gel and Commercial TiO2: A Comparative Study. *J Sol-Gel Sci Technol* **2012**, *61* (1), 1–7. https://doi.org/10.1007/s10971-011-2582-9.

(22) Khan, M. E.; Khan, M. M.; Cho, M. H. Ce3+-Ion, Surface Oxygen Vacancy, and Visible Light-Induced Photocatalytic Dye Degradation and Photocapacitive Performance of CeO2-Graphene Nanostructures. *Sci Rep* **2017**, *7* (1), 5928. https://doi.org/10.1038/s41598-017-06139-6.

(23) Bruix, A.; Migani, A.; Vayssilov, G. N.; Neyman, K. M.; Libuda, J.; Illas, F. Effects of Deposited Pt Particles on the Reducibility of CeO2(111). *Phys. Chem. Chem. Phys.* **2011**, *13* (23), 11384. https://doi.org/10.1039/c1cp20950g.
(24) Tao, L.; Shi, Y.; Huang, Y.-C.; Chen, R.; Zhang, Y.; Huo, J.; Zou, Y.; Yu, G.; Luo, J.; Dong, C.-L.; Wang, S. Interface Engineering of Pt and CeO2 Nanorods with Unique Interaction for Methanol Oxidation. *Nano Energy* **2018**, *53*, 604–612. https://doi.org/10.1016/j.nanoen.2018.09.013.
(25) Chiu, Y.-H.; Chang, T.-F. M.; Chen, C.-Y.; Sone, M.; Hsu, Y.-J. Mechanistic Insights into Photodegradation of Organic Dyes Using Heterostructure Photocatalysts. *Catalysts* **2019**, *9* (5), 430. https://doi.org/10.3390/catal9050430.
(26) Andronic, L.; Isac, L.; Cazan, C.; Enesca, A. Simultaneous Adsorption and Photocatalysis Processes Based on Ternary TiO2–CuxS–Fly Ash Hetero-Structures. *Applied Sciences* **2020**, *10* (22). https://doi.org/10.3390/app10228070.
(27) Houas, A. Photocatalytic Degradation Pathway of Methylene Blue in Water. *Applied Catalysis B: Environmental* **2001**, *31* (2), 145–157. https://doi.org/10.1016/S0926-3373(00)00276-9.
(28) Ummartyotin, S.; Pechyen, C. Role of ZnO on Nylon 6 Surface and the Photocatalytic Efficiency of Methylene Blue for Wastewater Treatment. *Colloid and Polymer Science* **2016**, *294* (7), 1217–1224. https://doi.org/10.1007/s00396-016-3881-z.
(29) Rauf, M. A.; Meetani, M. A.; Khaleel, A.; Ahmed, A. Photocatalytic Degradation of Methylene Blue Using a Mixed Catalyst and Product Analysis by LC/MS. *Chemical Engineering Journal* **2010**, *157* (2–3), 373–378. https://doi.org/10.1016/j.cej.2009.11.017.
(30) Nosaka, Y.; Nosaka, A. Y. Generation and Detection of Reactive Oxygen Species in Photocatalysis. *Chem. Rev.* **2017**, *117* (17), 11302–11336. https://doi.org/10.1021/acs.chemrev.7b00161.
(31) Ribao, P.; Corredor, J.; Rivero, M. J.; Ortiz, I. Role of Reactive Oxygen Species on the Activity of Noble Metal-Doped TiO2 Photocatalysts. *Journal of Hazardous Materials* **2019**, *372*, 45–51. https://doi.org/10.1016/j.jhazmat.2018.05.026.
(32) Tan, H. L.; Abdi, F. F.; Ng, Y. H. Heterogeneous Photocatalysts: An Overview of Classic and Modern Approaches for Optical, Electronic, and Charge Dynamics Evaluation. *Chem. Soc. Rev.* **2019**, *48* (5), 1255–1271. https://doi.org/10.1039/C8CS00882E.
(33) Hou, W.; Cronin, S. B. A Review of Surface Plasmon Resonance-Enhanced Photocatalysis. *Adv. Funct. Mater.* **2013**, *23* (13), 1612–1619. https://doi.org/10.1002/adfm.201202148.
(34) *Photocatalysis: Fundamentals and Perspectives*; Schneider, J., Bahnemann, D., Ye, J., Li Puma, G., Dionysiou, D. D., Eds.; Energy and Environment Series; The Royal Society of Chemistry, 2016. https://doi.org/10.1039/9781782622338.

CHAPTER 4: TRACKING THE ELECTRON FLOW IN THE PHOTOCATALYTIC ACTIVITY OF BIPOLAR PD/CDS MEMBRANE

ABSTRACT

In the present study, we aim to probe the photocatalytic activity of BPM loaded with CdS and Pd nanostructured to promote the photodegradation of contaminants in water. Through the ion exchange property of a bipolar membrane (BPM) it is possible to load the CdS photocatalyst on one side and Pd electrocatalyst on the other side. By inserting the photocatalytic BPM-CdS/Pd membrane between the two compartments of an H-cell, we can separate the reduction and oxidation processes. Following visible light excitation of CdS in the BPM-CdS/Pd membrane we can induce vectorial electron transfer from CdS to Pd and to an electron acceptor (4-nitrophenol). The holes generated at CdS are scavenged by ethanol or 4-chlorophenol. The photocatalytic reduction rate dependence on the Pd loading in the membrane as well as its effect on modulating the rates of electron and hole transfer processes are discussed. The design of a semiconductor and metal loaded membrane paves the way for improving selectivity and efficiency of photocatalytic processes.

This Chapter is based on: Costantino Federica, Luca Gavioli, and Prashant V. Kamat. "A Bipolar CdS/Pd Photocatalytic Membrane for Selective Segregation of Reduction and Oxidation Processes." *ACS Physical Chemistry Au* (2021).[1]

4.1 Introduction

Oxidation/reduction reactions employing hybrid nanostructures play a key role in emerging energy technologies as well as photocatalytic remediation of water pollutions.[2–6] The effective removal of toxic industrial chemicals such as organophosphates, sulfur mustards, nitro aromatics and dyes from wastewater runoff or accidental discharge is of vital importance. Due to the high health hazards at very low levels, their effective removal remains difficult but it is necessary for the entire eco-system considering the water scarcity. Recently, bipolar membrane (BPM) have attracted renewed interest and attention for electrochemical and photocatalytic application in water splitting and CO_2 reduction.[7] BPM are polymeric membranes composed of two layers, a negatively charged cationic-exchange layer (CEL) and a positively charged anion-exchange layer (AEL).[7,8] The interface between CEL and AEL is referred to as the "interfacial layer" or junction.[7,8] In contrast to the conventional "monopolar" membrane (IEMs), consisted of one charged polymeric layer for example Nafion ®, bipolar membrane are not meant to have any ion transport across them.[8] The main function of BPM is a disproportionation reaction: water can be electro or photo-dissociated into protons (H^+) and hydroxide (OH^-) ions at the bipolar junctions, with a pH difference as high as 10.[9]

Another interesting feature of the BPM is the ability to selectively exchange metal cations or anionic complexes.[10] For example, Cd^{2+} ions can be easily embedded into Nafion by simply immersing in aqueous solution, and then exposed to a sulfur (or selenide) source one can readily make CdS (or CdSe) nanoparticles.[10,11] This photocatalytically active membrane is used for photo production of H_2 during 1980.[12] Nonetheless in the monopolar

membrane it is possible to exchange only a cationic or anionic species while in the BPM offers the unique property to embed two different ions selectively in the AEL or CEL side and drive a photocatalytic reaction with a direct electron flow.[10,13,14]

In the present study, we aim to probe the BMP activity, gain mechanistic insight into the electron transfer between CEL and AEL, as well as create a photocatalytically active BMP assembly for increased 4-nitrobenzenethiol (4-NBT) degradation using a combination of two different types of nanoparticles (CdS/PdNPs). We furthered moved to take advantage of CEL and AEL layers to manipulate and optimize NPs growth for desired application in photocatalysis. By loading the BMP directly with catalyst particles, we have been able to circumvent and address the challenges of heterogeneous catalysis. We investigate the effect of different PdNPs amount on the CdS growth and on the properties of the BMP under visible light irradiation. We evaluate the photocatalytic degradation of 4-NP to 4-ammino phenol (4-AP) via light-induced electron transfer cascade across the CEL/AEL junction using ethanol and 4-chloro phenol as electron acceptor. Taking the advantage of localized surface plasmon from these hybrid nanostructures, we have established an efficient electron transfer cascade for the photocatalytic degradation of phenol compounds in water.

4.2 Materials and Method

4.2.1 Chemicals

Sodium Chloride (NaCl, >99%), Sodium Azide (NaN_3, >99%), Methyl Viologen dichloride (MV^{2+}, 98%), 4-nitrophenol (4-NP, 99%) and 4-chlorophenol (4-CP, 99%) were purchased form Sigma Aldrich and used without purification. Ethanol (CH_3CH_2OH, 99%)

was purchased from Kopatec. Thioacetamide (C_2H_5NS, TAA 99.4%) and Cadmium Nitrate tetrahydrate ($Cd(NO_3)_2 \cdot 4H_2O$, 99.99%) and Tetra-ammine palladium chloride ($Pd(NH_3)_4Cl_2$, >99%), were purchased from Fisher Scientific. Bipolar membrane (BPM, PEEK supported) was purchased from Fuel Cell Store.

4.2.2 Characterization Methods

Absorption spectra were recorded using a Varian Cary 50 Bio UV-Visible spectrometer. Pulse Voltammetry were performed using Gamry PCI 4750 in two-electrode cell setup, using a Pt foil as a working electrode and Ag wire as a reference electrode. A 300 W Oriel Xenon Lamp was used as a light source along with a water filter (13 cm length) to remove infrared contributions. Long-pass filters were used for the different irradiations experiments to select the desired wavelength in the visible region

4.3 Fabrication of BPM-CdS

Bipolar membrane (initially soaked in 1M NaCl, 100 ppm NaN_3 to exchange Na^+ ions) was cut in small pieces (2cm x $2cm^2$). The film immersed in DI water was sonicated for 30 minutes and then copiously cleaned with DI water. The BPM was soaked in 0.5M $Cd(NO_3)_2$ solution for 10 hours to allow the adsorption of Cd^{2+} ions inside the pores of cation exchange layer (CEL) side BPM. The membrane was rinsed with DI water and placed between the two compartments of the H-cell along with O-ring seals and clamps. The compartment facing CEL side of BPM was filled with 3 mL of TAA (0.5 M), while the AEL side was kept empty. The H-Cell was placed in a preheated water bath at 90°C for 1 hour. At this temperature, TAA dissociates to produce H_2S gas resulting in the

formation of CdS, as reported in our previous study. See the Scheme 4 to view the insight of these synthetic steps (1-4).

4.3.1 Fabrication of BPM-CdS/Pd

The BPM/CdS membrane was thoroughly washed with water to remove any adsorbed ions in the surface. The BPM/CdS was inserted in the middle of the H-Cell, the AEL side was exposed to 0.01 M solution of $Pd(NH_3)_4Cl_2 \cdot H_2O$ The dissolved Pd(II) complex species can have various analogues including negatively charged species such as $[PdCl(NH_3)OH]^-$.[15] The adsorption time was varied starting from 5 minute to 120 minutes to achieve different loadings loading in the AEL layer. The BPM/CdS/Pd(II) film was washed with DI water to remove any adsorbed ions in the outside surface of the membrane, and inserted in the H-Cell. The CEL side of compartment of the H-Cell contained ethanol while the AEL compartment water. Solutions were purged with N_2 for 30 min. The CEL side of the H-cell was irradiated for 60 min with Xenon lamp, using a cut-off filter (λ>390 nm) in order to promote the growth of Pd in the AEL side of the membrane. See the Scheme 4 to view the insight of these synthetic steps (5-8).

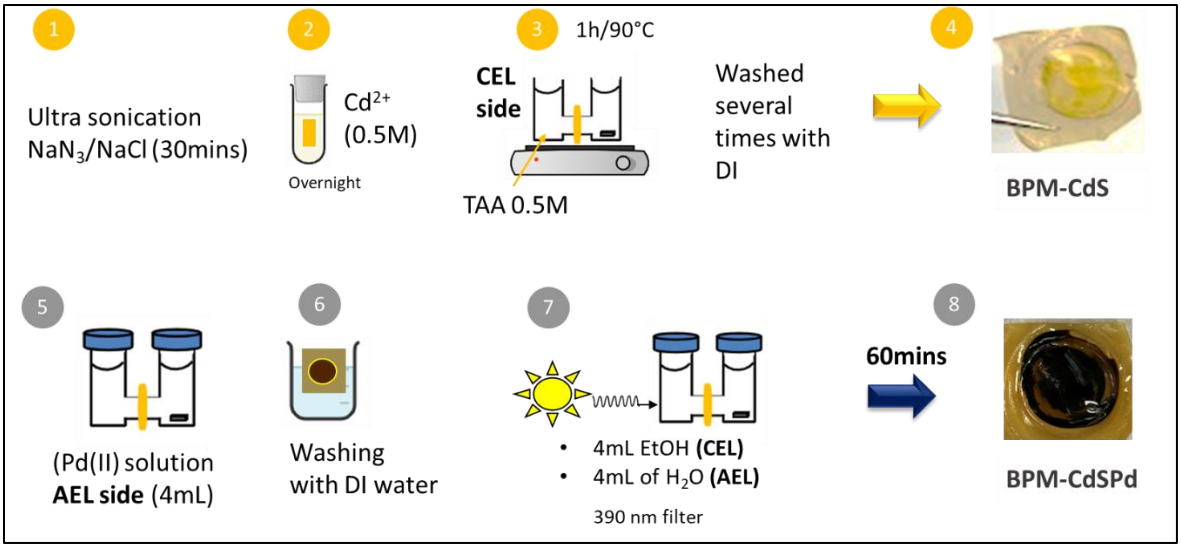

Scheme 4. Synthetic steps involved in preparing photocatalytic bipolar membrane. The schematic diagram illustrates key steps of loading CdS photocatalyst in the CEL side (Steps 1-4) and Pd electro catalysts on the AEL side (Steps 5-8) of the bipolar membrane.

4.4 Photocatalytic Experiments using BPM-CdS/Pd

The photocatalytic activity of BPM-CdS/Pd membrane was monitored by measuring the change in solution absorbance upon irradiation of the H-Cell. The BPM-CdS/Pd membrane was introduced between the arms of the cell. Solutions of probe molecules, such as Methyl Viologen (MV^{2+}), 4-Nitrophenol (NP) and 4-Chlorophenol (CP) were employed to establish the photo activity of the membrane.

The rate constant of the photodegradation process (k, min^{-1}) is calculated by fitting the experimental data with the pseudo-first order kinetics model expressed in the equation:

$$ln\ \frac{A_0}{A} = kt, \qquad (4.1)$$

Where A_0 is the initial concentration of the probe species and A is the concentration of the solutions at time t during the photocatalytic process.

The degradation efficiency (%) is calculated using the following equation:

Degradation efficiency $(\%) = \frac{C_0 - C}{C_0} \times 100\ \%$ (4.2)

4.4.1 Reduction of Methyl Viologen

BPM-CdS/Pd was introduced in the H-Cell with 4 mL of 1 mM of MV^{2+} in the AEL side and 4 mL of EtOH in the CEL side as hole scavengers. The cell compartments were closed with the septa to avoid the presence of oxygen and moisture during the photocatalytic process. The solutions were purged with N_2 for 30 minutes. The cell was irradiated with visible light, using a 300W Xe-lamp placed 30 cm away from the sample. A water layer and a cut-off filter (λ> 390 nm) was placed between the cell and the light source. The area of the BPM-CdS/Pd exposed to light was (0.785 cm^2) The absorbance spectra of the solution were recorded periodically to monitor the formation of $MV^{+\bullet}$ species for all samples.

4.4.2 Oxidation of 4-Nitro Phenol

BPM-CdS/Pd was introduced in the H-Cell with 4 mL of 25 μM 4NP (water solution) in the AEL side of the cell, the pH of the solution was adjusted to 10 adding 0.2μL of NaOH (0.2 M). The CEL side is filled with 4 mL of EtOH/water (3:1). The cell was clamped and the solution was purged for 30 minutes with N_2. The cell was irradiated with a visible light as mentioned above. The absorption spectra were recorded periodically to monitor the degradation of nitrophenol species and the formation of aminophenol in solution species for all samples.

4.4.3 Simultaneous Oxidation and reduction of 4-Chlorophenol and 4-Nitrophenol

BPM-CdS/Pd was introduced in the H-Cell, the CEL side of the cell is filled up with 4 mL of 4-CP 30 μM in water, while the AEL side is filled with 4 mL of 30 μM 4NP (pH 10). The cell compartments were closed with the septa, clamped and purged for 30 min with N_2. The CdS in the membrane was excited with the visible light (λ>390 nm). The absorption spectra were recorded periodically to monitor the degradation of chlorophenol (CEL side) and the oxidation of nitro phenol (AEL side).

4.5 Results and Discussion

4.5.1 Morphological characterization of BPM-CdS/Pd

By taking the advantage of the different charge on the AEL and CEL side of BPM it is possible to load selectively different metal salt. Presently the BPM is loaded with Cd^{2+} in the cation exchange layer (CEL) and Pd(II) in the anion exchange layer (AEL), as can be seen from the Scheme 4. The processes leading to the formation of CdS and Pd in the two parts of the BPM are expressed in reactions (4.3-4.4) and (4.5-4.6).

Part 1

$$CEL\text{-}Na^{+} + Cd^{2+} \longrightarrow CEL\text{-}Cd^{2+} \quad (4.3)$$

$$CEL\text{-}Cd^{2+} + TAA \longrightarrow \longrightarrow CEL\text{-}CdS \quad (4.4)$$

Part 2

$$AEL\text{-}Cl^{-} + Pd(II) \longrightarrow AEL\text{-}Pd(II) \quad (4.5)$$

$$AEL\text{-}Pd(II) + CEL\text{-}CdS\ (e) \longrightarrow \longrightarrow AEL\text{-}Pd^{0} + CEL\text{-}CdS \quad (4.6)$$

The formation of CdS in CEL and Pd in AEL can be seen through color changes as shown in the photographs of the membrane following two-step synthesis (Figure 4.1). The

changes in the absorption spectra are shown in Figures 4.2 (a) and 4.2 (c). The CdS nanoparticles formed within the pores of the membrane exhibit an absorption onset around 490 nm (or 2.53 eV), which is close to the bandgap energy of the bulk semiconductor (E_g= 2.42 eV).[16,17] Similarly, the formation of Pd in the AEL is marked by the broad absorption in the visible. Because of the strong absorption and scattering effects, the absorption spectra of Pd loaded film could not be analyzed. It is interesting to note that these spectral features confirm the loading of the semiconductor and metal nanoparticles within the pores of the membrane.

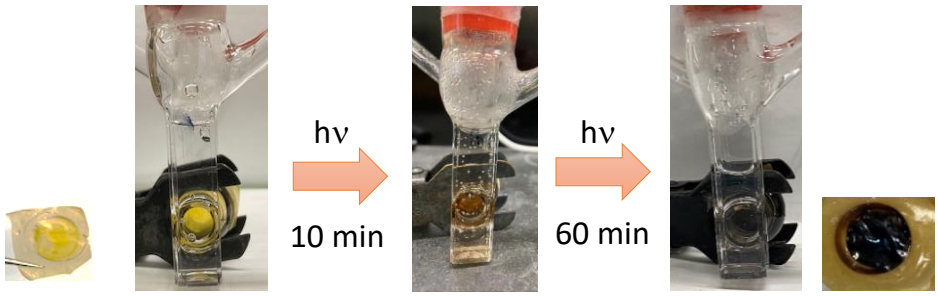

Figure 4.1. The color change of the BPM associated with the formation of CdS in the CEL (left), followed by 10 and 60 min irradiation to produce Pd nanoparticles in AEL (right).

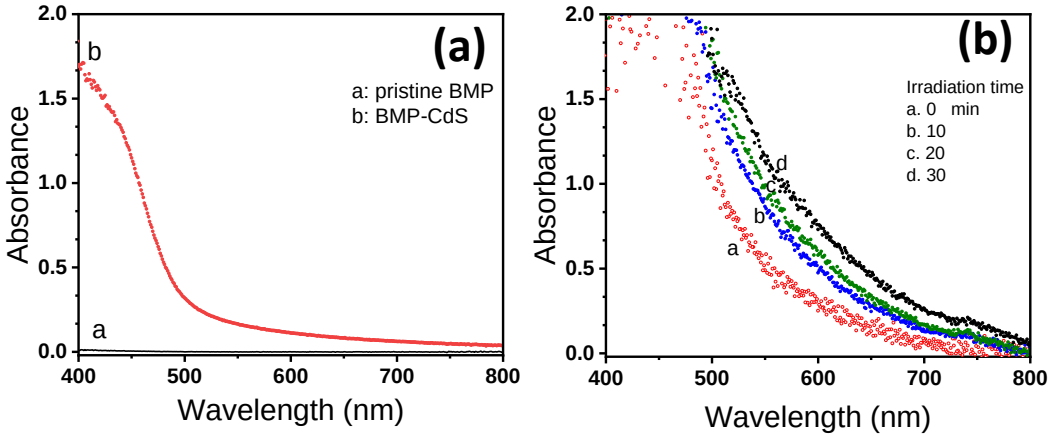

Figure 4.2. (a) Absorbance spectra of BPM-CdS following the exposure of Cd^{2+} loaded CEL layer to thioacetamide. (b) Absorbance spectra of BPM-CdS/Pd(II) recorded during the growth of

Pd nanoparticles in the AEL side. The CdS in the BPM was excited with visible light to provide photo-generated electrons for Pd reduction (with holes scavenged by ethanol in the H-cell).

The morphology of the BPM was investigated by SEM analysis, as can be seen from the Figure 4.3 (a-b), the cross section of the bare membrane clearly reveled the presence of the two different layer and even the junction of PEEK polymer.

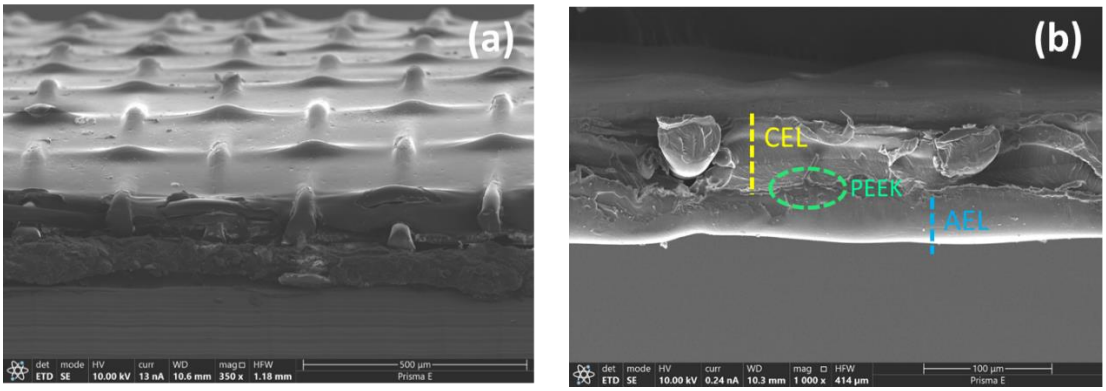

Figure 4.3. (a) Cross section of pristine BPM (scale bar: 500µm) and (b) high magnification analysis on BPM (scale bar: 100µm), Both CEL side (yellow dash line) and AEL side (blue dash line) can be detected from the figure, also the junction made of poly-ethyl ketone (PEEK) of the membrane is clearly observed (green circle).

Energy-d3ispersive X-ray spectroscopy (EDX) elemental mapping provided further insight into the BPM layers of BPM-CdS/Pd. Figure 4.4 (a) showed the cross sectional image of BPM-CdS/Pd. As shown in the Figure 4.4 (b), the region marked with green and yellow colors are associated with Cd and Pd species, in the CEL and AEL side of the membrane respectively. This indicating the existence of two oppositely charged ion in the different side of the membrane, as a result of the two different synthetic step to load the CdS and PdNPs in the BPM.

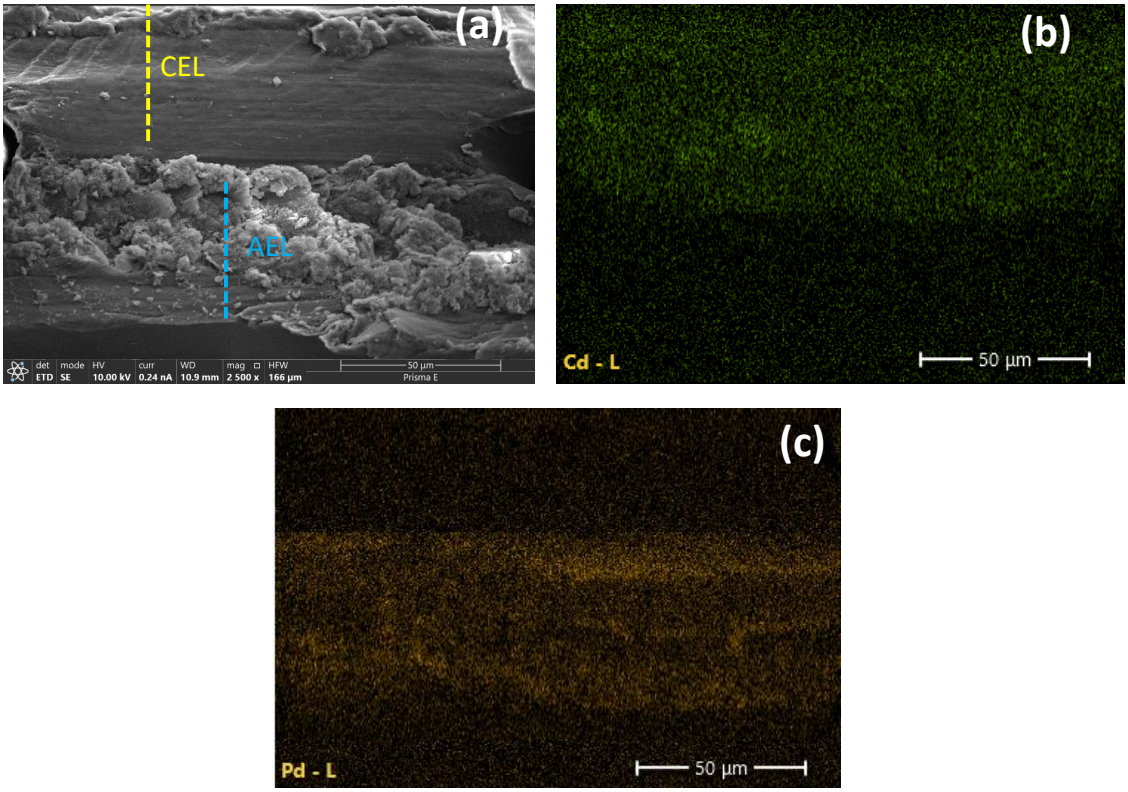

Figure 4.4. Cross-section of BPM-CdS/Pd (a) with higher magnification (scale bar: 50 µm) The EDX analysis confirmed the presence of Cd (top CEL part) and Pd (bottom AEL part) elements in the bipolar membrane (b-c).

A closer look on BMP-CdS/Pd showed the particle morphology, from Figure 4.5 (a) is possible to detected the presence of CdS nanostructure in the CEL layer consists of ~100 nm diameter (see the inset of the Figure 4.5 (a)). The Pd particles loaded in the AEL on the other hand exhibit both particle and rod like structures as can show in the Figure 4.5 (b). These images provide a glimpse of photocatalyst and Pd nanoparticles embedded in two separate layers of the bipolar membrane.

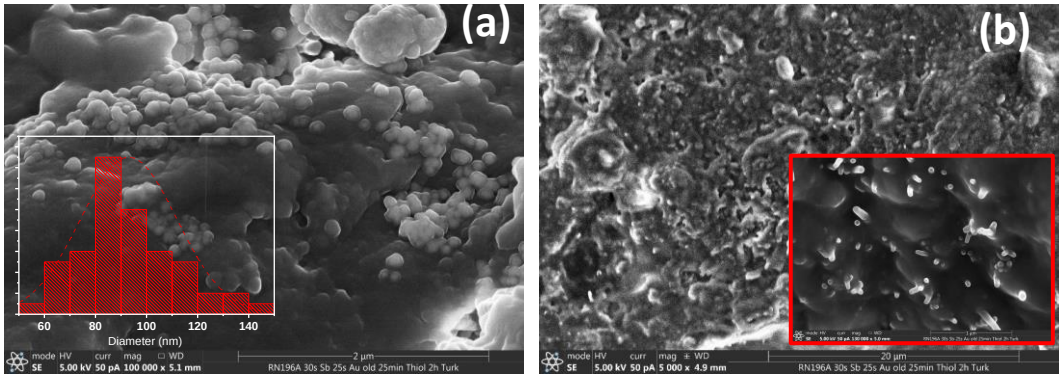

Figure 4.5. Cross sectional image of BPM-CdS/Pd membrane. (a) CdS nanoparticles in the CEL side of BPM (magnification is 2µm), the inset is related to the size distribution analysis. AEL layer loaded with Pd particles at two different magnifications.

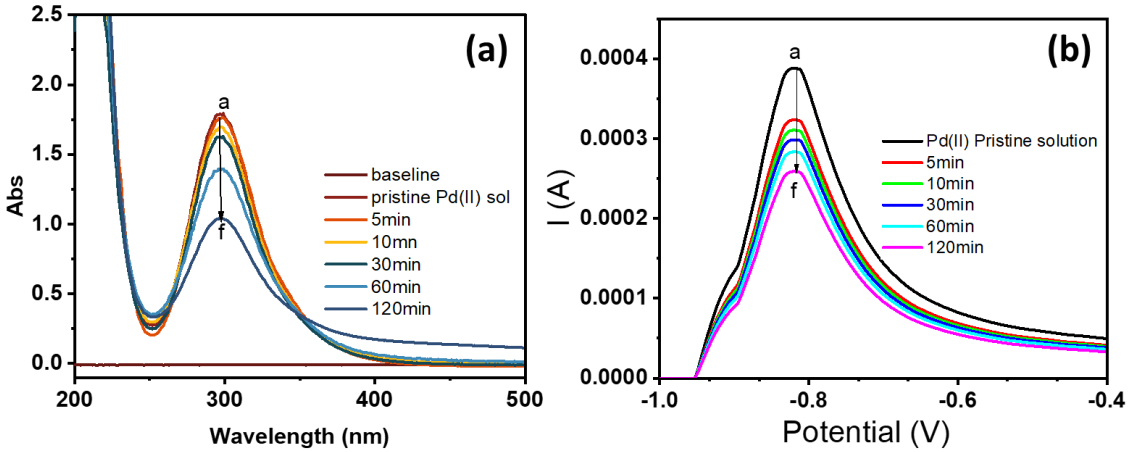

Figure 4.6. (a) absorbance spectrum of a $Pd(NH_3)_4Cl_2$ solutions starting from (a) pristine solution to (f) solution collected after 120 min in contact with the AEL side of the membrane. (b) Square wave voltammograms (SQWV) of $Pd(NH_3)_4Cl_2$ solution following the loading of the membrane; (a) pristine Pd(II) solution before soaking of BPM (b)-(f) after soaking of membrane (BPM-CdS) for different times.

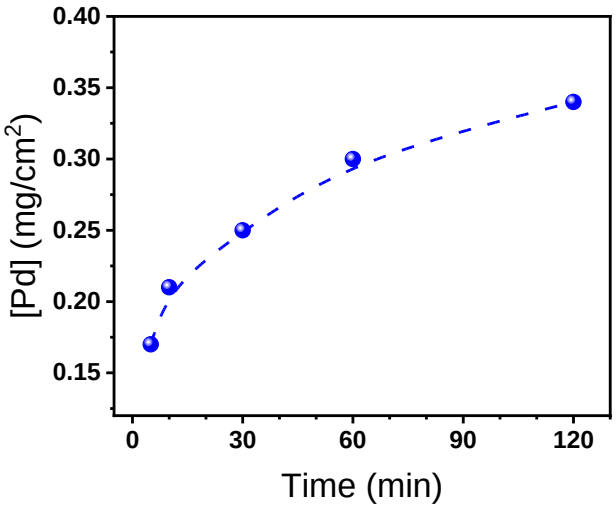

Figure 4.7. Total amount of Pd (mg/cm^2) estimated from the decreased peak in SQWV at different soaking times.

In order to optimize the photocatalytic membrane the concentration of Pd species is varied while the concentration of CdS is keep constant. The concentration was varied by soaking the CdS-loaded BPM in a $Pd(NH_3)_4Cl_2$ solution for several different times.

Table 4. Estimation of palladium quantity (mg/cm^2) in the membrane using square wave voltammetry

Soaking time	**ΔI (A)**	**ΔC (M)**	**Pd(II) moles/cm^2**	**Pd equivalent mg/cm^2**
5min	$6 \cdot 10^{-5}$	$1.6 \cdot 10^{-3}$	$6.4 \cdot 10^{-6}$	0.17
10min	$7.3 \cdot 10^{-5}$	$2 \cdot 10^{-3}$	$8 \cdot 10^{-6}$	0.21
30min	$8.4 \cdot 10^{-5}$	$2.3 \cdot 10^{-3}$	$9.3 \cdot 10^{-6}$	0.25
60min	$1 \cdot 10^{-4}$	$2.7 \cdot 10^{-3}$	$1.1 \cdot 10^{-5}$	0.30

120min	$1.2 \cdot 10^{-4}$	$3.3 \cdot 10^{-3}$	$1.3 \cdot 10^{-5}$	0.34

The loss of Pd(II) was monitored in solution to estimate the amount incorporated in the AEL. Pd(II) concentration in solution was monitored using absorption spectra and square wave voltammetry, see Figure 4.6 (a-b).

Considering the current (I) relating to the initial 0.01 M solution of $Pd(NH_3)_4Cl_2$ (trace a, Figure 4.6 (b)) was used to approximation and calculate the total amount of palladium in the surface of the membrane (assuming the current is proportional to the concentration). As Pd(II) gets incorporated into the film, the measured current decreases (traces b-f, Figure 4.6(b)) and that decrease can be related to the loading in the AEL side of the membrane. From the Figure 4.7 and from the Table 4, showed the different amount (mg/cm^2) which are loaded in the AEL side of the BPM.

4.6 Photocatalytic reduction of Methyl Viologen to optimize the Pd concentration

The photocatalytic activity was probed through with the reduction of methyl viologen in the AEL compartment of the H-cell. The BPM-CdS/Pd membrane was inserted in the middle of the H-cell separating the solutions in the CEL and AEL compartments. The arms of the cell were made from quartz cuvette, in order to monitored the changes in the absorption of the respective solution in each compartment. The photoexcitation was conducted through the CEL side so that CdS can be excited to induce the photocatalytic reaction. The area of the film exposed to light was 0.785 cm^2. As the ethanol in the CEL compartment scavenged the photogenerated holes, the transport of accumulated electrons

from CdS to the Pd nanoparticles embedded in AEL is facilitated. The MV^{2+} present in the AEL compartment captured these electrons to form the reduced methyl viologen cation radical ($MV^{+\bullet}$). Because of the positive charge for both MV^{2+} and $MV^{+\bullet}$, they remain in solution and are repelled by the AEL part of the membrane.

The followed reactions represent the reduction of MV^{2+} following the photoexcitation of CdS in the BPM-CdS/Pd membrane, in the CEL and AEL side of the fabricated BPM-CdS/Pd.

CEL

$$\text{BPM-CdS/Pd} + h\nu \longrightarrow \text{BPM-CdS(h—e)/Pd} \qquad (4.7)$$

$$\text{BPM-CdS(h—e)/Pd} + C_2H_5OH \longrightarrow \text{BPM-CdS(e)/Pd} + C_2H_5O^{\bullet} \qquad (4.8)$$

AEL

$$\text{BPM-CdS(e)/Pd} \longrightarrow \text{BPM-CdS/Pd(e)} \qquad (4.9)$$

$$\text{BPM-CdS/Pd(e)} + MV^{2+} \longrightarrow \text{BPM-CdS/Pd} + MV^{+\bullet} \qquad (4.10)$$

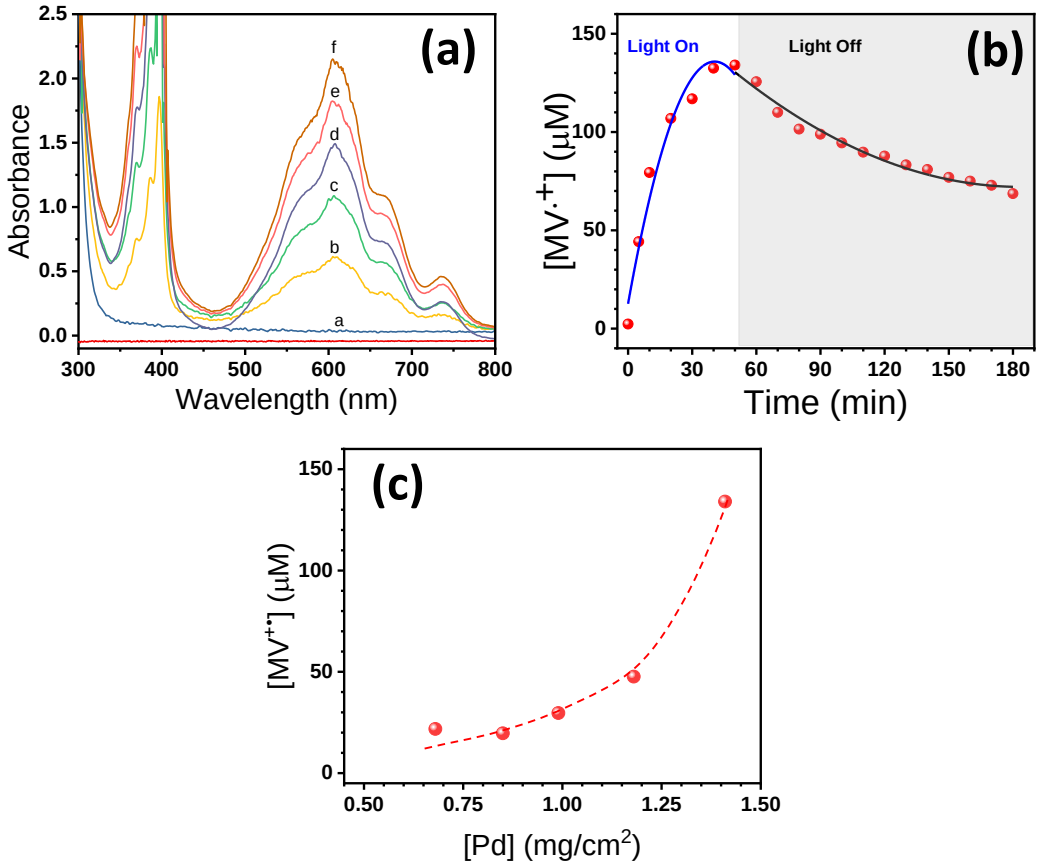

Figure 4.8. (a) Formation of $MV^{+\bullet}$ as monitored from the absorption spectra recorded during the excitation of BPM-CdS/Pd with visible light. Deaerated ethanol solution MV^{2+} (1mM) was employed in the AEL compartment. Pd loading in the BPM was 0.34 mg/cm^2. (b) The formation of $MV^{+\bullet}$ under visible light irradiation (λ>390nm) and its decay upon stopping the illumination. (c) Dependence of steady state concentration of $MV^{+\bullet}$ on the loading of Pd in the BPM-CdS/Pd membrane.

The formation of the reduction product $MV^{+\bullet}$ in the AEL compartment was monitored by recording the absorption spectra (Figure 4.8(a)). With continued irradiation of visible light, the absorption peaks increased, these are related to the formation of $MV^{+\bullet}$ radicals at 395 nm and 610 nm respectively. From the $MV^{+\bullet}$ extinction coefficient (13700 $M^{-1}cm^{-1}$)[18], it is possible to calculate the concentration of $MV^{+\bullet}$ formed in the AEL compartment. With increasing photo irradiation time, the $MV^{+\bullet}$ attained a steady state concentration of 135 μM

(Figure 4.8 (b)). Metal nanoparticles are also capable of accepting electrons to catalyze other reduction processes (reaction 4.11).

$$BPM\text{-}CdS/Pd + MV^{+\bullet} \longrightarrow BPM\text{-}CdS/Pd(e) + MV^{2+} \quad (4.11)$$

For example, the electron transfer between photogenerated $MV^{+\bullet}$ and metal nanoparticles have been investigated for H_2 generation in aqueous solutions.[19,20] The interesting aspect of attaining the steady state concentration of $MV^{+\bullet}$ during steady state irradiation is the result of forward (reaction 4.10) and back (reaction 4.11) electron transfer. The plot in Figure 4 (b) shows the growth of $MV^{+\bullet}$ during visible light irradiation attaining a steady state in ~60 minutes. Considering the pseudo-first order of the kinetic, it is possible to calculate the rate constant of the process which is 5×10^{-3} min^{-1}. When the illumination is stopped, the back electron transfer results in a decrease in $MV^{+\bullet}$ concentration (Figure 4.8 (b)). The rate constant for back electron transfer is 2×10^{-3} min^{-1}. The difference between forward and back electron transfer dictates the steady state concentration.

The estimate of steady state concentration of $MV^{+\bullet}$ it is possible to estimate the flat band potential of BPM-CdS/Pd membrane using the Nernst expression (expression 4.12).

$$E_{FB} = E^{0}_{(MV^{2+}/MV^{+\bullet})} - 0.059\log[MV^{+\bullet}]/[MV^{2+}] \quad (4.12)$$

By substituting the steady state concentrations of $MV^{+\bullet}$ and MV^{2+} along with the redox potential of the $MV^{2+}/MV^{+\bullet}$ couple, $E^{\circ} = -0.449$ V vs. NHE,[21,22] we obtain E_{FB} as -0.460 V vs. NHE. This estimation of E_{FB} provides the energetics of the membrane with which it can induce redox processes.

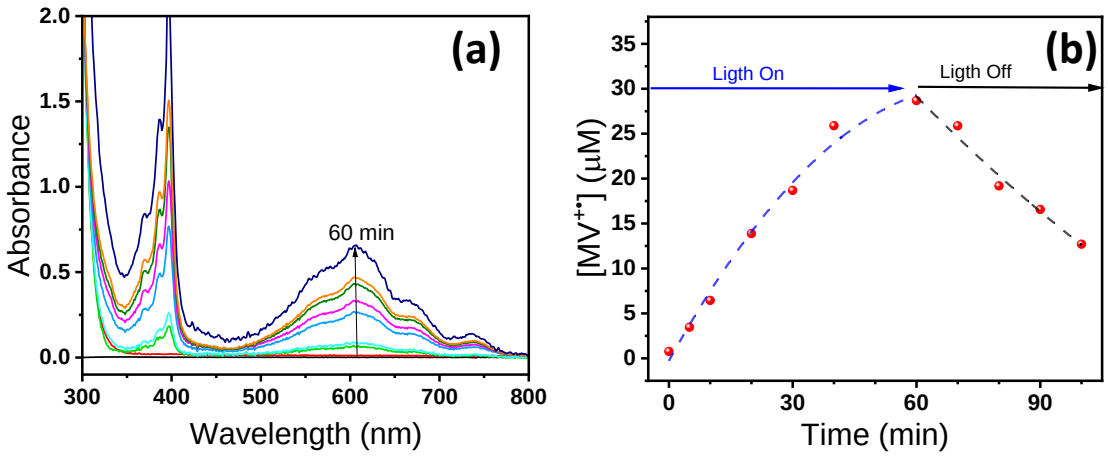

Figure 4.9. (a) MV^{2+} reduction under irradiation for 60 min. (b) Formation of $MV^{+\bullet}$ radical during radiation (light on) and back-electron transfer (with light off).

This experiments are repeated with four other BPM-CdS/Pd membranes having different loading of Pd (0.17–0.30 mg/cm^2). In particular, increasing the concentration of PdNPs in the membrane to 0.30 mg/cm^2 the reduction of MV^{2+} occurred as reported in the Figure 4.9 (a-b) upon 60 min under irradiation with a rate of $1.03x10^{-6}$ min^{-1}. The back electron transfer process (after stopping the illumination) occurred with $5.5x10^{-5}$ min^{-1} rate constant. The steady state concentration achieved with all membranes, where the loading of Pd (II) is different according with the Table 4, are presented in Figure 4.8 (c). It is evident that the increased Pd loading leads to increased $MV^{+\bullet}$ concentration indicating that the high loading of Pd is required to capture the photogenerated electrons from CdS and transfer to MV^{2+} in AEL compartment. These experiments confirm the vectorial electron transfer from CEL compartment to AEL compartment induced through the excitation of BPM-CdS/Pd membrane.

4.7 Photodegradation of Nitro-phenolic compounds

Semiconductor assisted photocatalysis has been widely studied in the remediation of organic pollutants from air and water.[23] Of particular interest are nitroaromatic compounds such as nitrophenol and trinitrophenol, which are environmental water contaminants.[24–26] In order to test the feasibility of the BPM-CdS/Pd membrane for degradation of nitroaromatics, 4-nitrophenol (NP) is used as a representative pollutant in the AEL compartment. An aqueous solution of NP (25 μM) with pH adjusted to 10 so that it exists in solution as nitrophenoxide ion (pKa ~7), with absorption maximum at 400 nm is introduced in AEL compartment of H-Cell, while in the CEL side of the H-Cell was introduced ethanol as hole scavengers and was subjected to visible light excitation (λ>390 nm), see Scheme 4.1

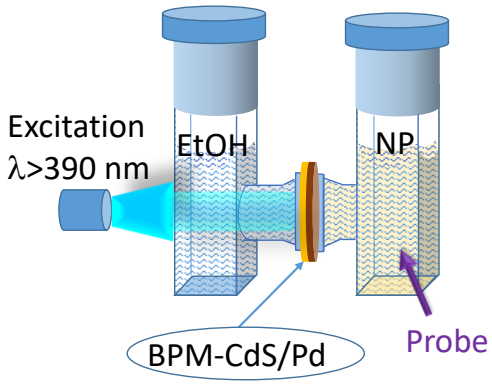

Scheme 4.1. Experimental setup for the oxidation of 4-nitro phenol by the presence of BPM-CdS/Pd inserted in the middle of H-Cell and ethanol as hole scavengers in CEL side of the H-Cell.

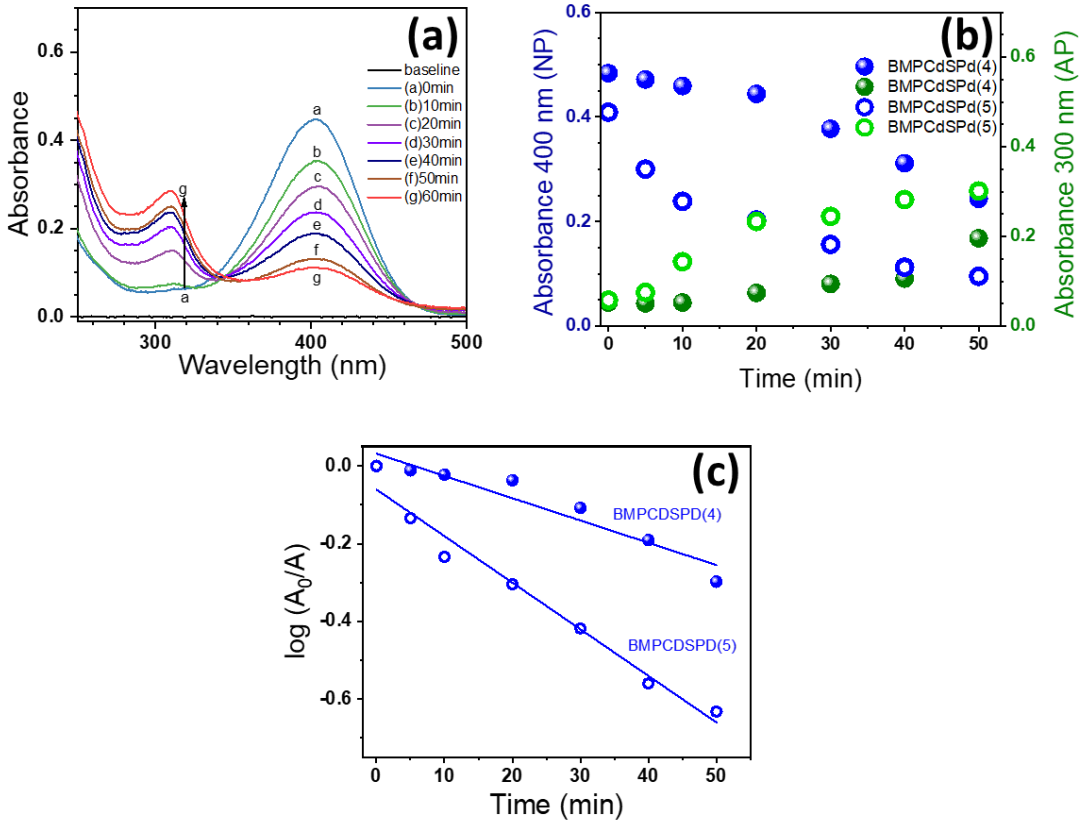

Figure 4.10. Photocatalytic reduction of 25 μM 4-nitrophenol in water (AEL compartment) during the visible light irradiation of BPM-CdS/Pd. (A) Absorption spectra of AEL compartment solution recorded at different irradiation times ([Pd] in the membrane = 0.34 mg/cm^2). (B) Decrease of 4-NP absorbance at 400 nm and growth of 4-AP absorbance at 300 nm at two different Pd Loadings (0.30 (solid circles) and 0.34 (open circles) mg/cm^2 Pd). (C) Pseudo first order kinetic analysis for the decay of 4-NP at two different Pd loadings. The CEL compartment contained 3:1 ethanol/water by volume for these experiments.

The absorption spectrum of the solution in AEL compartment was recorded periodically during photo irradiation of the CdS side of the BPM-CdS/Pd membrane. The vectorial flow of electrons from CdS to Pd resulted in the reduction of NP to 4-amino phenol (AP). The decrease in NP absorption at 400 nm coincided with increase in the absorption of AP at 310 nm, as can be noted from the Figure 4.10 (a).[26,27] The decrease in the absorption at 400 nm and growth of absorption at 300 nm with irradiation time are shown in Figure 4.10 (b)

for two different Pd concentrations. The kinetic analysis of NP decay shows pseudo-first order degradation rate of 6×10^{-3} s^{-1} and 1×10^{-2} s^{-1} for Pd catalyst loadings of 0.30 and 0.34 mg/cm^2, respectively, in the BPM-CdS/Pd membrane. This increase in rate constant with increased metal nanoparticle loading follows the trend seen with MV^{2+} reduction seen in Figure 4.8 c). The results further establish the effectiveness of BPM-CdS/Pd membrane in the photocatalytic reduction of 4-NP.

4.7.1 Simultaneously photodegradation of chloro-phenol and nitro-phenol compounds

Organochlorines have been widely used as pesticides and wood treatment chemicals. Their contamination of soil, water and food products are an emerging problems related to the water contaminations.[24,28,29] Advanced oxidation process such as photocatalysis are quite effective in the remediation of such organochlorines. 4-chlorophenol (CP) is employed as a model pollutant to understand the possibility of its oxidation and meantime the reduction of 4-nitrophenol. By replacing ethanol with CP as the electron donor in the CEL compartment, the stability of CdS is maintained over the time.

The H-cell containing aqueous solutions of 30 μM CP in the CEL compartment and 30 μM NP in AEL compartment separated by the BPM-CdS/Pd membrane was irradiated with the visible light (λ>390 nm).

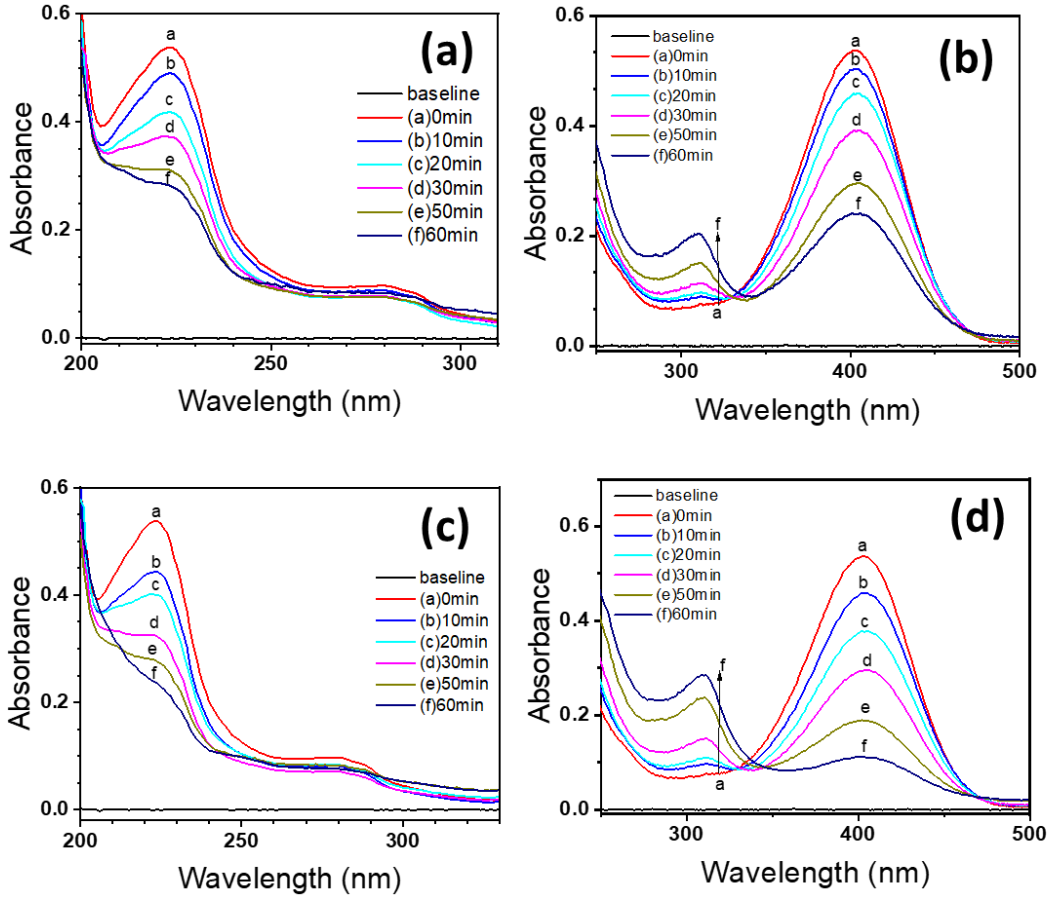

Figure 4.11. Absorption changes of (a), (c) 4-chlorophenol (30 μM aqueous solution in CEL compartment) and (b),(d) 4-nitrophenol (30 μM aqueous solution in AEL compartment) recorded during the visible (>390 nm) irradiation of BPM-CdS/Pd at two different Pd loadings: (a), (b) 0.30 mg/cm^2, and (c),(d) 0.34 mg/cm^2 Pd.

During the photocatalytic experiment, electrons and holes are generated in the surface of the membrane, and it is possible to observe a decrease in absorbance of the parent compound in the two compartments. Figure 4.11 shows the changes in the absorption of NP and CP at different irradiation times. These changes in the absorption can be related to the oxidation of CP by the holes generated at CdS and reduction of NP at the Pd interface,

see the reaction 4.12-4.13, related to the oxidation and reduction process in the CEL and AEL comportment during the photocatalytic experiment.

CEL

$$\text{BPM-CdS(h)/Pd + CP} \longrightarrow \text{BPM-CdS/Pd + (chlorocatechol, hydroquinone…)} \longrightarrow \longrightarrow CO_2 + HCl \quad (4.12)$$

AEL

$$\text{BPM-CdS/Pd(e) +NP} \longrightarrow \text{BPM-CdS/Pd + AP} \quad (4.13)$$

Figures 4.11 (a) and 4.11 (c) show the changes in the absorption spectra of CP over the time with different loading of Pd species in the BPM-CdS/Pd membranes. The decrease in absorbance at 300 nm is indicative of degradation of CP as it reacts with the holes generated at CdS. As shown earlier the photocatalytic oxidation of CP results in the formation of chlorocatechol and hydroquinone as major intermediates with ultimate conversion to CO_2 and HCl (reaction 4.12).[30,31] The absorption changes of the solution in the AEL compartment (Figures 4.12 (b) and 4.12 (d)) confirmed the transformation of NP to AP (reaction 4.13).

Considering the decrease of the absorbance, the degradation efficiency and the rate constant are calculated for the BMP-CdS/Pd with 0.30 mg/cm^2 and 0.34 mg/cm^2 of Pd in the AEL side. As can show in the Figures 4.12 (a) and 4.12 (b) at lower Pd concentration the percent degradation of NP and CP are similar, is achieved about 50% degradation during 60 minutes of light irradiation.

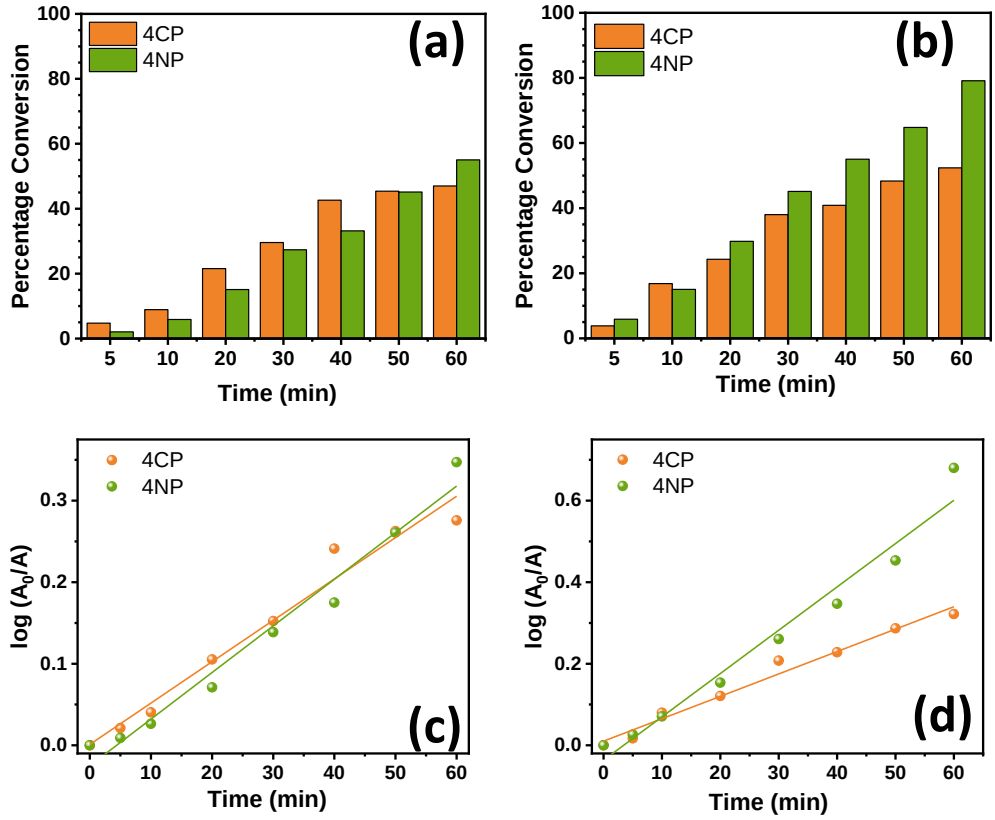

Figure 4.12. Percentage conversion of 4-chlorophenol (CP; 30 μM in CEL compartment) and 4-notrophenol (NP; 30 μM in AEL compartment) monitored during the visible (λ>390 nm) irradiation of BPM-CdS/Pd at two different Pd loadings. (a) 0.30 mg/cm^2, and (b) 0.34 mg/cm^2 Pd. (c) and (d) show corresponding first order plots.

On the other hand, with higher Pd loading a higher degree of NP degradation while the CP degradation remains almost the same. The kinetic rate followed this trend; the conversion of NP to AP is faster in the BPM-CdS/Pd where the concentration of Pd is 0.34 mg/cm^2. It is interesting to note that at lower Pd concentration the rate constants of the two degradations are closely matched (see Table 4.1).

Table 4.1. Kinetic rate for the photodegradation of CP and NP.

Pd loadings	**CP**	**NP**
(mg/cm^2)	**k (min^{-1})**	**k (min^{-1})**

0.30	0.005 (R^2=0.96)	0.005 (R^2=0.97)
0.34	0.006 (R^2=0.96)	0.01 (R^2=0.97)

The similarity of the two rate constants explains achieving constant conversion between the two model contaminants (CP and NP) at lower Pd loading in the membrane. The higher rate constant of degradation at 0.34 mg/cm^2 Pd loadings explains the higher percent of degradation of NP. These results show that one can modulate the degradation rates of organic contaminants in AEL and CEL compartments by controlling the loading of photocatalyst and metal nanoparticles in the BPM. In order to maintain the stability of the photocatalyst and electrocatalyst in the BPM membrane and maximize the photo conversion efficiency one needs to balance the rates of both reduction and oxidation processes.

4.8 Conclusion

In conclusion, the principal results of this study are:

- The possibility to use the bipolar membrane as host matrix for selective incorporation of different nanostructures in the two side of the polymer.
- The electron transfer process from the cationic exchange layer to the anionic exchange layer has been demonstrated.
- The use of MV^{2+} permitted to have an insight to the catalytic properties of the materials by the presence of Pd species in the AEL side of BPM.

- The oxidation and reduction of organic compounds engaged with the photo driven electrons across the junction of the BPM.
- e simultaneous oxidation of 4-chlorophenol and the reduction of 4-nitrophenol under visible light irradiation of the BPM-CdS/Pd shows its effectiveness in photocatalytic remediation of chemical contaminants.
- The possibility to extend the design of the photocatalytic membrane in a flow cell design.

4.9 References

(1) Costantino, F.; Gavioli, L.; Kamat, P. V. A Bipolar CdS/Pd Photocatalytic Membrane for Selective Segregation of Reduction and Oxidation Processes. *ACS Phys. Chem Au* **2021**. https://doi.org/10.1021/acsphyschemau.1c00035.

(2) Herrmann, J.-M.; Guillard, C.; Pichat, P. Heterogeneous Photocatalysis : An Emerging Technology for Water Treatment. *Catalysis Today* **1993**, *17* (1–2), 7–20. https://doi.org/10.1016/0920-5861(93)80003-J.

(3) *Water Pollution and Remediation: Photocatalysis*; Inamuddin, Ahamed, M. I., Lichtfouse, E., Eds.; Environmental Chemistry for a Sustainable World; Springer International Publishing: Cham, 2021; Vol. 57. https://doi.org/10.1007/978-3-030-54723-3.

(4) Hou, W.; Cronin, S. B. A Review of Surface Plasmon Resonance-Enhanced Photocatalysis. *Adv. Funct. Mater.* **2013**, *23* (13), 1612–1619. https://doi.org/10.1002/adfm.201202148.

(5) *Photocatalysis: Fundamentals and Perspectives*; Schneider, J., Bahnemann, D., Ye, J., Li Puma, G., Dionysiou, D. D., Eds.; Energy and Environment Series; The Royal Society of Chemistry, 2016. https://doi.org/10.1039/9781782622338.

(6) Nosaka, Y.; Nosaka, A. Y. Generation and Detection of Reactive Oxygen Species in Photocatalysis. *Chem. Rev.* **2017**, *117* (17), 11302–11336. https://doi.org/10.1021/acs.chemrev.7b00161.

(7) Giesbrecht, P. K.; Freund, M. S. Recent Advances in Bipolar Membrane Design and Applications. *Chem. Mater.* **2020**, *32* (19), 8060–8090. https://doi.org/10.1021/acs.chemmater.0c02829.

(8) Blommaert, M. A.; Aili, D.; Tufa, R. A.; Li, Q.; Smith, W. A.; Vermaas, D. A. Insights and Challenges for Applying Bipolar Membranes in Advanced Electrochemical Energy Systems. *ACS Energy Lett.* **2021**, *6* (7), 2539–2548. https://doi.org/10.1021/acsenergylett.1c00618.

(9) Pärnamäe, R.; Mareev, S.; Nikonenko, V.; Melnikov, S.; Sheldeshov, N.; Zabolotskii, V.; Hamelers, H. V. M.; Tedesco, M. Bipolar Membranes: A Review on Principles, Latest Developments, and Applications. *Journal of Membrane Science* **2021**, *617*, 118538. https://doi.org/10.1016/j.memsci.2020.118538.

(10) Chhetri, M.; Kamat, P. V. Vectorial Charge Transfer Across Bipolar Membrane Loaded with CdS and Au Nanoparticles. 16.

(11) Jaroszek, H.; Dydo, P. Ion-Exchange Membranes in Chemical Synthesis – a Review. *Open Chemistry* **2016**, *14* (1), 1–19. https://doi.org/10.1515/chem-2016-0002.

(12) Mau, A. W. H.; Huang, C. B.; Kakuta, N.; Bard, A. J.; Campion, A.; Fox, M. A.; White, J. M.; Webber, S. E. Hydrogen Photoproduction by Nafion/Cadmium Sulfide/Platinum Films in Water/Sulfide Ion Solutions. *J. Am. Chem. Soc.* **1984**, *106* (22), 6537–6542. https://doi.org/10.1021/ja00334a014.

(13) Kakuta, N.; White, J. M.; Campion, A.; Bard, A. J.; Fox, M. A.; Webber, S. E. Surface Analysis of Semiconductor-Incorporated Polymer Systems. 1. Nafion and

Cadmium Sulfide-Nafion. *J. Phys. Chem.* **1985**, *89* (1), 48–52. https://doi.org/10.1021/j100247a014.
(14) Park, H.; Park, Y.; Bae, E.; Choi, W. Photoactive Component-Loaded Nafion Film as a Platform of Hydrogen Generation: Alternative Utilization of a Classical Sensitizing System. *Journal of Photochemistry and Photobiology A: Chemistry* **2009**, *203* (2–3), 112–118. https://doi.org/10.1016/j.jphotochem.2008.12.025.
(15) Zeizinger, M.; Burda, J. V.; Šponer, J.; Kapsa, V.; Leszczynski, J. A Systematic Ab Initio Study of the Hydration of Selected Palladium Square-Planar Complexes. A Comparison with Platinum Analogues. *J. Phys. Chem. A* **2001**, *105* (34), 8086–8092. https://doi.org/10.1021/jp010636s.
(16) Gopidas, K. R.; Bohorquez, Maria.; Kamat, P. V. Photophysical and Photochemical Aspects of Coupled Semiconductors: Charge-Transfer Processes in Colloidal Cadmium Sulfide-Titania and Cadmium Sulfide-Silver(I) Iodide Systems. *J. Phys. Chem.* **1990**, *94* (16), 6435–6440. https://doi.org/10.1021/j100379a051.
(17) Harris, C.; Kamat, P. V. Photocatalytic Events of CdSe Quantum Dots in Confined Media. Electrodic Behavior of Coupled Platinum Nanoparticles. *ACS Nano* **2010**, *4* (12), 7321–7330. https://doi.org/10.1021/nn102564x.
(18) Watanabe, T.; Honda, K. Measurement of the Extinction Coefficient of the Methyl Viologen Cation Radical and the Efficiency of Its Formation by Semiconductor Photocatalysis. *J. Phys. Chem.* **1982**, *86* (14), 2617–2619. https://doi.org/10.1021/j100211a014.
(19) Sant, P. A.; Kamat, P. V. Interparticle Electron Transfer between Size-Quantized CdS and TiO2 Semiconductor NanoclustersDedicated to Professor Frank Wilkinson on the Occasion of His Retirement. *Phys. Chem. Chem. Phys.* **2002**, *4* (2), 198–203. https://doi.org/10.1039/b107544f.
(20) Nakahira, T.; Graetzel, M. Fast Electron Storage with Colloidal Semiconductors Functionalized with Polymeric Viologen. *J. Phys. Chem.* **1984**, *88* (18), 4006–4010. https://doi.org/10.1021/j150662a029.
(21) Meisel, D.; Mulac, W. A.; Matheson, M. S. Catalysis of Methyl Viologen Radical Reactions by Polymer-Stabilized Gold Sols. *J. Phys. Chem.* **1981**, *85* (2), 179–187. https://doi.org/10.1021/j150602a015.
(22) Bird, C. L.; Kuhn, A. T. Electrochemistry of the Viologens. *Chem. Soc. Rev.* **1981**, *10* (1), 49. https://doi.org/10.1039/cs9811000049.
(23) Ollis, D. F.; Pelizzetti, E.; Serpone, N. Photocatalyzed Destruction of Water Contaminants. *Environ. Sci. Technol.* **1991**, *25* (9), 1522–1529. https://doi.org/10.1021/es00021a001.
(24) Carvalho, F. P. Pesticides, Environment, and Food Safety. *Food and Energy Security* **2017**, *6* (2), 48–60. https://doi.org/10.1002/fes3.108.
(25) Peller, J.; Wiest, O.; Kamat, P. V. Hydroxyl Radical's Role in the Remediation of a Common Herbicide, 2,4-Dichlorophenoxyacetic Acid (2,4-D). *J. Phys. Chem. A* **2004**, *108* (50), 10925–10933. https://doi.org/10.1021/jp046450l.

(26) Schmelling, D. C.; Gray, K. A.; Kamat, P. V. Role of Reduction in the Photocatalytic Degradation of TNT. *Environ. Sci. Technol.* **1996**, *30* (8), 2547–2555. https://doi.org/10.1021/es950896l.
(27) Strachan, J.; Barnett, C.; Masters, A. F.; Maschmeyer, T. 4-Nitrophenol Reduction: Probing the Putative Mechanism of the Model Reaction. *ACS Catal.* **2020**, *10* (10), 5516–5521. https://doi.org/10.1021/acscatal.0c00725.
(28) Wolff, M. S.; Toniolo, P. G. Environmental Organochiorine Exposure as a Potential Etiologic Factor in Breast Cancer. *Environmental Health Perspectives* **1995**, *103*, 5.
(29) Muir, D. C. G.; Norstrom, R. J.; Simon, Mary. Organochlorine Contaminants in Arctic Marine Food Chains: Accumulation of Specific Polychlorinated Biphenyls and Chlordane-Related Compounds. *Environ. Sci. Technol.* **1988**, *22* (9), 1071–1079. https://doi.org/10.1021/es00174a012.
(30) Stafford, U.; Gray, K. A.; Kamat, P. V. Radiolytic and TiO2-Assisted Photocatalytic Degradation of 4-Chlorophenol. A Comparative Study. *J. Phys. Chem.* **1994**, *98* (25), 6343–6351. https://doi.org/10.1021/j100076a019.
(31) D'Oliveira, J. C.; Al-Sayyed, G.; Pichat, P. Photodegradation of 2- and 3-Chlorophenol in Titanium Dioxide Aqueous Suspensions. *Environ. Sci. Technol.* **1990**, *24* (7), 990–996. https://doi.org/10.1021/es00077a007.

CHAPTER 5: CONCLUSIONS AND FUTURE WORK

This research project is focused on the development of new nanocomposite materials able to degrade organic pollutants in water. The incorporation of nanomaterials in a solid porous matrix ensures the preparation of functional composites, which do not require the use of expensive and post-treatment steps after the water remediation process.

Our general approach is very simple and consists on the preparation of polymer nanocomposites based on the electrospinning technique and the in-situ synthesis of NPs, by the presence of a salt precursor, on the mats under mild conditions. This simple and low-cost method is easily scalable. We chose CA as a matrix considering its properties such as renewability, biocompatibility, and biodegradability in the environment. At first, we realized a fibrous membrane made of CA/SnO_2; the preparation of this nanocomposite allow us to understand two aspects: the good photochemical properties of SnO_2 NPs, which are rarely studied for water treatment applications and the advantage of the in-situ synthesis of the NPs in the porous substrate. The SnO_2 fixed stably in the ultrafine polymer fibers showed a good photocatalytic performance under UV irradiation; in particular, the nanoparticles act as oxidation site against a cationic and anionic dye such as MB and MO. Using these fibrous mats, we reach a good degree of the degradation and mineralization of both dyes detecting different by-product in water.

Considering that the UV light is only 5% of the solar spectrum, we combined cerium nanoparticles and Pt nanoclusters in the CA membrane in order to have a photocatalytic degradation of MB under visible light irradiation. The nucleation and growth of ceria NPs

in close contact with the deposited PtNCs directly in the solid mats improve the photocatalytic performances of the nanocomposites, thanks to the enhancement of oxygen vacancies and the possible formation of the Schottky junction in the heterostructures. In order to better understand this combination, the detection of the reactive oxygen species produced during the photodegradation allow us to verify the presence of hydroxyl radicals and holes as main species during the degradation of the cationic MB dye

In the last part of this research, we used a different approach. Starting from a commercial Bipolar Membrane (BPM, Fumasep ®) we are able to synthesize directly on the membrane two different types of nanostructure materials. Using the exchange capability of the BPM's layers, we synthesize the CdS and Pd nanostructures on the cationic and anionic side of the membrane.

The advantage is in the separation of oxidation and reduction processes while continuing to engage in photo-driven reactions. The example of simultaneous oxidation of 4-chlorophenol and the reduction of 4-nitrophenol under visible light irradiation of the BPM-CdS/Pd shows its effectiveness in photocatalytic remediation of chemical contaminants

The nanocomposites prepared and studied in this work overcome many problems of the traditional method for water purification. The presence of a solid support facilitates the handling and transportation of the photocatalysts, and eliminates additional processing steps after the remediation process for the removal of the photocatalysts, as in the case of powder used for water treatment. The presence of the NPs embedded in the solid matrix can prevented their release in the environment. This promising approach to prepare these

nanocomposites can be used to develop a new class of materials, which can be use directly during the wastewater treatment.

APPENDIX A: INSTRUMENT DETAILS

Scanning Electron Microscopy (FE-SEM and HR-SEM)

Morphological analysis of all materials was performed by field emission scanning electron spectroscopy (FE-SEM-EDS) (JEOL, JSM 6490) operating with an acceleration voltage of 10 kV. The specimens were previously coated with 10 nm thick Au layer. High resolution HR-SEM images were acquired with a high-resolution scanning electron microscope (HR-SEM) equipped with a cold field emission gun (JEOL JSM 7500F, accelerating voltage of 10 kV, chamber pressure of 9.6x10-5 Pa).

Transmission Electron Microscopy (TEM)

Morphology and size distribution of the formed NPs were investigated by a JEOL JEM-1011 transmission electron microscope (TEM) equipped with a tungsten thermionic electron source, operating at 100 kV. The TEM samples were prepared by dissolving about 0.0050g of the nanocomposite mat in 1 mL of acetone/DMF, sonicated for 30 min and then filtered (PTFE filter 0.45 μm pore size). Subsequently 5 μL of the prepared solution was placed on a TEM copper grid and dried at room temperature.

X-Ray Diffraction analysis (XRD)

X-Ray Diffraction (XRD) measurements were performed on a PANanalytical Empyrean X-ray diffractometer equipped with a 1.8kW CuKα ceramic X-ray tube (λ=1.5418 Å) operating at 45 kV and 40 mA, and a PIXcel^{3D} area detector (2x2 mm^2). The characterization was performed in air and at room temperature in parallel beam geometry

and symmetric reflection mode. The data analysis was carried out using PANanalytical Highscore 4.1 software.

UV-Visible analysis

UV-Vis diffuse reflectance spectroscopy analysis was performed using a Varian Cary 6000i (Agilent) UV-visible-NIR spectrophotometer in the range of 200-800 nm, equipped with an integrating sphere and calibrated with an MgO mirror before starting the measurements.

The UV-Vis analysis of the organic pollutants were performed by Varian Cary 6000i (Agilent) UV-visible-NIR spectrophotometer in the range of 200-800 nm, using a water solution as blank solvent.

Fourier Transform Infrared analysis

Fourier Transform Infrared analysis (FTIR) of the fibrous mats in an attenuated total reflectance (ATR)-mode was performed with an FTIR spectrometer (Equinox 70 FT-IR, Bruker), coupled to an ATR accessory (MIRacle ATR, PIKE Technologies). Each spectrum was acquired by accumulating 128 scans in the 4000-600 cm^{-1} spectral range with a scanning resolution of 4 cm^{-1}.

Emission Spectra

Emission spectra were measured at a room temperature on the solid samples with Fluoromax®-4 spectrofluorometer (Horiba Jobin-Yvon Inc., France) with an excitation wavelength $\lambda_{ex} = 520nm$ for all samples, (analysis related to the sample CeO2/Pt in the Chapter 3).

Raman analysis

The Raman spectra of the fiber mats were acquired by a Raman LabRam HR800 (Horiba Jobin-Yvon Inc., France) spectrometer equipped with a built-in microscope with objectives 10x (NA 0.25) and 50x (NA 0.75), using the 632.8 nm He-Ne laser excitation. The experimental setup consists of a grating (600 lines mm^{-1}) with a spectral resolution of approximately 1 cm^{-1}.

X-ray photoelectron spectroscopy analysis

X-ray photoelectron spectroscopy (XPS) was performed using an electron spectrometer (Lab2, Specs, Berlin, Germany) equipped with a monochromatic X-ray source (set at 1253 eV) and with a hemispherical energy analyzer (Phoibos, HSA3500, also from Specs). The applied voltage of the Mg Kα X-ray source was set at 12 kV and the applied current at 7 mA. The pressure in the analysis chamber was ≈1 × 10−9 mbar. The large area lens mode was used for both wide and narrow scans. For the wide scan, the energy pass was 90 eV and the energy step was 1 eV. For the narrow high-resolution scan, the energy pass was 30 eV and the energy step was 0.1 eV. A flood gun was used to neutralize the surface charge, having an energy of 7 eV and a filament current of 2.2 A.

APPENDIX B: CALCULATION AND APPROXIMATION

Scherrer's Equation

The crystalline domain of the NPs is calculated by applying the Scherrer's equation (equation b.1) using the characteristic peak related to the crystalline structure of each NPs in the XRD pattern

$$d = \frac{K\lambda}{W cos\theta} \quad \text{(eq. B1)}$$

where the shape factor K is equal to 1, λ corresponds to the wavelength of Cu Kα and W is the full width of half maximum (FWHM) of the peak.

Kubelka-Munk approximation

The diffuse-reflectance spectra of the white standard (MgO) and of the samples were collected (Figure S7a), and the R(Reflectance, %) (Eq. S3) and the Kubelka−Munk function *(F)* (Eq. S4) were calculated.

$$R = {Rsample}/{Rstandard} \quad \text{(eq. B2)}$$

$$F(R) = (1 - R)^{\frac{2}{2R}} = \alpha/S \quad \text{(eq. B3)}$$

F(R) is proportional to the absorption coefficient (α), if it is assumed that the scattering coefficient (S) is approximately constant.

The absorption coefficient of semiconductors in the region near the absorption edge is given by Eq. S5, where *hv* is the energy of the incident light and η depends on the type of the optical transition. The η value can be 1/2, 3/2, 2, or 3 for direct-allowed, direct-forbidden, indirect-allowed, and indirect forbidden transitions, respectively.

$$\alpha \propto (hv - E_g)^{\eta}/(hv) \qquad \text{(eq. B4)}$$

Therefore, the absorption edge (band gap energy *Eg*) can be determined by plotting $(F(R)hv)^{1/\eta}$ as a function of *hv*. After a linear regression of the obtained plot, the *x*-intercept reveals the energy of the band gap. We considered a direct-allowed transition, and therefore the $(F(R)hv)^2$ versus *hv* was plotted.

Chapter 2

Photodegradation of Methyl Orange and Methylene Blue

Calibration Curve

Initially the absorption spectra of the dyes solutions with different concentrations (from 0.1 to 5 ppm) were recorded. The intensity of the representative absorption peak for each dye concentration was then plotted, and the equation which gives the dependence of the intensity to the dye concentration was defined by a linear fit. For MO the absorption intensity dependence to the concentration (Figure S1) is defined by equation S1, and for MB by equation S2.

$y= 0.068+0.069x$ Eq. C1

$y= 0.014+0.140x$ Eq. C2

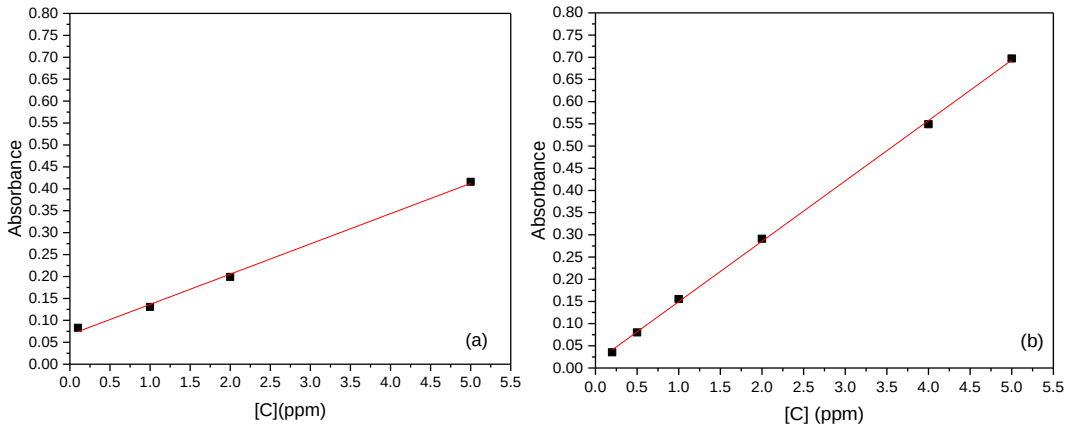

Figure C1. Calibration curve of (a) MO (R2= 0.99) and of (b) MB (R2 = 0.99).

Chapter 3

Calibration curve

Initially the absorption spectra of aqueous solutions containing different concentrations of MB (from 0.1 to 5 ppm) and the emission spectra of aqueous solutions containing different concentrations of fluorescein (from 8 um to 0.5 μm) were recorded (Figure S2a,c). The intensity of the representative absorption peak of MB (λ_{abs}=664nm) and of the emission peak of fluorescein (λ_{em}=515nm) for each concentration were then plotted (Figure S1b,d) and the linear fitting in each case was conducted. Therefore, for MB the absorption intensity dependence to the concentration is defined by equation S1 and for Fluorescein by equation S2.

$y = 0.14+0.014x$ Eq. S1

$y = 3.25 \cdot 10^{-6}x$ Eq. S2

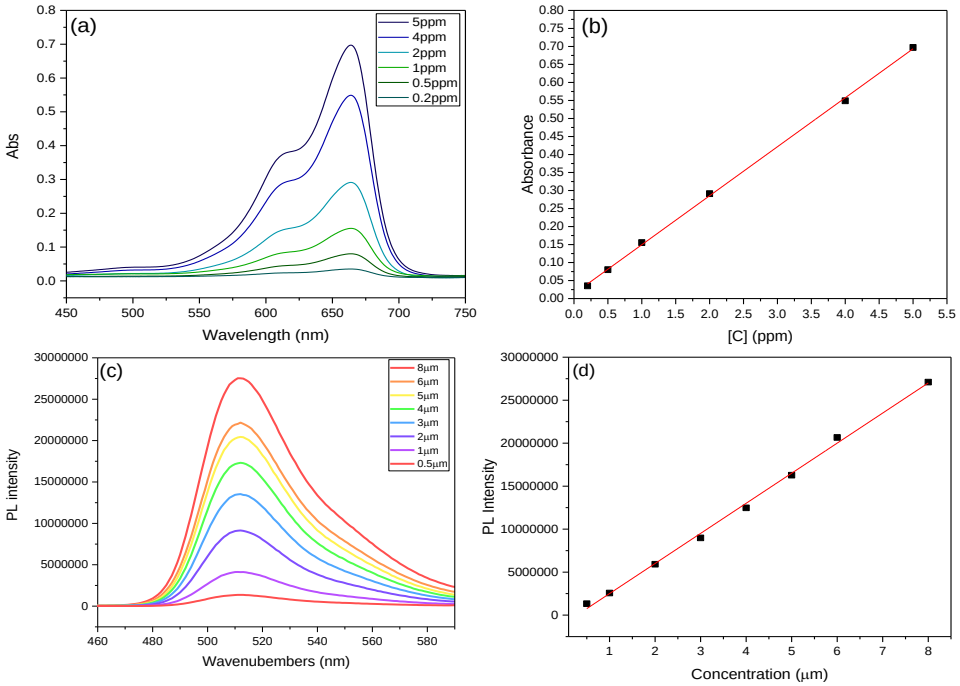

Figure C2. (a) Absorption spectra and (b) calibration curve of MB. (c) Emission spectra and related calibration curve of FL.